Tomographic measurement of all orthogonal components of three-dimensional displacement fields within scattering materials using Wavelength Scanning Interferometry

By

Semanti Chakraborty

A Doctoral Thesis
Submitted in partial fulfilment of the requirements for the award
of Doctor of Philosophy of Loughborough University

December 2012

Abstract

Experimental mechanics is currently contemplating tremendous opportunities of further advancements thanks to a combination of powerful computational techniques and also full-field non-contact methods to measure displacement and strain fields in a wide variety of materials. Identification techniques, aimed to evaluate material mechanical properties given known loads and measured displacement or strain fields, are bound to benefit from increased data availability (both in density and dimensionality) and efficient inversion methods such as finite element updating (FEU) and the virtual fields method (VFM). They work at their best when provided with dense and multicomponent experimental displacement (or strain) data, i.e. when all orthogonal components of displacements (or all components of the strain tensor) are known at points closely spaced within the volume of the material under study. Although a very challenging requirement, an increasing number of techniques are emerging to provide such data.

In this Thesis, a novel wavelength scanning interferometry (WSI) system that provides three dimensional (3-D) displacement fields inside the volume of semi-transparent scattering materials is proposed. Sequences of two-dimensional interferograms are recorded whilst tuning the frequency of a laser at a constant rate. A new approach based on frequency multiplexing is used to encode the interference signal corresponding to multiple illumination directions at different spectral bands. Different optical paths along each illumination direction ensure that the signals corresponding to each sensitivity vector do not overlap in the frequency domain. All the information required to reconstruct the location and the 3-D displacement vector of scattering points within the material is thus recorded simultaneously in a single wavelength scan. By comparing phase data volumes obtained for two successive scans, all orthogonal components of the three dimensional displacement field introduced between scans (e.g. by means of loading or moving the sample under study) are readily obtained with high displacement sensitivity.

The fundamental principle that describes the technique is presented in detail, including the correspondence between interference signal frequency and its associated depth within the sample, depth range, depth resolution, transverse resolution and displacement sensitivity. Data processing of the interference signal includes Fourier transformation, noise reduction, re-registration of data volumes, measurement of the illumination and sensitivity vectors from

experimental data using a datum surface, phase difference evaluation, 3-D phase unwrapping and 3-D displacement field evaluation.

Experiments consisting of controlled rigid body rotations and translations of a phantom were performed to validate the results. Both in-plane and the out-of-plane displacement components were measured for each voxel in the resulting data volume, showing an excellent agreement with the expected 3-D displacement.

Acknowledgements

List of Nomenclature

$A_0(m, n, t)$	Complex amplitude of reference wavefront
$A_{pj}(m, n, t)$	Complex amplitude of the scattered wavefront from the p-th illumination beam at the j-th slice within the object
atan2	Four quadrant inverse tangent
c	Speed of light in vacuum
$\mathbf{e}_p$	Unit vector pointing along p-th illumination beam
$\mathbf{e}_{p'}$	Unit vector pointing along the p-th refracted beam
$\mathbf{e}_o$	Unit vector pointing along the observation direction
$f_{\Lambda pj}$	Frequency (cycles per frame for the p-th beam scattered at j-th layer of the sample)
$\hat{f}_{\Lambda pj}$	Frequency in units of cycles per scan duration
$\hat{\mathbf{i}}, \hat{\mathbf{j}}$ and $\hat{\mathbf{k}}$	Unit vectors along x, y and z axes respectively
$I(t)$	Intensity of interference signal
$\tilde{I}(\hat{f})$	Fourier transform of intensity $I(t)$
j,l	Slice indexes
k	Wavenumber
k_c	Central wavenumber
δk	Interframe wavenumber increment
Δk	Wavenumber range
L_1, L_2, L_3	Near-infrared double achromats for illumination
L_4, L_5	Near-infrared double achromats for reference delay line
L_6, L_7	Near-infrared double achromats for imaging the sample
M	Magnification
(m, n)	Integer pixel coordinates on the photodetector array
n_0	Refractive index of surrounding media
n_1	Refractive index within the material
$\mathbf{n}_p$	Normal vector to the p-th reconstructed surface
$\mathbf{N}$	Unit vector normal to the surface of the material
N_m	Number of pixel rows in the region of interest

N_n	Number of pixel columns in the region of interest
N_s	Number of discrete thin scattering layers inside the Sample, parallel to its surface
N_t	Number of frames
p_x	Pixel pitch along the columns (n axis)
p_y	Pixel pitch along rows (m axis)
p, q	Illumination beam indexes
Q	The size of the local region in DVC, determines the displacement and strain spatial resolution for independent measurements.
$\mathbf{r}$	Position vector of point (x, y, z) inside the material
$\mathbf{r}_0$	Position vector of point (x_0, y_0, z_0) on the object's surface, which is imaged on pixel (0, 0)
$\mathbf{r}_e$	Position vector of point (x_e, y_e, z_e) where the illumination beam enters the object
$\mathbf{r}_s$	Position vector of a point (x_s, y_s, z_s), where scattered light exits the object
$\mathbf{r}_p$	Position vector of a point (x_p, y_p, z_p) along the centre of the p-th illumination beam
$\Delta\mathbf{r}$	Displacement vector or change of position vector $\mathbf{r}$
$\mathbf{S}$	Sensitivity matrix
S_p	Sensitivity vector for the p-th illumination beam
t	Non dimensional time or frame number index
$u(x, y, z), v(x, y, z), w(x, y, z)$	x, y and z components of the displacement vector $\Delta\mathbf{r}$
$\mathrm{W}(t)$	Window function
$\widetilde{W}(\hat{f})$	Fourier transform of window function $\mathrm{W}(t)$
$x\Lambda, \quad y\Lambda, \quad xy$	Cross-sections of the displacement data volumes
z_0	Depth of the point imaged at pixel (0, 0) relative to the zero optical path plane at $z=0$.
δz	Scattering layer thickness
α_p	Zenith angle that $\mathbf{n}_p$ subtends from the observation axis
β_p	Azimuth angle that $\mathbf{n}_p$ subtends from x axis
$\delta(\ )$	Dirac delta function

θ_{p}	Zenith angle of the p-th illumination beam
$\theta_{p'}$	Angle of refraction of the p-th illumination beam
λ_c	Central wavelength
ν	Laser frequency
ν_1, ν_2	Initial and final frequencies during laser scan
$\Delta\nu$	Laser frequency scan range
$\delta\nu$	Laser frequency step
ξ_{p}	Azimuth angle of the p-th illumination beam
$\boldsymbol{\Phi}$	Wrapped phase change vector
ϕ_{pj}	Wrapped phase difference between light scattered at the j-th slice when illuminated by the p-th beam, and the reference beam
ϕ_{sj}	Phase shift at zero nominal path difference due to a phase change on reflection or due to microscopically random arrangements of scatterers
ϕ_{0pj}	Phase difference at the origin between the light scattered at the j-th slice when illuminated by p-th beam and the reference beam
$\Lambda_{\mathrm{M\_eff}}$	Effective maximum allowed optical path difference
$\Delta\Lambda_{pj}$	Optical path length change due to deformation for p-th beam and for j-th scattering layer
Λ_{pj}	Optical path difference due to the p-th beam and for the j-th slice
Λ_M	Maximum allowed optical path difference
$\delta\Lambda$	Optical path resolution
γ	Constant that depends on the shape of the sampling window function W(t). γ=2, 4 for rectangular or hanning windows, respectively.
$()^{T}$	Transpose operator
$()^{-1}$	Inverse function or reciprocal operator

Abbreviations

AC	-	Auto-correlation
ACP	-	Anterior chamber depth
ADM	-	Absolute distance metrology
ADI	-	Absolute distance interferometer
ADL	-	Achromatic doublet
ADP	-	Adapter for holding three illuminations
AEL	-	Axial eye length
Al	-	Aluminium
AP	-	Absorber plate
APL	-	Adapter plate
AR	-	Antireflection coating
AS	-	Aperture stop
ASL	-	Anterior segment length
CADP	-	Camera adapter plate
CC	-	Cross-correlation
CST	-	Semiconductor tracker
CT	-	Computed tomography
CRO	-	Cathode ray oscilloscope
CXD	-	Coherence x-ray diffraction
CW	-	Continuous wave
DENSE	-	Displacement encoding method with stimulated echoes
DHM	-	Digital holographic method
DHPTV	-	Digital in-line holographic particle tracking velocimetry
DIC	-	Digital image correlation
DOCT	-	Doppler optical coherence tomography
DSPI	-	Digital speckle pattern interferometry
DVC	-	Digital volume correlation
ECDL	-	External cavity diode laser
ESA	-	European space agency
ESPI	-	Electronic speckle pattern interferometry
f	-	Focal length
FC/PC	-	Fibre connector / polish connector

FC/APC	-	Fibre connector / angled polish connector
FD-OCT	-	Fourier domain optical coherence tomography
FDS	-	Finite difference scheme
FE	-	Finite element
FEM	-	Finite element model
FEU	-	Finite element updating
FEMU	-	Finite element model updating
FFT	-	Fast Fourier transform
FF-OCT	-	Full-field optical coherence tomography
FF-SS-OCT	-	Full-field swept source optical coherence tomography
FOV	-	Field of view
FSI	-	Frequency scanning interferometry
GLI	-	Grid line interferometer
GPU	-	Graphics processing unit
I'	-	Image
ID	-	Iris diaphragm
LCI	-	Low coherence interferometry
LSCM	-	Laser scanning confocal microscopy
MAX	-	Measurement & automation
MI	-	Michelson interferometer
MRI	-	Magnetic resonance imaging
NA	-	Numerical aperture
ND	-	Neutron diffraction
NIR	-	Near infrared
O'	-	Object
OCE	-	Optical coherence elastography
OCT	-	Optical coherence tomography
OFDI	-	Optical frequency domain imaging
OF_R	-	Reference arm optical fibre
OF_1, OF_2, OF_3	-	Optical fibres for illumination beams 1, 2 and 3
OST	-	Optical scanning tomography
PIV	-	Particle image velocimetry
PBS	-	Pellicle beam splitter

PC	-	Personal computer
PC-MRI	-	Phase-contrast Magnetic Resonance Imaging
PC-OCT	-	Phase-contrast optical coherence tomography
PC-SOCT	-	Phase-contrast spectral optical coherence tomography
PDA	-	Photo detector array
PH	-	Pinhole
PM	-	Plane mirror
PLC	-	Planar lightwave circuit (optical fibre beam splitter)
PS-OCT	-	Polarisation sensitive optical coherence tomography
PS-OCE	-	Phase sensitive optical coherence elastography
PSF	-	Point spread function
PT	-	Photoelastic tomography
PTV	-	Particle tracking velocimetry
PVA	-	Poly vinyl alcohol
RF	-	Radio frequency
R.I.	-	Refractive index
RM	-	Reference mirror
S	-	Sample
SD-OCT	-	Spectral domain optical coherence tomography
SD-PS-OCT	-	Spectral domain polarisation sensitive optical coherence tomography
SLSI	-	Scattrered light sheet illumination
SMF	-	Single mode fibre
SrXmCT	-	Synchrotron x-ray micro computed tomography
SS-OCT	-	Swept source optical coherence tomography
SWIR	-	Short wave infra-red
TD-OCT	-	Time domain optical coherence tomography
TL	-	Tunable laser
TPB	-	Three point bending
TSI	-	Tilt scanning interferometry
USI	-	Ultrasound imaging
VCD	-	Vitreous chamber depth
VFM	-	Virtual fields method
VOI	-	Volume of interest
WFOCM	-	Whole field optical coherence microscopy

WSI	-	Wavelength scanning interferometry
XmCT	-	X-ray micro-computed tomography
XRD	-	X-ray diffraction
ZDL	-	Zero delay line
ZNCC	-	Zero normalised cross correlation
1-D, 2-D, 3-D	-	One-, two-, three- dimensional

List of Figures

CONTENT

Chapter 1

1 Introduction

1.1 Introduction

Sub-surface stresses are difficult to evaluate with current non-destructive testing methods of surface measurements. Often caused by delamination, moisture ingress, material mismatch or the anisotropic nature of the material, these stresses are required in order to assess the structural integrity of the component under test or to identify depth-resolved constitutive parameters to characterize the material and better predict its behavior. Examples in which surface measurements do not provide sufficient information include the localization and sizing of delaminations in composite materials [1-4] (as large and deep delaminations can show a surface deformation field similar to that of a small and shallow one), or the determination of stress propagation in granular packs, a truly 3-D spatial problem [5].

Another interesting case in which the behavior of the system is related to 3-D strain fields is ablative corneal surgery: following surgery, stresses may develop as a result of structural changes introduced by re-shaping of the corneal surface or the scarring process that follows. Current predictive models assume a uniform distribution of stiffness through the thickness of the cornea in order to estimate the final shape of the cornea after surgery (the target profile).

Identification techniques, aimed to evaluate material mechanical properties given known loads and measured displacement or strain fields, are bound to benefit from increased data availability (both in density and dimensionality) and efficient inversion methods such as finite element updating (FEU) and the virtual fields method (VFM) [6-8]. When all the orthogonal components of the displacement field (or all components of the strain tensor) are known at points closely spaced 'within' the volume of the material under study, inversion methods are more likely to identify a greater number of elements of the material's stiffness matrix. The last two decades have witnessed the development of a significant number of techniques that aim to provide 3-D multicomponent displacement fields.

Neutron diffraction and x-ray diffraction can provide 3-D strain fields in crystalline materials effectively measuring changes in the lattice parameter. Other techniques provide internal microstructure by some sort of tomographic imaging and can evaluate deformation fields using texture tracking methods based on digital image correlation (DIC) or digital volume correlation (DVC). Some examples include x-ray computed tomography (CT), ultrasound imaging, confocal microscopy, optical coherence tomography (OCT) (also known as OCT elastography when combined with digital image correlation (DIC) or DVC). Correlation methods are used to quantify displacement fields from before and after deformation of depth-resolved microstructure images. In all these cases the displacement sensitivity is coupled to the depth resolution, which constrains their ability to detect and quantify small deformations due to mechanical, thermal or chemical loads, in large fields of view. Phase sensitive techniques are powerful alternatives that are also able to provide 3-D microstructure and some displacement components or combination of principal strains: phase–contrast magnetic resonance imaging (PC-MRI), photoelastic tomography (PT), polarisation sensitive OCT (PS-OCT), Doppler and phase-contrast OCT, tilt scanning interferometry (TSI), and wavelength scanning interferometry (WSI).

Each technique has a restricted range of materials to which it can be applied: PT, for example, is suitable only for materials that exhibit transient photo-elasticity; PC-MRI requires significant water or fat content in the sample, and OCT techniques require the material to be

semi-transparent and able to scatter light usually in the infrared spectral region. For many technologically and medically important materials, the existing techniques often have insufficient spatial resolution or else are too insensitive. A detailed description of these techniques is presented in Chapter 2 with a comparative table that summarizes their main technical characteristics.

1.2 Novelty of research

Most OCT variants have evolved towards improving spatial resolution and acquisition speed and measuring the amplitude of the complex signal obtained, which describes the microstructural morphology of weakly scattering samples. Several depth-resolved interferometric optical techniques such as WSI, TSI and phase-contrast spectral OCT have been developed at Loughborough University as extensions of speckle pattern interferometry towards applications in mechanics of materials. The initial systems were able to provide only one or two depth-resolved displacement components through the thickness of polymer samples seeded with scattering particles. Their depth resolution was ~14mm, ~1.1mm, and 0.058mm respectively for the WSI [9], TSI [10] and PC-SOCT [11] systems.

A novel WSI system is proposed here, based on a broadband, near-infrared (NIR), telecommunications grade tunable laser and a 2-D NIR photodetector array. The system does not require spatial scanning and enables phase-contrast volume imaging with high spatial resolution. The interference signals from three non-coplanar illumination beams associated with three sensitivity vectors are recorded simultaneously using a frequency multiplexing approach. By comparing the phase data volumes before and after loading of the material, all the orthogonal components of the 3-D displacement field are readily obtained for each voxel in the resulting data volume. To the best of my knowledge, this is the first time that all orthogonal components of displacement have been measured within the volume of scattering materials. Other improvements over previous OCT systems include a ~100× increase in voxels count, a 3× increase in the number of displacement components measured, a displacement rms noise level of 0.14μm, 0.20μm and 32.5nm for the u, v and w displacement components respectively, with a comparable depth resolution of 0.060 mm and a lateral resolution of 0.025 mm.

1.3   Thesis structure

This Thesis is organized as follows: Chapter 2 presents a review of optical and non-optical techniques for 3-D full–field measurements of displacement and strain fields inside the volume of various materials and in the context of experimental mechanics. An overview of different identification methods which are used to evaluate material mechanical properties based on full-field measurements is also presented. Chapter 3 describes the initial developments of WSI and related techniques applied to experimental mechanics, profilometry and absolute distance measurements. Chapter 4 presents a detailed description of a novel full sensitivity WSI system, including optical setup, hardware synchronization scheme, the fundamental principle of WSI, the mathematical model used to describe it and a new approach based on frequency multiplexing that enables the simultaneous encoding of multiple measurements with different displacement sensitivities. In Chapter 5, data acquired for a reference opaque surface is used to evaluate the sensitivity vectors of the interferometer, rather than establishing them from approximate illumination and observation directions measured from the setup. The relationship between measured phase and calculated displacements is thus established in a convenient reference system. Chapter 6 presents experimental results of the 3-D distribution of the displacement field within a test sample that has undergone known rigid body in-plane rotation and out-of-plane tilt. All the components of the displacement vector at each voxel of the data volume are measured and compared to the nominal values of rotation and tilt introduced in the experiment via two rotation and tilt stages. Finally, Chapter 7 summarizes the research, provides a discussion on potential applications, sources of error and opportunities for further refinement and derives some conclusions.

1.4   Publications arising from the research

Chakraborty S., and Ruiz P. D., "Measurement of all orthogonal components of displacement in the volume of scattering materials using wavelength scanning interferometry", J. Opt. Soc. Am.A, 2012.**29**(9): p. 1776-85.

This journal has been selected by the Editors, for publication in the Virtual Journal for Biomedical Optics. http://vjbo.osa.org/virtual_issue.cfm.

Ruiz P. D. and Chakraborty S., "Full-sensitivity depth-resolved measurements of displacement fields inside weakly scattering materials using wavelength scanning interferometry", Proc. of SPIE, Vol. 8413, 84130D1-6, Speckle 12, V International Conference on Speckle Metrology, Vigo, Spain. [Received 'Best presentation and paper award']

Chapter 2

2 Measurement of three dimensional displacement and strain fields

2.1 Introduction

Volumetric imaging techniques can turn into powerful tools in experimental mechanics when combined with image correlation, tracking and registration methods to evaluate displacement fields. Their non-contact and full field approaches enable the study of the structural behaviour of complex materials from measurements of 3-D displacement and strain fields within their volume [12, 13]. Phase sensitive techniques constitute an alternative approach that do not require tracking or correlation to evaluate displacements, as they are obtained directly from phase differences measured from the signal that encodes depth information. Neutron and x-ray diffraction do not belong to these categories but provide volumetric maps of strain from

point wise measurements of diffraction peak shifts, scanned through the volume. A wide variety of techniques is quickly evolving to provide internal displacement fields in engineering materials (concrete, wood, metals, fibre reinforced composites, adhesives, polymers, gels, powders) and biological tissues (skin, tendons, muscle, arteries). This chapter presents a comparative analysis of current techniques by focusing in the following aspects:1) Working principles that lead to 3-D imaging; 2) Achievable spatial resolution (axial and lateral); 3) The way in which displacement is evaluated; 4) Displacement and strain sensitivity; 5) Materials for which they are suitable and 6) Advantages and limitations of the different implementations. This analysis, presented within the context of identification in mechanics of materials, is aimed to better appreciate the strengths and weaknesses of the new WSI approach proposed in this Thesis.

2.2   Evaluation of mechanical properties of materials

Results from predictive analytical or numerical models of material behaviour are only as good as the mechanical properties and boundary conditions that are used and also depend on the validity of the considered assumptions. Establishing the parameters that characterize material behaviour is therefore paramount, and is the main purpose of so called "identification techniques". In general terms, for a material under mechanical load, identification techniques use measured values of the applied load and the resultant displacement (or strain) field to find the mechanical properties of the material. These properties are usually the elastic modulus, Poisson's ratio or in general cases the components of the stiffness tensor [6, 14]. Finite element model updating (FEMU) is a common iterative approach in which the displacement or strain at certain points in the material are evaluated using a forward model using some initial guess for the mechanical properties. A cost function that compares the predicted strain field with the measured one is written in terms of the mechanical parameters to be identified. These parameters are then found by minimizing the cost function. FEMU can handle a large variety of over-determined data [15].

Another approach, based on the concept of virtual work and known as the virtual fields method (VFM), has been proposed in 1989 [16] and evolved ever since to solve more challenging identification problems, in part fuelled by advances in imaging and full field non-contact optical measurement techniques. VFM has been used mainly with 2-D displacement and strain measured fields to study [8]: a) bending stiffness in thin anisotropic plates, b) shear

bending on rectangular coupons, c) non-linear shear behaviour and damping effects in composites, d) elasto-plasticity of materials (a plane dog bone shaped) and e) heterogeneous stiffness fields in woods and impacted composite plates [7].

In solid mechanics, due to the advent of powerful computation methods and experimental techniques, the mechanical behaviour of the materials can be characterised precisely by comparing the results obtained from experiments and theoretical models. The constitutive equation plays a key role in identifying the structural behaviour of the materials under study. In case of 'direct inversion' method for homogeneous and isotropic materials, there is always a direct link that connects the unknown parameters and the measurements (such as local displacements, strain, applied loads, etc.), but for heterogeneous anisotropic or plastic materials, no such straightforward relationship remains between them [17].

2.3   Neutron diffraction & X-ray diffraction

Diffraction methods in solid state physics date back to the early 20th century along with Bragg's law of diffraction [18]. Neutron diffraction (ND) and x-ray diffraction (XRD) can provide 3-D non-destructive strain fields within the volume of crystalline materials, effectively measuring changes in the lattice parameter (atomic plane spacing) due to plastic and elastic deformations caused by stress. They require long acquisition times for each measured point (usually several minutes to hours, depending on the beam intensity) and rely on spatial scanning to build up 3-D data volumes [19]. As neutrons interact with the atomic nucleus, the scattered intensity is directly proportional to the isotopic structure and they are weakly absorbed by most materials, which give them good penetration in metals (a few centimetres). One area that has benefited from 3-D ND, for instance, is rail quality and maintenance. The repeated rolling contact between railway track and wheels lead to a complex and asymmetric strain distribution and ultimately gives rise to contact induced plasticity and fracture [20-23]. Figure 2.1 illustrates a typical ND measurement of strain spatial distributions. In this case, the residual plastic strain for transverse, vertical and longitudinal components are mapped in a cross section of a rail head [23]. Volumetric data could be acquired by further scanning of the measurement point (indicated by a cross '×' in the figure) along the rail axis (the longitudinal direction). The gauge volume (the selected volume of the sample where the measurements are made) can be as small as $0.5{\times}0.5{\times}0.5mm^3$.

The strain levels in this case were within -1600 and 800 microstrain with levels of 100 microstrain being easily distinguishable.

X-ray diffraction relies on the interaction of X-rays with the electron cloud surrounding the atoms. Modern synchrotron sources provide high energy, coherent, polarized and collimated X-ray radiation, which reduces measurement time, increases penetration depth to a few tens of micrometres and increases spatial resolution and strain sensitivity. The strain distribution within the volume of nano-crystalline materials can only be studied by coherent x-ray diffraction (CXD) [24, 25]. Figure 2.2 shows a beautiful example in which x-ray diffraction is used to measure 3-D strain fields within a Pb nano crystal. The gauge volume can be as small as $0.11 \times 0.11 \times 0.11 \text{mm}^3$. The maximum strain component measured due to the +1.4rad phase shift of the complex density which corresponds to a total displacement of 0.08nm.

Though very powerful in crystalline materials, the main limitation of ND and x-ray diffraction methods is that they do not work in amorphous materials such as glass, polymers and some tissues.
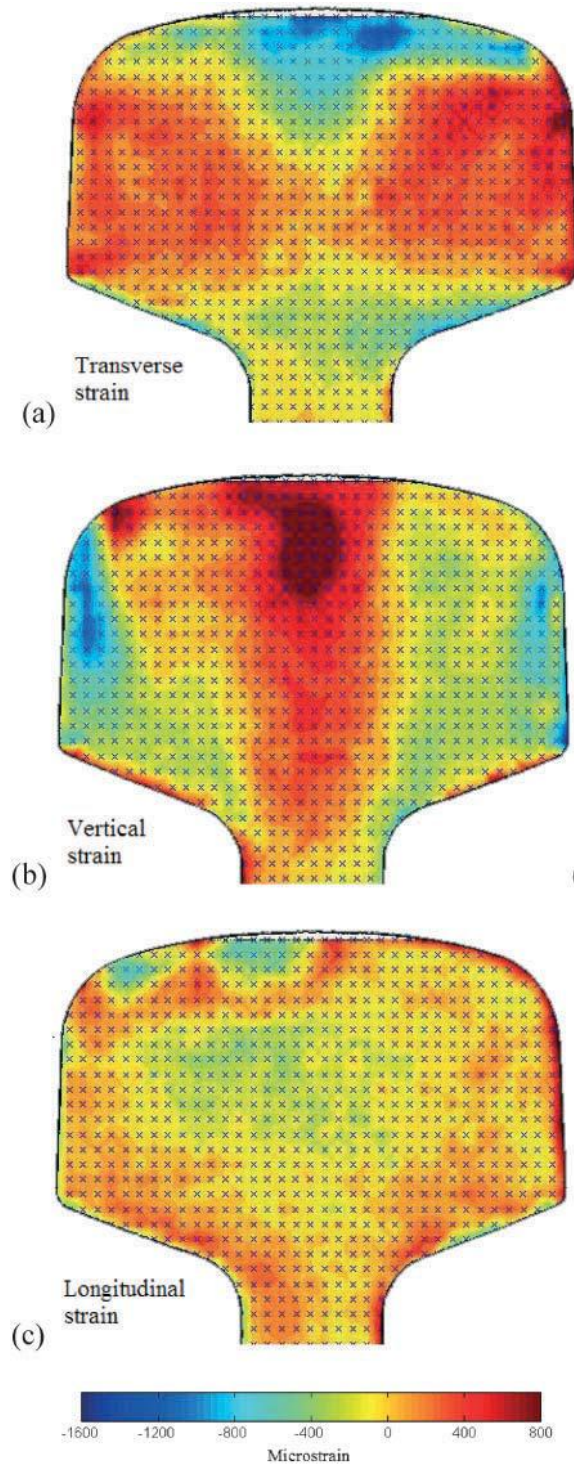
Figure 2.1 Distributions of the residual elastic strain components in a rail measured with ND. (a) transverse, (b) vertical, and (c) longitudinal [23].
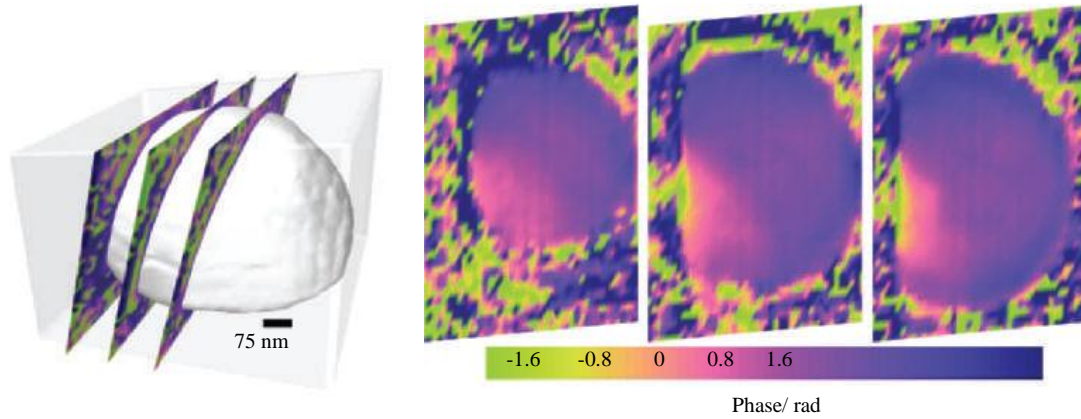
Figure 2.2 Strain distribution within a Pb nanocrystal and cross sections of cut-planes passing through an isosurface of the density of the Pb nanocrystal studied with coherence x ray diffraction (CXD) [25].

2.4   3-D magnetic resonance imaging

Magnetic resonance imaging (MRI) is primarily a medical imaging modality mostly used in radiology to visualize detailed internal structure and function of the body, especially useful in neurological (brain), musculoskeletal, cardiovascular and oncological (cancer) imaging. It uses a powerful magnetic field to align the nuclear magnetization of (usually) hydrogen atoms in water in the body. Radio frequency (RF) fields are used to change the alignment of this magnetization in a systematic way, causing the hydrogen nuclei to develop a rotating magnetic field perceptible by the scanner.

A micro MRI method coupled with 3-D 'finite-element based' DIC has been used to study the cancellous bone of bovine femoral head under compression and 3-D displacement and strain uncertainties were calculated for different correlation subsets [26]. A slice of 16 mm long and 10 mm^2 cross-section was extracted from a sample like femoral head and field of view (FOV) $40\times20\times20mm^3$ was limited by the MRI antenna. The displacement fields were measured over a volume of $96\times192\times96$ voxels or $7.5\times15\times7.5mm^3$ volume of interest (VOI), where the strain level was -0.6 microstrain and the displacement uncertainty was ~ 8mm in all three directions.

In another study, MRI has been used in conjunction with a zero-th order and a first-order texture correlation algorithms, i.e. 2-D DIC, to evaluate 3-D deformation fields inside intervertebral disc tissue [27]. The spatial resolution achieved here was $256\times256\times64$ voxels

where each voxel is ~ 78μm^3. The axial strain levels were -9.55% ± 2.59% and -9.07% ± 2.71% for two different slices and radial strains were 0.17% ± 0.83% and -0.14% ± 0.52% for them.

Gilson *et al* in 2005 [28] developed a multi-slice displacement encoded with stimulated echoes (DENSE) MRI method along with the 3-D motion encoding capability for determining the 3-D myocardial mechanics and they applied their method on the mice heart in case of pre and post infarction. The intra-myocardial displacement, strain and torsion everything can be evaluated by DENSE MRI, which takes only 50 minutes for a complete scan. In 2008, Avril *et al* used displacements measured by stimulated echo MRI in conjunction with the virtual fields method to estimate the stiffness ratio between an inclusion and its surrounding medium in a phantom [29]. The volume of interest of the sample was 50×50×42mm^3, where the average value of modulus in surrounding material was 0.69 and within the inclusion it was 2.98.

2.5   Digital volume correlation

It seems convenient at this point to introduce a brief description of correlation techniques, as they are central in a significant number of techniques that will be introduced in this Chapter. Image correlation techniques such as DIC for 2-D and DVC for 3-D datasets are becoming ubiquitous in mechanics of materials, material research and biological sciences due to the simplicity of their working principle, enabled by advances in imaging techniques and algorithm design for stereo photogrammetry and tomography [30-32]. Essentially, DVC works by tracking how a spatial region in a 3-D dataset moves and deforms from a reference state to a deformed state. The method relies on the local "texture" within a sub-region of Q^3 voxels (Q~20-40), ideally a random "speckle" field, which is matched and tracked by minimizing a correlation parameter. The result from such minimization is a set of parameters that include the displacement vectors and higher order derivatives of the displacements used to improve the matching. This is repeated for specific points in the data volume laid out as a grid [33]. The strains are finally obtained for points in the grid by estimating the surrounding deformation gradients. The size of the local region, Q, thus determines the displacement and strain spatial resolution for independent measurements. One important characteristic of DIC and DVC is that the spatial resolution is coupled to the size of the field of view (FOV), or the magnification of the imaging system. This is so because displacements are measured in

fractions of pixels (DIC) or voxels (DVC). The spatial scale is determined by the size of the imaged region or FOV. Fig. 2.3 illustrates how DVC works. Here a single point was considered for analysis at the position P, the displacement of P was defined by t.

In DVC the two consecutive images before and after the deformations need to be divided into a set of sub volumes and those sub volumes can be centred on the different points of interest. The local displacement vector can easily be evaluated at each point from each pair of corresponding sub volume images by using a 3-D volume correlation method where the 3-D discrete correlation function is generally computed by 3-D fast Fourier transform (FFT) algorithm. The FFT is the easiest method to evaluate the cross-correlation functions by replacing the double summation using a point-wise multiplication which reduces the computational cost.
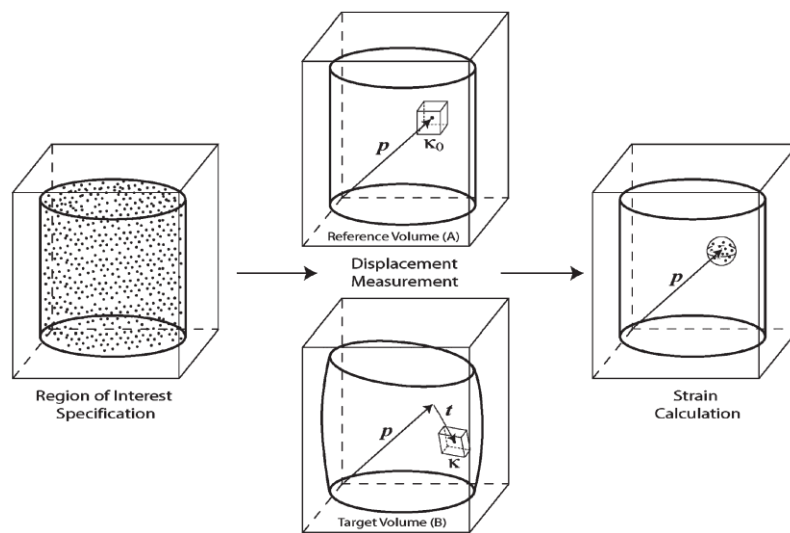
Figure 2.3 Digital volume correlation involves: (a) specification of a region of interest in the microstructure data volume; (b) displacement measurement at each location by correlation of reference and target data volumes; and (c) strain calculation at each point by estimation of the surrounding deformation gradients [31].

2.6 3D particle image velocimetry

3-D particle image velocimetry (PIV) dominates in the area of experimental fluid mechanics for measuring multi-component velocity vectors at a large number of points inside a measurement volume filled by a particle-seeded fluid. The technique consists of four different stages –see Fig. 2.4: 1) stereo imaging of the measurement volume with 2 or more

13

cameras. The fluid is usually illuminated by a high power visible laser; 2) stereoscopic localisation (based on an epipolar-line or crossing-line method) to get the three position coordinates of the particles); 3) calibration (to compensate for lens distortions and aberrations) and 4) matching or tracking algorithm (DIC or DVC). Though originally used in 2-D sections of the flow, 3-D versions of PIV methods have been proposed and demonstrated over two decades ago [34, 35], leading to the determination of the 3-D components of the velocity field within the flow volume [36]. It was from the field of PIV that experimental mechanics adapted the correlation and tracking algorithms to measure material strain rather than velocity fields. While in PIV the particles need to be sparse and resolved to be successfully tracked, in the experimental mechanics variants, DVC methods work better when the volume is filled by a non-sparse random texture field, not necessarily fully resolved as long as the fundamental condition is met (as discussed in the last paragraph of section 2.5).

There is a holographic version of PIV in which the amplitude and phase components of the scattered wave and reference wave are stored in a hologram as an interference pattern, while the replica of the reference wave is generally used again to illuminate the hologram to reconstruct the original wave field. Micro digital in-line holographic particle tracking velocimetry (micro-DHPTV) was demonstrated for evaluating 3-D velocity vector fields at distinct points inside the volume of a flow in conjunction with combined 3-D cross correlation and nearest neighbour matching algorithm [37]. At the time of reconstruction of the hologram, the scanning depth was 50μm, the number of image slices 100 and the resolution ~ 0.5μm. In a straight micro channel flow, 507 vectors were obtained with velocity ranging from 0.002 to 0.025 m/s. Comparing with all different PIV techniques, it can be said that HPIV is superior to all other methods where the coherent volumetric illumination is required to record the holograms. Their applications is limited nowadays only in the area of simple flow configurations because of the complicated experimental setups and complex data analysis techniques.

All the components of the velocity field can be measured with a 3-D holographic PIV technique in which in-line digital holograms of particle seeded volumes are recorded from different directions, reconstructed and then analysed by with a 3-D cross correlation algorithm [38]. In this experiment the seeded particle with a diameter of 11μm had been sandwiched between two microscopic slides and placed on x–z micrometer traverse. The technique was called as 'two single-exposed digital in-line holography' where in between the

two exposures, the seeded particles were moved by 0.1mm and 0.06mm in *x* and y directions respectively, i.e., a vector displacement was of 0.1166 mm and standard uncertainty was of 4.29%. Red blood corpuscles have been successfully tracked in the flow inside a micro-tube using digital holography and PIV [39]. The reconstructed volume was $600 \times 350 \times 350 \mu m^3$ containing 185 RBCs and the maximum measured velocity ~ 5.96mm/s and mean velocity ~ 2:98mm/s.
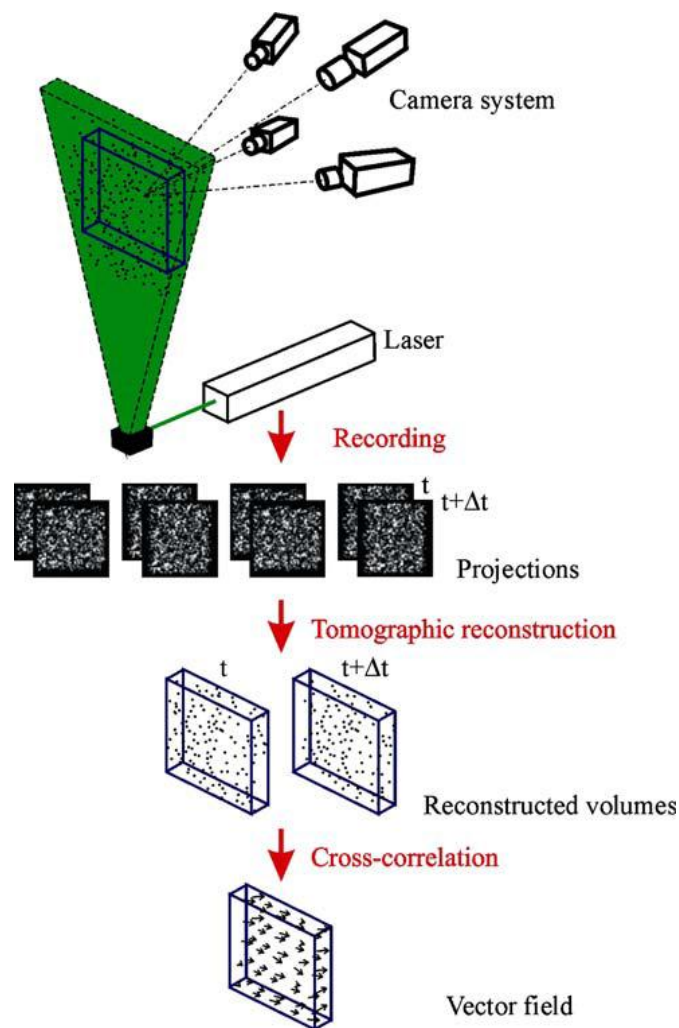
Figure 2.4 3-D PIV [40]

2.7 DVC & 3D x-ray computed tomography

DVC has been used on data volumes acquired with a diverse range of techniques to evaluate 3-D deformation fields in a variety of materials and x-ray computed tomography (CT) is perhaps the most popular one among them. Unlike x-ray diffraction, CT is based on measurements of the absorbance of X-rays by the material. Some examples of evaluation of 3-D deformation fields using a combination of DVC and CT include: compressed breast mimicking phantoms [41]; propagation of fatigue cracks in cast iron [42]; interior of silicon rubber phantoms [43]; human cancellous bones [44]; trabecular bones [45, 46]; wood specimens [47]; propagation of micro-cracks in murine cortical bones [48]; granular beds of sugar packs [49]; polypropylene solid foams [50] and rock specimens [51]. Germaneau *et al* in 2008 [52], applied DVC on data volumes acquired with XmCT and also with optical scanning tomography (OST). They compared the two methods in terms of their displacement uncertainties in case of rigid body translations and measured strain in a localised compression test. From a number of different experiments it has been seen that the volume of interest obtained from the sample was on the order of $10 \times 10 \times 10 \text{mm}^3$ and the standard deviation error in displacement was calculated on that selected volume was on the order of few µm.

2.8 DVC & 3-D scattered light sheet illumination

DVC has been used on 3-D data volumes obtained with 3-D scattered light sheet illumination (SLSI) imaging. Transparent polymer phantoms made of epoxy resin and polyurethane seeded with particles of different sizes were deformed and their 3-D structure reconstructed [53, 54]. The correlation volume used was $31 \times 31 \times 31$ voxels^3 and the displacement uncertainty along the *x*, *y* and *z* were 0.015 voxel (0.9 micron), 0.015 voxel (0.9 micron) and 0.058 voxel (3.5 micron) respectively. The strain uncertainty was 0.00075, 0.00075 and 0.0029 respectively.

2.9 DVC & 3-D ultrasonic imaging

Changes in strain can also be evaluated from ultrasonic echo data before and after compression of the material. Axial strain (in the direction of ultrasound propagation) has recently been computed in pressure ulcer mimicking phantoms from their in-plane and out-of-plane motions [55, 56]. 3-D data volumes, assembled from a stack of 2-D images acquired before and after a small change in elasticity of the phantom under compressive load, were processed with a DVC algorithm. Displacements of ~0.6mm were measured for a 2% deformation. In another case, DVC and 3-D ultrasound imaging were combined to evaluate displacement and strain distributions within breast tissue mimicking phantoms with an inclusion [57]. The inclusion diameter and also the ratio between the elastic modulus of the inclusion and of the surrounding medium were calculated.

The main drawback of the ultrasound volume imaging technique is its low resolution, time consuming computational techniques and processing of each section of the elastograms approximately by one hour using a standard personal computer, because the solution is based on the finite difference scheme (FDS) and due to the presence of higher derivatives in the propagation equations. On the other hand, the Fourier domain approach is better and can speed-up the simulation by decreasing the higher order derivatives. Presently the graphics processing unit (GPU) plays an important role in the image processing and breaks down the complex system into many small tasks, and processes them simultaneously to speed up the simulations [58].

2.10 DVC & 3-D laser scanning confocal microscopy

Laser scanning confocal microscopy (LSCM) provides 3-D data volumes of transparent materials with internal beacons, such as cell cultures with fluorescent markers in agar gel. Confocal microscopy increases the axial resolution of conventional microscopy by using a pin hole (confocal to a point that scans the object) in front of the detector that filters out defocused light. In the visible spectrum and using an objective with numerical aperture NA= ~0.6, the lateral and axial resolutions correspond to ~ 0.25 to 0.8µm and 0.5 to 1.5µm respectively. LSCM has been recently combined with a DVC algorithm based on the fast Fourier transform for finding out the internal strain map of the extracellular matrix under

uniaxial compression [59]. In another study, these techniques were used for evaluating 3-D displacement and strain fields within the whole volume of an agarose gel phantom blended with fluorescent markers [60]. The DVC algorithm was formulated using a 3-D zero-normalised cross correlation (ZNCC) technique based on the fast Fourier transform and a 3-D sum table scheme to minimize the correlation computation time. The migration pattern of fibroblasts (approximate speed of 8 µm/hour) on the surface of polyacrylamide gels embedded with red microspheres (0.5 µm radius) and the corresponding displacement in the underlying gel substrate was also studied with DVC and LSCM [61]. The dynamical tracking and the quantification of cellular forces in cellular matrices in 3-D spatial axes were determined by volumetric LSCM image stacks coupled with a DVC algorithm. A cell induced deformation as a function of depth within the volume of the sample was plotted and the displacement maps of gel substrates with varying thicknesses were compared.

The field of view (FOV) achieved in LCSM was $\sim 230 \times 230 \times 230 \mu m^3$ and the lateral strain without stretch correlation were 0.8×10^{-2}, 1.1×10^{-2}, and axial strain was -9.25. With stretch correlation the lateral strains were -3.6×10^{-2}, -7.8×10^{-2} and axial strain was -9.34.

2.11 DVC & 3D optical coherence tomography

Optical coherence elastography (OCE) is another non-invasive modality with a strong clinical approach for finding out mechanical parameters of biological tissues (muscle, skin, cornea, tumours, intravascular tissues, etc.) [62, 63]. 2-D and 3-D optical coherence tomography (OCT) reconstructions are combined with DIC or DVC for calculating displacement and strain fields. Inversion methods then follow to evaluate the constitutive parameters of the material under study.

Briefly, OCT is an interferometric technique based on a broadband light source with a short coherent length. The modulation of the interference signal finds a maximum when the optical path between object and reference beams in the interferometer lies within the coherence length of the source. If this 'coherence gate' is scanned axially and laterally through the object (which has to be semi-transparent and weakly scattering) then a volume reconstruction with the microstructure of the object is obtained [64]. The Swept source OCT (SS-OCT) system from Thorlabs Ltd. can work in the near infrared (NIR) spectral region with a central wavelength of $\lambda_c=1310nm$ and a spectral bandwith of $\Delta\lambda=50nm$. It can only image the 2-D

and 3-D microstructure of the sample with lateral and axial resolutions of 25μm and 12μm in air and 25μm and 9μm in water, respectively. DIC or DVC has to be applied to the 2-D or 3-D images respectively, before and after the loading, for the evaluation of the 2-D or 3-D displacement fields at each pixel/voxel of the sample.

DIC is used to track spatial features which are part of the material microstructure of the object to sub-pixel accuracy [65]. In the last 15 years mainly 2-D displacement and strain fields were estimated by applying the 2-D cross correlation tracking algorithms on the pre and post-deformed 2-D OCT images, such as in a collagen model of the African frog tadpole (Xenopuslaevis) [66], in tissue mimicking gelatin phantoms and atherosclerotic arterial samples [67], in bilayered poly-vinyl-acrylate tissue phantoms [68], in silicone-based tissue phantoms and in human breast tissue [69], in bilayer RTV silicone phantoms embedded with titanium oxide particles and human skin [70], in 27 silicone tissue-mimicking phantoms (with different elastic moduli) under uniaxial compression [71], and in skin tissue mimicking phantoms made of poly-dimethyl-siloxane seeded with titanium oxide powder [72]. Here in this study of skin tissue mimicking phantoms [72], direction and site dependent mechanical properties were measured by accessing the different surface waves having separate frequencies and the Young's moduli were evaluated by solving wave equations.

In phase-contrast OCE (PC-OCE), phase changes occurred due to displacement of the scattering centres inside the tissue are measured [69]. By noting the time delay between two successive depth-resolved scans, depth-resolved velocity of the tissue in the direction of the illumination beam can be determined from the measured value of phase-change which leads to the evaluation of strain rate and also total displacement. The volume of the silicone tissue phantoms used for the experiment was $10 \times 16 \times 10 \text{mm}^3$ (*x-y-z* directions) and elastic moduli were calculated for the tissue phantoms and human tissues at different organs of the human body.

In 2010 an interesting analysis of the mechanical behaviour of an aeronautical spherical plain bearing model made of epoxy resin was presented, where DVC was coupled with 3-D optical scanning tomography (OST) and the measured displacement uncertainty was 0.1 voxel ~ 0.006mm and strain value ~ 0.005 which were compared with finite element (FE) predictions [73].

In 2011 Kennedy *et al* [74] demonstrated a spectral OCT based 3-D OCE system on hydrated and normal skin where the elastic properties of the tissue have been estimated at different strain rates. In the tissues, the deformation occurs at a particular rate termed as a strain rate which is commonly used in ultrasound elastography and as well as in OCE, in order to differentiate tissues based on elastic properties.

2.12 3-D polarisation sensitive OCT

Polarisation sensitive OCT (PSOCT) relies on the photoelastic effect (transient birefringence), in which orthogonal polarizations propagate with different speeds within the material under stress. The retardation between them is proportional to the difference of the principal strains in a plane perpendicular to the direction of light propagation. PSOCT provides depth-resolved distributions of birefringence, optical axis orientation, phase retardation, and principal strain difference [75]. It is effectively a type of reflection mode photoelasticity that uses reflected or back scattered light.

In 2010, Stifter *et al* [76] interrogated the polarisation pattern changes inside the polymer volume sample during the tensile and fracture tests and evaluated the internal strain map by the combination of Spectral domain PSOCT (SD-PSOCT) method and advanced image processing algorithms at 1550 nm wavelength range.

The main limitation of PSOCT is that it only measures the difference between the principal strains that are perpendicular to the observation direction. Another drawback is that highly birefringent materials are required to provide a detectable retardation for small deformations as the penetration depth in OCT is usually not greater than 3 mm, i.e. a short distance for the orthogonal polarizations to build up retardation. So far it seems that no studies with PSOCT have been combined with inversion methods for identification purposes. Figure 2.5 shows a glass fibre composite deformed to fracture. Notice the amount of deformation required to produce a small retardation change.
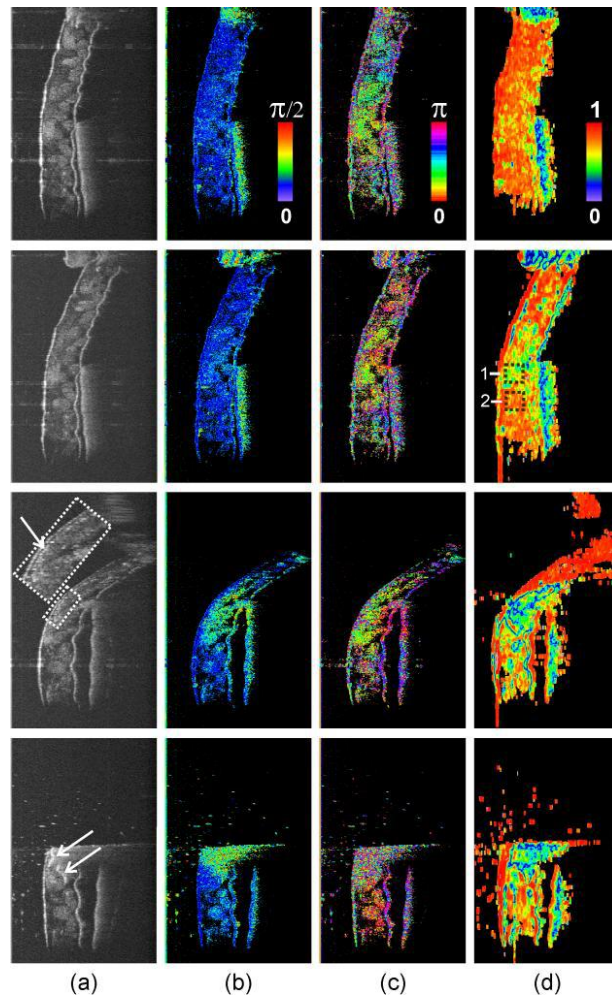
Figure 2.5 Single-frame excerpts from spectral domain PSOCT recordings of a glass-fibre composite during fracture. (a) Intensity; (b) colour-coded retardation; (c) colour-coded optical axis orientation; (d) colour-coded degree of polarization uniformity. The single spots in the bottom images correspond to debris flying off the sample during fracture [75].

2.13 3-D photoelastic tomography

Tomographic photoelasticity can measure the stress tensor inside the volume of 3-D transparent materials depending upon the retardation between different polarization components as light propagates through it. Careful experimental measurements and inversion algorithms are required to retrieve all the components of the stress tensor [77]. In 2002, Tomlinson *et al* [78] proposed and designed a tomographic polarimeter, based on birefringence effects, to measure the stresses in transparent or semi-transparent biological

tissues and engineering materials. However, no further studies or measurements have been reported so far. The continuous wave (CW) He-Ne laser of 632nm wavelength, a Sony XCD 710 machine version standard camera with maximum resolution 1024×768pixels and speed of 30 frames per second, a 5µm pinhole and a 60× microscopic objective were used to image an epoxy resin cube with dimensions $25×25×25mm^3$. A typical full tomographic measurement cycle (72×36×6 images = 15552 images, i.e. 72 images for the Fourier polarimetry, 5º interval of the specimen rotation stage and 6 views) was conducted in 4.5 hours and images were then processed to obtain 36×6 sets of three characteristic parameters, which were used for tomographic reconstruction.

2.14 3-D phase-contrast OCT

A family of optical phase-contrast OCT techniques (PC OCT) [79] have recently emerged where both the amplitude and the phase of the back scattered light from the sample are measured. By comparing the phases between two successive scans, the axial displacement of the sample along the direction of the light beam can be calculated. If the time between successive scans is known then the velocity can be obtained and the techniques are referred to as Doppler OCT [80]. In blood flow applications, Doppler OCT proved effective to measure blood flow inside 0.3 mm vessels, with velocities in the range (-18 mm/s to + 18 mm/s [81].

PC OCT has the ability to measure deformations of soft tissues and displacement fields inside the volume of scattering materials without requiring birefringence, as opposed to PSOCT or tomographic photoelasticity [82, 83]. This is a great advantage when small strains need to be measured as the technique possesses interferometric displacement sensitivity. PC OCT provides depth-resolved displacements within the volume of scattering materials. There is fundamentally no distinction between Doppler OCT and PC OCT; both measure changes in phase, the only difference being the time between scans (roughly ms or sub ms range for Doppler OCT and several seconds or minutes for PC OCT).

Different implementations of PC OCT were reported in the last few years, the most common being spectral PC OCT systems based on a broadband source and spectral detection. The first system proposed (as shown in the figure below) was used to measure axial displacements in cross sections of porcine corneas due to changes in intra-ocular pressure [11].
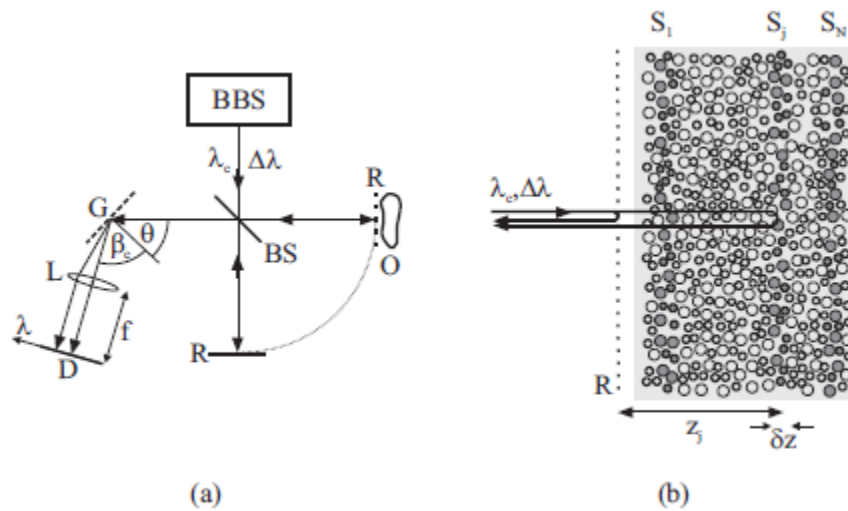
Figure 2.6 (a)Schematic of a SOCT set-up and (b) the cross section of the sample used in the set-up. The SOCT system consisting of a broadband source (BBS), beam splitter (BS), object (O), reference mirror (R) (apparent position is shown by a dashed line), diffraction grating (G), lens (L) of focal length (f), 2-D photo detector array (D),the incident angle of the broadband beam (θ) for the central wavelength (λ_c) and the diffraction angle (β_c) at λ_c.[11].

In the Fig 2.6(a) the optical set up of SOCT has been shown and the cross section of the sample is shown in Fig. 2.6(b), where the sample has been considered as consisting of a set of 'slices' of equal thickness having the depth resolution of δz. As a result time resolved wrapped phase maps were obtained that indicated the corneal deformations (up to 420nm compression between epithelium and endothelium) due to creep after a small change in the intra-ocular pressure. A later system was extended to provide the axial and one in-plane displacement components simultaneously. This was achieved by using symmetric oblique illumination. In-plane and axial displacement fields were mapped through the thickness of a polymer phantom [84].

In 2009, Wang *et al* [82] demonstrated a Phase-contrast optical coherence elastography (PCOCE) approach on a bilayer tissue phantom made from Poly-vinyl-alcohol (PVA), to characterize the heterogenous structure of the tissue that subjected to a deformation of micron order. During the cyclic loading period the OCE system continuously displayed the velocity, displacement, strain rate, and cumulative strain maps of the phantom at an imaging rate of 10 frames/s. Here Fig. 2.7(a) shows the direction of load, Fig. 2.7(b) represents the phase-change maps between two successive scans, Fig. 2.7(c) shows the smoother phase map, Fig. 2.7(d), (e) and (f) describes the localized velocity map, strain rate map and instant strain map

respectively. The system sensitivity was measured as 5.1mrad and minimum resolvable deformation was measured as 0.26nm when the average refractive index of the tissue was taken as 1.3.
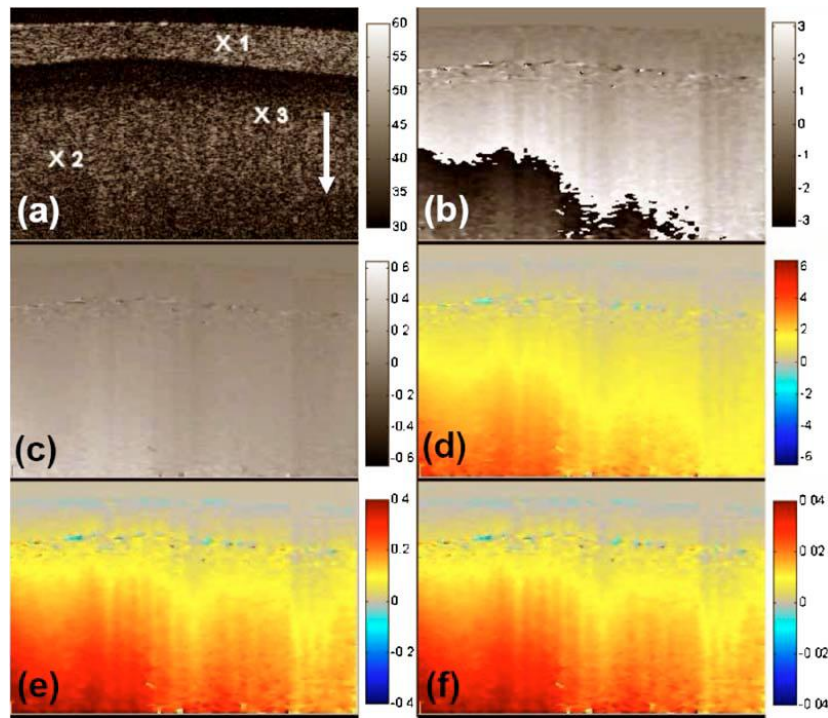
Figure 2.7 Characterization of the tissue mechanical properties of a bilayer phantom using Phase sensitive optical coherence elastography (PSOCE) system at the time instant of t=5 s under a slow dynamic compression. (a) OCT structural image (physical size of the image is 1.3×2.2mm^2 (depth×width)) (dB), (b) wrapped phase map determined by the PSOCE (radians), (c)-instant tissue deformation map calculated from (a) after the application of unwrapping algorithm (μm), (d) localized velocity map (μm/s), (e) instant strain rate map (%/s), and (f) instant strain map (%) [82].

2.15 Wavelength scanning interferometry

We finally arrived to wavelength scanning interferometry (WSI), the technique that forms the core of this Thesis. WSI is a type of PC OCT that is not based on a spectrometer as previous realizations. It relies on a tunable laser (or swept source) to record a sequence of 2-D interferograms from which depth resolved information can be extracted. It can be thought of as a parallel version of Swept-source OCT (SS-OCT) [79] as all pixels are recorded simultaneously for each wavelength (rather than a sequence of wavelength scans for each

lateral position in the FOV). In this section, several equivalent techniques that emerged each with a different name are presented. Even though there are no fundamental differences between them, one may be tempted to consider otherwise due to variations in their implementation, application fields and diverse measuring ranges.

2.15.1 Wavelength and frequency tuning for OCT reconstructions

Optical coherence tomography (OCT) is an exciting technique that was first demonstrated more than two decades ago, by Huang *et al* in 1991 [85]. It is based on a Michelson interferometer and a low temporal coherence broadband source that provides 1-15μm depth resolution in 2-D and 3-D microstructure images of materials primarily in biological tissues for medical applications [86], whereas standard clinical ultrasound imaging provides 0.1 to 1mm depth resolution. The technique when implemented in the time domain detection mode, i.e. Time domain OCT (TDOCT), the reference mirror is scanned to provide cross-sections of the sample. It can also be realised in the Fourier domain detection mode, i.e., Fourier domain OCT (FDOCT) demonstrated by Fercher *et al* in 1995 [87] with greater speed than TDOCT because of its simultaneous measurement procedure of intensity from all scattered back signals with no axial scanning devices in the interferometer model [64]. Spectral domain OCT (SDOCT) is one form of FDOCT where all the information of a slice inside the material is registered simultaneously by using a spectrometer and an array of photo-detectors. The depth of the material is encoded as spatial frequency along the wavelength axis or wave-number axis (so called k-axis) of the spectrometer. Material-microstructure is then extracted from the spectral magnitude of the Fourier transformed data along the k-frequency axis.

Swept source OCT (SSOCT), also known as Optical frequency domain imaging (OFDI), is another approach that uses a narrow bandwidth source which can sweep its frequency as a single fast photodetector is used to record the interference signal modulation. This signal is then Fourier transformed to retrieve a depth scan. Galvo-scanners are then used to perform depth scans at different locations across a plane perpendicular to the viewing direction.

Wavelength scanning interferometry (WSI) is effectively a SSOCT system where images of the object are recorded sequentially by a 2-D photo detector array while tuning the

wavelength. WSI has become a widespread imaging tool due to successive improvements in tunable lasers in the last 15 years. Its history dates back to the discovery of the radar system using a saw tooth frequency sweep by Hymans *et al* in 1960 [88]. The period between 1981 and 1997 saw the emergence of fibre-optic frequency-domain reflectometers, simple noncontact wavelength-shift interferometers and 2-D OCT, all based on wavelength scanning. Fibre-optic frequency-domain reflectometry was first described by Eickhoff *et al* around 1981 [89] where a He-Ne laser was tuned over its line-width, the back scattered light was detected as a function of spatial frequency of the laser and Fourier transformed data revealed the scattering distribution. A simple noncontact wavelength-shift interferometer using a single mode laser diode along with phase-shifting technique was developed by Sekine *et al* in 1992 [90] for axial eye length measurement with a measurement range of 16-32 mm. The technique showed lower measurement accuracy than other techniques that used partially coherent light. In 1996-1997 Chinn *et al* [91] produced 2-D OCT images of a thin glass sandwich structure as a preliminary demonstration of the system's depth and resolution capabilities. They used a swept frequency source (external cavity laser with a super-luminescent LED) with 0.1nm spectral steps around 840nm in a 20nm bandwidth. They produced depth profiles at different lateral positions and achieved a depth resolution of 38μm and a depth range of 8mm. Lexer *et al* described the basic principles of WSI and its application in ophthalmology [92] see Fig. 2.8. They studied a model eye with high resolution and human eyes in vivo with low resolution using an external-cavity tunable diode laser with 780nm central wavelength which had two wavelength-tuning modes: a coarse tuning mode over full wavelength range (25 nm) and the fine tuning mode (0.18 nm) which lead to depth resolutions of 11μm and 1.5mm, respectively. They could measure three separate optical depths within the eye model such as Anterior segment length (ASL) = 10.5mm, Vitreous chamber depth (VCD) = 24.8mm and Axial eye length (AEL) = 35.3mm. Kerbage *et al* in 2007 [89], presented a 3-D rapid large depth range imaging technique of the anterior segments of the human eye (13.4 ×12 × 4.2mm in 1.4 seconds) by OFDI. The tunable source scanned from 1217 to 1356nm with an average output power of 60mW providing an axial resolution of 10μm in air.
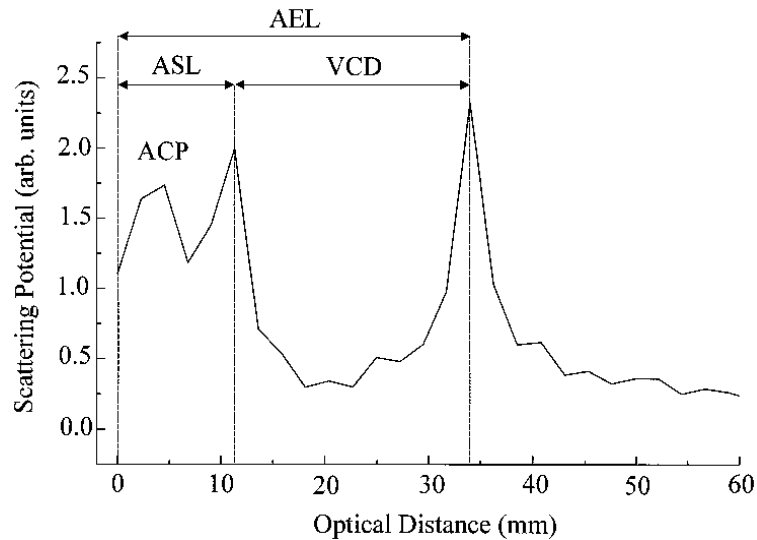
Figure 2.8 Wavelength scanning interferometric scan of a human eye *in vivo,* ASL-anterior segment length; VCD-vitreous chamber depth; AEL-axial eye length; ACP-anterior chamber depth [92]

Full-field swept-source optical coherence tomography (FF-SS-OCT) was demonstrated by Mehta *et al* [93] based on coaxial common-path optical interferometry with a frequency sweeping broadband low coherence light source. A stack of 2-D interferograms were recorded along the wavelength axis and images of composite materials and also phase maps were reconstructed at different depths. They presented their detected intensity in *k*-space and a 3-D rendering algorithm was used to reconstruct the volume to get structural information, defects at different depths, etc. In 2009 Mehta *et al* [94] proposed applications of FF-SS-OCT in forensic sciences and materials such as epoxy, silicon microelectronic circuits, composites, etc. Izatt *et al* [95, 96] contributed significantly to ophthalmology by designing a whole-eye optical coherence tomography system. They could image the retina and the anterior segment of eye simultaneously with an axial resolution of 10μm and lateral resolution of 30μm.

2.15.2 WSI in profilometry

For the last 15 years some examples of simultaneous measurement of shape, optical thickness variation, multiple surface testing, refractive index homogeneity were done by wavelength scanning interferometry which include the combination of different type of tunable light sources with interference signal and data processing approaches, i.g., to measure the real time

surface shape and height of specular and diffuse surfaces of step objects [97], flatness of transparent plates [98], shape of reflecting plane surfaces [99], variation in surface shape and optical thickness of nearly parallel plates [100], surface and thickness of transparent thin film layers [101,102], thickness of a wedge shaped sample [103] and profiles of thin wafers less than 100μm thick [104] and thus is well suited for thin wafer inspection.

2.15.3 WSI in absolute distance measurement

In the past 25 years, various wavelength sweeping interferometric methods were developed to perform absolute distance measurement over several meters to overcome the 2π-ambiguity of conventional laser interferometers. Absolute distance measurement techniques using light have a variety of industrial application areas starting from small measurement domains such as thin wafer inspection to large distance measurement jobs such as measurement of a few meters to kilometres in the geodetic and extra-terrestrial fields. Distance using light is measured by three basic processes. For large distances of more than a few kilometres, a pulse propagation time technique is generally used based on measuring the total time taken by an extremely small sharp focussed spot while moving from the source to end point and returning back to the source [105]. The phase measuring technique is used for measuring the distance in the range of a few meters to kilometres, which compares the phase of the modulating signal reflected back from the target to the emitted light and for measuring the shorter distance interferometer with coherent source is generally used. In 1986, Kikuta *et al* [106] proposed a novel distance measuring technique over several millimetres range by using wavelength scanning method of a laser diode on rough surfaces. Measurement of optical length of Fabry-perot etalons were done by few scientists of National Physical Laboratory, UK 1993 and 1998 [107,108]. In 1998, a frequency scanning method was developed by Xiaoli *et al* [108] to measure distances up to 4 mm with an accuracy of 3 nm. A variable synthetic wavelength absolute distance interferometer also developed by Bechstein *et al* [109] to measure few metres absolute distance in the machine and plant construction area with 10 micron measurement uncertainty within very short time (~5 seconds).

In absolute distance metrology (ADM), frequency scanning interferomety (FSI) flourished due to the emergence of tunable external cavity diode lasers (ECDL) that can be swept continuously in the frequency domain. FSI based sensors are relatively simple to handle and

flexible with different suitable configurations and only rely on the frequency sweep range. Cabral *et al* [110] implemented a FSI based Fabry-Pérot interferometer made by mode-hop free frequency sweep ECDL and a dual measurement system to measure a distance of 150 m with an accuracy of tens of microns in the context of the ESA-PROBA3 mission (Coronagraph and demonstration of metrology for free-flying formation, European Space Agency).

In 2002, Coe *et al* [111] developed an FSI system for absolute distance measurement to track the shape changes of the semiconductor tracker (CST) placed at the centre of ATLAS, the largest particle detector at the Large Hadron Collider at CERN, Geneva. They made this FSI with a wavelength scanning tunable laser where tuning has been done in the frequency domain. They used FSI in this project along with geodetic grids containing 842 grid line interferometers (GLI) of different lengths ranging from 30mm to ~1.5m. High precession was required when all interferometers were working simultaneously to monitor the shape of particle tracker with 10 micron accuracy in three dimensions [112-116].

Following that, in the period of 2005-2008 a better FSI system was proposed by Yang *et al* in terms of estimating the vibration effects and error sources. They described a plan to use it for the alignment of tracker elements of electron positron linear collider detectors [117-119] .
Metrology is an essential part of planned scientific missions of the European Space Agency in projects like: (a) gravitational wave detection, (b) X-ray telescopes, (c) synthetic aperture telescopes, (d) Darwin infrared space interferometer containing 6 free-flying telescopes with a central satellite to detect planets around stars. All deal with high accuracy complex metrology systems to align all components so that they operate as a single instrument [120]. An Absolute distance interferometer based on FSI with a single tunable laser was made by Swinkels *et al* to measure the absolute distance between two satellites with an uncertainty of around 10 μm over a distance of 250 m. According to the principle, their system measures phases before and after a frequency sweep and by counting the number of fringes during the sweep, the absolute path length difference can be calculated without ambiguities (as long as no fringes are missed). Since the wavelength at the endpoints of the sweep is generally stabilized by a Fabry-Perot cavity, the measured distance is directly related to the length of the cavity.

2.16 Depth-resolved out-of-plane displacement measurement using WSI

The first WSI system used to measure the axial displacement of a stack of optically smooth glass air interfaces was presented by Ruiz et al [9]. A second paper by the same authors demonstrated that the principle worked also for a stack of scattering surfaces [121].These systems were based on a tunable diode laser with a narrow tuning range of 0.116nm that lead to a depth resolution of 14mm. The FOV was determined by the NA of the imaging system and it was ~10×10mm^2. However, as displacement sensitivity is decoupled from the spatial resolution, the displacements were measured with interferometric sensitivity. Out-of-plane displacement was under 317 nm. The light source used was a solid-state tunable laser (New Focus Vortex 6005) and a high-speed camera VDS HCC-1000 (1024 × 1024 pixel sensor with 10 μm × 10 μm pixel size) was used for recording the interference patterns.

WSI fully relies on a tunable laser source with broad tunable range and the sample has to be kept mechanically stable when it is exposed to different wavelengths sequentially, i.e., during the whole period of scan [79, 122].
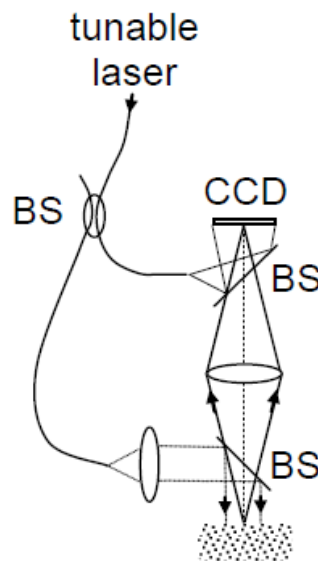
Figure 2.9 WSI setup- measurement of depth-resolved displacement fields with phase sensitivity [122].

The main advantage of the technique proposed by Ruiz *et al* [121] was the decoupling of displacement sensitivity from depth resolution (as in OCT + DVC approaches) and the absence of a spatial scanning mechanism in the interferometer. The main disadvantage was that they could not tune the laser linearly in the frequency domain. Recently in 2012, Davila

et al [123] described the suitability of a Ti:Sapphire laser in a WSI system with >100 nm scan range which allowed high speed scans of significant number of frames (> 50000) at a rate of 30fps, with a linear frequency scan. A detailed description of WSI as it was originally proposed together with an analysis to develop a new system is presented in Chapter 3. A novel system that provides all the components of the displacement field is described in Chapter 4.

2.17 Tilt scanning interferometry

Finally, it is worth mentioning tilt scanning interferometry (TSI), another PC-OCT like technique able to provide depth-resolved amplitude and phase. The fundamental difference between TSI and all other previous OCT methods is that it uses a monochromatic light source. Depth information is encoded in the frequency of the interference signal by continuously changing the angle of the illumination beam during image acquisition. A temporal sequence of monochromatic speckle interferograms is recorded that leads to 3-D reconstructions of the microstructure and the phase of the object. Displacement fields with one in-plane and out-of-plane sensitivity were measured within an epoxy beam [10]. The depth resolution of the system was measured as 1.1mm for a tilting range of 0.0048rad and a gauge volume of $0.028 \times 0.028 \times 1.1 \text{mm}^3$. The depth range of the system was measured as 7.8 mm.

It is interesting to note that confocal microscopy, WSI, TSI and OCT techniques can all be described in a common mathematical framework as linear filters in 3-D space [122, 124].

2.18 Concluding remarks

In this Chapter, different non-contact 3-D volume imaging techniques were discussed, together with methods to extract displacement and strain information from the recorded data volumes. Non-optical techniques included MRI, ND, X-ray CT and USI, all of which have found niches of applications in life sciences and engineering. Among the optical techniques the following were discussed: PIV, SLSI, LSCM, OCT, PS-OCT, PT, PC-OCT, OCE, SS-OCT, WSI, FSI, and TSI. In this optical methods, displacement and strain information can be extracted essentially by three different methods: 1) texture tracking methods based on correlation methods such as DIC and DVC, 2) measurement of phase delay between

orthogonal polarization components as light propagates in a birefringent material, and 3) phase contrast methods in which phase is proportional to displacement.

In the context of this Thesis, "close competitor techniques" can be considered those optical techniques which aim to measure displacement fields in the volume of scattering materials with: 1) high displacement sensitivity, 2) as many displacement components as possible, and 3) high spatial resolution of the displacement field. Techniques that rely on speckle tracking with DVC (e.g. OCT elastography –Section 2.11) do not satisfy 1 and 3, but satisfy 2. Phase sensitive OCT elastography satisfies 1 and 3 but so far systems have provided sensitivity only to the axial displacement component. Sensitivity to the axial and one lateral displacement was achieved with phase contrast OCT in 2D cross sections (Section 2.16). Polarization sensitive OCT, which relies on material birefringence to measure in-plane strain, does not satisfy 1-2, but can provide high spatial resolution of the strain field (Section 2.12). The WSI approach presented in this Thesis and described in Chapters 3 and 4 addresses all points 1-3 and is not aimed to compete in terms of spatial resolution with ultra-high resolution OCT techniques.

WSI, FSI, SS-OCT and OFDI are all fundamentally the same technique. They aim to measure the optical path difference of an interferometer by scanning either the laser wavelength or frequency in one direction continuously and measuring the resulting accumulated phase shift. As frequency, rather than wavelength, is conjugate to the optical path difference variable through the Fourier Transform, regular frequency intervals are required during the scan for a correct reconstruction of the depth profiles. If the wavelength is scanned with regular intervals, however, resampling (at regular intervals) of the interference signal is required prior to the Fourier transform to avoid peak broadening.

In this Thesis a novel method of phase contrast WSI is proposed to determine all the 3-D orthogonal components of the displacement vector in each voxel of the data volume. This is achieved by simultaneously measuring the interference signal produced for different illumination directions during a wavelength scan. In the next chapter the working principle of WSI is described and some design considerations are discussed to build the interferometer.

Chapter 3

3 Wavelength scanning interferometry

3.1 Mathematical description of WSI

Let us consider the simple diagram of a Michelson interferometer (MI) in Fig. 3.1 for normal illumination and observation. The interferometer contains a tunable laser as source, a beam splitter, reference and sample arms and finally the detector for capturing the interference pattern. The working principle can be developed by considering the phase difference between sample and reference arms which depends on the optical path difference while the source

wavelength changes at a constant rate. The zero delay line (ZDL) represents the apparent position of the reference mirror along the sample arm.
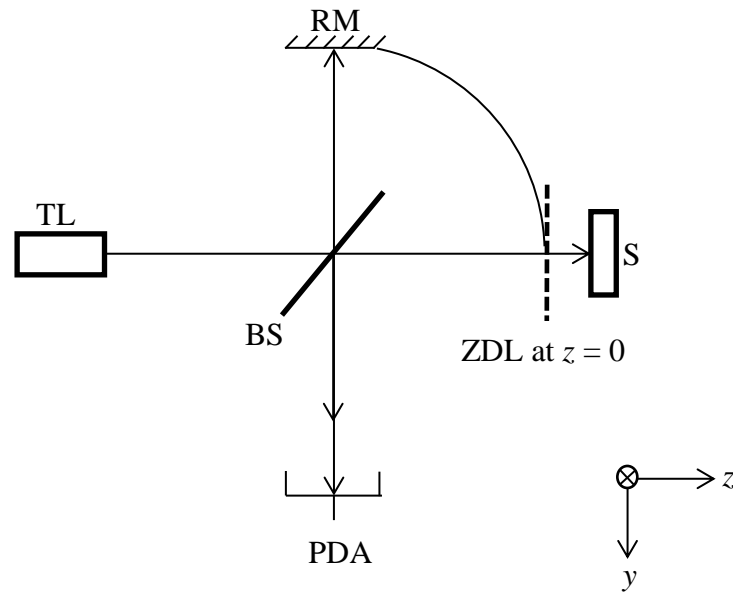
Figure 3.1 Michelson interferometer (MI) – a basic diagram of WSI, where TL- tunable laser; S- sample; ZDL- zero delay line; RM- reference mirror; BS- beam splitter; PDA- photo detector array;

3.1.1 Interference signal, phase and modulation frequency

The mathematical description of WSI presented here has been derived from previous work of Ruiz *et al* [9, 79, 121, 125]. Consider the layout shown schematically in Fig. 3.1. At $z = 0$, the same path lengths of reference and sample arms from BS result in a zero phase difference. Let the sample be modelled as a set of N_s discrete thin scattering layers parallel to its surface, illuminated by a beam of wavelength λ which varies with time and is partially reflected from different layers of a semi-transparent sample. It is assumed that multiple reflections are neglected within the layers of the object and the back scattered light is imaged onto a pixel of a photo-detector array with indices (m, n). The intensity due to the interference of the sample and the reference wavefronts can be written as

$$I(m,n,t) = |A_0(m,n,t) + \sum_{j=1}^{N_s} A_j(m,n,t)\exp[i\phi_j(m,n,t)]|^2$$

(3.1)

where A_0 represents the amplitude of the reference wavefront and A_j (j=1, 2, … N_s) is the amplitude of the wavefront scattered at the j-th slice of the object when it is illuminated by the normal illumination and i is the complex number ($i=\sqrt{-1}$). ϕ_j is the phase difference between light scattered at the j-th slice and the reference beam. The spatial indices m and n on the detector are m= 0, 1, 2, …,N_m-1; n= 0, 1, 2, …, N_n-1 and t is a non-dimensional time defined as the true time divided by the camera interframe time. Expanding Eqn. (3.1) and dropping the (m, n, t) dependence in all the amplitude and phase variables in right hand side of the equation for clarity gives

$$I(m,n,t) = A_0^2 + \sum_{j=1}^{N_s} A_j^2 + 2\sum_{j=1}^{N_s-1}\sum_{l=j+1}^{N_s} A_j A_l \cos(\phi_j - \phi_l) + 2A_0 \sum_{j=1}^{N_s} A_j \cos\phi_j \qquad (3.2)$$

The right hand side of Eqn. (3.2) consists of four terms. The first two correspond to dc terms and term 3 represents interference between the light scattered back from the j-th and the l-th layers. Together, terms 2 and 3 are referred as the autocorrelation terms (AC). Term 4 represents the interference between the scattered light from each of the different j-th slices and the reference beam, and is referred to as the cross correlation term (CC). This last term contains the information about the microstructure of the sample.

The phase ϕ_j can be represented as

$$\phi_j(m,n,t) = \phi_{sj}(m,n) + k(t)\Lambda_j(m,n) , \qquad (3.3)$$

where ϕ_{sj} is a phase change induced on reflections from the rough surfaces of the sample or due to the microscopically random arrangements of scatterers at the j-th slice contributing to the amplitude at pixel (m, n), i.e. the phase that leads to speckle noise. $k(t)$ is the wave number $2\pi/\lambda(t)$, a function of time t and Λ_j is the optical path difference due to the normal illumination beam scattered back from the j-th slice and the reference beam. The j-th slice lies at a depth $z=z_0+(j-\frac{1}{2})\delta z$ below the sample's surface, δz being the layer thickness.

Wavelength scanning interferometry involves changing k with time over a total range Δk, while image sequences are recorded using the 2-D photo-detector array.

$$k(t) = k_c + \delta k t \tag{3.4}$$

Where k_c is the central wavenumber, δk is the increment in wavenumber between successive frames and t is from $-\Delta k/2\delta k$ to $+\Delta k/2\delta k$. Substitution of Eqn. 3.4 into Eqn. 3.3 leads to

$$\phi_j(m,n,t) = \phi_{sj}(m,n) + k_c \Lambda_j(m,n) + \delta k \Lambda_j(m,n)t , \tag{3.5}$$

The linear variation of $\phi_j(m,n,t)$ with t leads to an intensity modulation frequency $f_{\Lambda j}(m,n)$ in units of "cycles per frame" which is directly proportional to the path difference between the light beams scattered back from j-th slice and the reference wavefront:

$$f_{\Lambda j}(m,n) = \delta k \Lambda_j(m,n)/2\pi \tag{3.6}$$

An alternative frequency can be defined in units of "cycles per scan duration"

$$\hat{f}_{\Lambda j}(m,n) = f_{\Lambda j} N_t = \Delta k \Lambda_j(m,n)/2\pi \tag{3.7}$$

where N_t is the number of frames and measuring frequency $f_{\Lambda j}$ or $\hat{f}_{\Lambda j}$ provides a measure of $\Lambda_j(m, n)$, which can be used to locate the coordinates of scatterers on the surface and within the bulk of the sample. Moreover, if two scans are performed before and after a deformation of the sample, then provided ϕ_{sj} remains the same between scans, the phase changes $\Delta\phi_j (m, n, 0)$ provide a direct measure of the change in optical path lengths $\Delta\Lambda_j(m, n)$ due to the deformation.

3.1.2 Extraction of the sample micro structure

Both the microstructure and phase change of surface scatterers can be evaluated by a time-frequency analysis. The Fourier transform of the interference intensity signal $I(m, n, t)$ in Eqn. (3.2) can be written as an infinite sum over an integer index that locates identical spectra N_t samples apart in the frequency domain. The goal of the measurement is to reconstruct the amplitude $A_j (m, n)$ and the 3-D distributions of phase $\phi_j(m, n)$ of the scattered light field

from each of the N_s scattering layers. If no aliasing is present, then the Fourier transformed data of the intensity in Eqn. (3.2) may be written as

$$\tilde{I}(\hat{f}) = \tilde{W}(\hat{f}) * \left\{ \begin{array}{l} \left(I_0 + \sum_{j=1}^{N_s} I_j \right) \delta(\hat{f}) + \sum_{j=1}^{N_s} \sqrt{I_0 I_j} \exp(\pm i\phi_{0j}) \delta(\hat{f} \mp \hat{f}_{\Lambda j}) \\ + \sum_{j=1}^{N_s-1} \sum_{l=j+1}^{N_s} \sqrt{I_j I_l} \exp[\pm i(\phi_{0j} - \phi_{0l})] \delta[\hat{f} \mp (\hat{f}_{\Lambda j} - \hat{f}_{\Lambda l})] \end{array} \right\} \tag{3.8}$$

where * represents convolution, $\tilde{W}(\hat{f})$ is the Fourier transform of W(t), a continuous window function that represents the finite sampling duration and the envelope of the laser power spectrum. The first term between curly brackets in Eqn. (3.8) is part of the autocorrelation term and represents the dc term due to the reference and scattered wavefronts. The second, known as the cross-correlation term, represents the interference between the reference beam and the illumination beam scattered at all layers within the sample and is given by the superposition of Dirac deltas δ that fall within bands in the frequency domain between frequencies $\hat{f}_{\Lambda p1}$ and $\hat{f}_{\Lambda pNs}$ which are, according to Eqn. (3.7), proportional to the optical paths Λ_{p1} and Λ_{pNs} corresponding to the first and last layers. The phase at the origin of each of these frequency components is given by $\phi_{0j} = \phi_j(m, n, 0)$. It is represented by Dirac deltas at frequencies $(\hat{f} \mp \hat{f}_{\Lambda j})$ (the amplitude of this cross correlation term is mentioned in 4th term of Eqn. (3.2)). The third term of Eqn. (3.8), again known as autocorrelation, represents the interference between pairs of scattering layers due to the same illumination beam. It is represented by Dirac deltas at frequencies $\pm(\hat{f}_{\Lambda j} - \hat{f}_{\Lambda l})$. Before the application of the Fourier transform, the mean value of the intensity signal is subtracted and the signal is multiplied by a Hanning window.

3.1.3   Calculation of interference phase

When $\hat{f} = \hat{f}_\Lambda$, $\tilde{I}(\hat{f})$ from the Eqn. 3.8 takes the complex value (as discussed in the section 2.3.1.2 of [79]),

$$\tilde{I}(\hat{f}_\Lambda) = \sqrt{I_0 I_j} \tilde{W}(0) \exp(i\phi_0) \tag{3.9}$$

37

The temporal phase shift calculated from the real and imaginary parts are written as,

$$\phi(0) = \tan^{-1}\left\{\frac{\mathrm{Im}\left[\tilde{I}(\hat{f}_\Lambda)\right]}{\mathrm{Re}\left[\tilde{I}(\hat{f}_\Lambda)\right]}\right\} \tag{3.10}$$

3.1.4 Range and resolution of the optical path difference measurement

The maximum allowed optical path difference depends on the Shannon sampling theorem, which states that in order to get adequate sampling of the $I(x, y, t)$ signal, the phase difference ϕ should not change by more than π between successive t values, i.e. 2 samples per each cycle which led to

$$\Lambda_M = \frac{\pi}{\delta k} \tag{3.11}$$

where, Λ_M is the maximum allowed optical path difference and δk is the increment in wavenumber axis in between two consecutive frames.

The optical path length resolution is measured by the width of the peak in the Fourier domain which is frequency difference between two neighbouring peaks of at least twice the distance from their centres to their first zero. In the case of single scattering surface the optical path resolution is

$$\delta\Lambda = \gamma\,\frac{2\pi}{N_t\delta k} \tag{3.12}$$

and the depth resolution along the z-axis is

$$\delta z = \gamma\,\frac{2\pi}{n_1 N_t\delta k} \tag{3.13}$$

where N_t is the number of frames, δk is the step in wavenumber, n_1 is the refractive index of the material of sample and γ takes a value of 2 for rectangular window and 4 for Hanning window [79]. In case of a bulk sample under oblique illuminations (rather than normal, for instance, as described above) the equation modifies to

$$\delta\Lambda = \gamma \frac{\pi}{n_1 \cos(\theta_{p'}/2)N_t \delta k} , \tag{3.14}$$

where n_1 is the refractive index within the material, $\theta_{p'}$ is the angle of refraction at the air/medium interface and γ takes 2 for rectangular window and 4 for a Hanning window as before [79].

Considering the above equations from Eqn. (3.3) to Eqn. (3.14), it is possible to plot the recorded intensity against different axes and the axes can be transformed from frame number to spatial frequency of the laser (v) or to the wavelength (λ) or to the wave number (k) etc. Here one example of axis transformation is shown in the figure below. The intensity I can be plotted against the frame number N_t and as well as along the wave number k axis. The Fourier transformed intensity data $\hat{I}$ can be plotted along the frequency axis $\hat{f}$ in the units of cycles per scan duration and finally against the depth axis z (following the Eqn. 3.7). The depth resolution is shown schematically in Fig. 3.2(d).
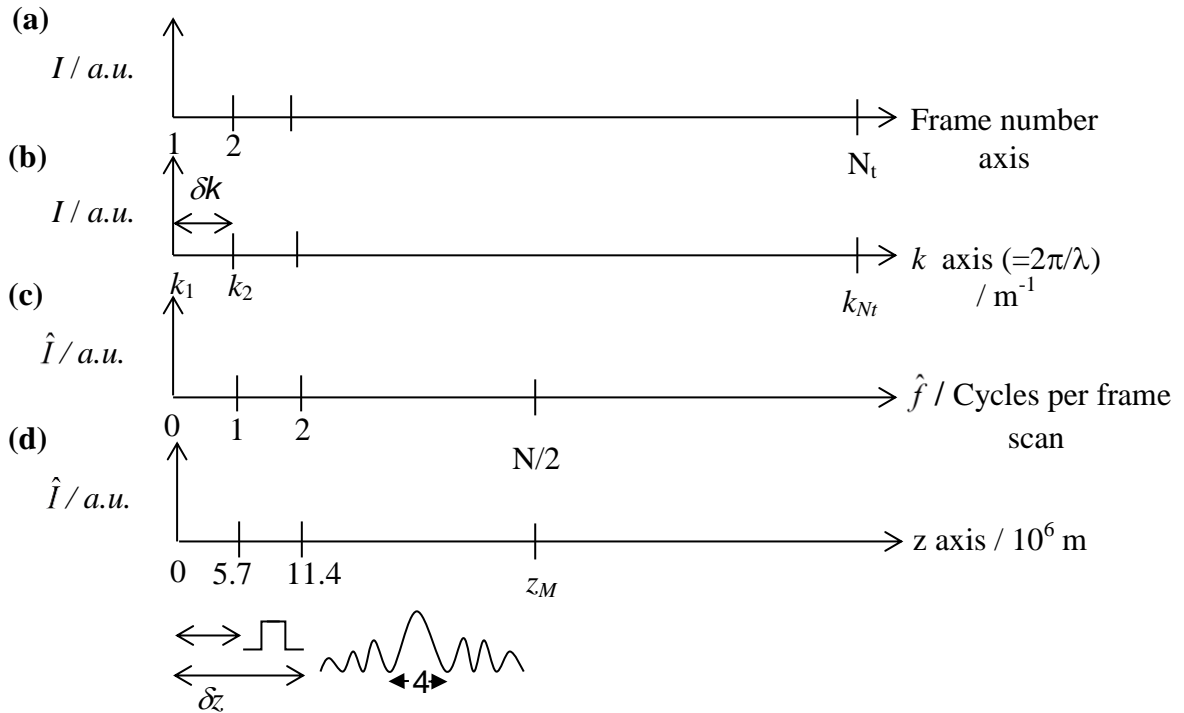
Figure 3.2 Transformation of axes. (a) Intensity I plotted against the frame number N_t, (b) along the wave number k-axis, (c) the Fourier transformed intensity data $\hat{I}$ plotted along the frequency axis $\hat{f}$ and (d) against the depth axis z.

3.2 Novel WSI system based on a telecom laser and an InGaAs detector array

In this section a WSI system based on a near infra red (NIR) tunable telecom type laser and NIR camera are described and tested in a simple experimental configuration. These will be used as the building blocks for the full sensitivity system derived in Chapter 4.

3.2.1 Light source of the WSI

TSL-510 (type A) from Santec Ltd. can perform continuous, mode-hop-free sweeps over its full 100nm tuning range with low noise and excellent stability. It is a class-3R external cavity laser (50mW power). Working wavelength is 1260-1360nm with 1310nm central wavelength and 100 nm bandwidth. The laser was connected to the input of 2×2 fibre coupler through an FC/APC fibre connector, which was present on the front panel of the laser. A BNC-BNC cable was connected in between trigger signal output terminal of the laser on rear panel and trigger input terminal of the NIR detector for synchronising their operation. The main advantage of this laser is that its frequency can be tuned linearly. The laser has excellent wavelength characteristics with repeatability of ±10 pm and the stability of ±5 pm. It can be tuned in two modes, either in sweep or step mode with a maximum speed of 100nm/sec. The laser can be tuned in the wavelength domain with a minimum step of 0.001 nm, as well as in the frequency domain with a minimum step of 0.0002 THz. The output beam can be fed directly into the single mode fibre (SMF) through a FC/APC fibre connector. As the laser emits in the 1260-1360 nm range, a special high resolution InGaAs camera is required.
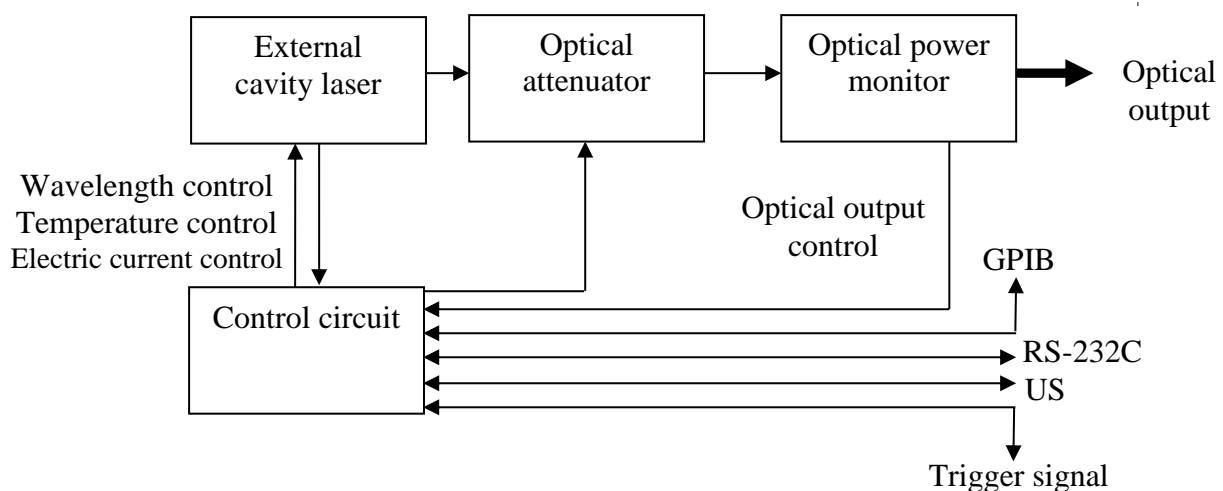
Figure 3. 3 Block diagram of TSL-510 tunable laser [126]

40

The TSL-510 type A, has four main parts (1) external cavity laser, (2) optical attenuator, (3) optical power monitor and (4) an electronic control circuit- see Fig. 3.3 [126]. The external cavity laser is contains a diffraction grating, mirror, lens, laser diode and an isolator. The angle of the mirror is changed to tune the lasing wavelength. The laser diode is maintained at uniform temperature to achieve stable oscillation.

3.2.2 NIR photo-detector array

As the laser works in the near infrared (NIR) range, it is impossible to use silicon based sensors for imaging purposes, because their working wavelength is below 1125 nm. Hence, a special high resolution NIR camera (SU640SDV-1.7RT/RS170 InGaAs, Goodrich Corporation, USA) was used, with a spectral sensitivity in the 900-1700 nm range, compatible to spectral emission of the laser source [127]. The SUI SWIR Digital Video (SDV) camera family offers a set of compact, versatile imaging tool with high resolution and sensitivity. It is based on an Indium Gallium Arsenide (InGaAs) focal plane array (FPA) with 640×512 pixels on a 25μm pitch grid and a maximum framing rate of 30 frames per second. The FPA requires a minimum dead time of 123μs and the maximum exposure period is 33.2ms. It provides sensitivity over an extended NIR range because of its lower band gap, which increases the dark current to ~400 e-/pixel/sec in the full wavelength range 900-1700nm.

Offset correction, gain correction, and pixel substitution were controlled using ASCII commands through a Camera Link asynchronous serial communication port. A 'Camera-link Terminal' software and 'SUI-Image Analysis 3 +' software were used for sending these ASCII codes.

3.2.3 Data processing hardware/software

An IMAQ PCI -1428 frame grabber card from National Instruments with camera link cable was used for image acquisition. The IMAQ PCI-1428 NI frame grabber card was installed with the 'Measurement & Automation (MAX)' software. An interface file was written in MAX and enabled the acquisition of images. 'Cameralink Terminal' & 'SUI-Image Analysis 3+' software were used to set camera parameters and interface file in MAX. Images were

acquired and accessed through MATLAB image acquisition toolbox. Hence, image processing was also done using MATLAB.

3.2.4 Timing and synchronization diagram
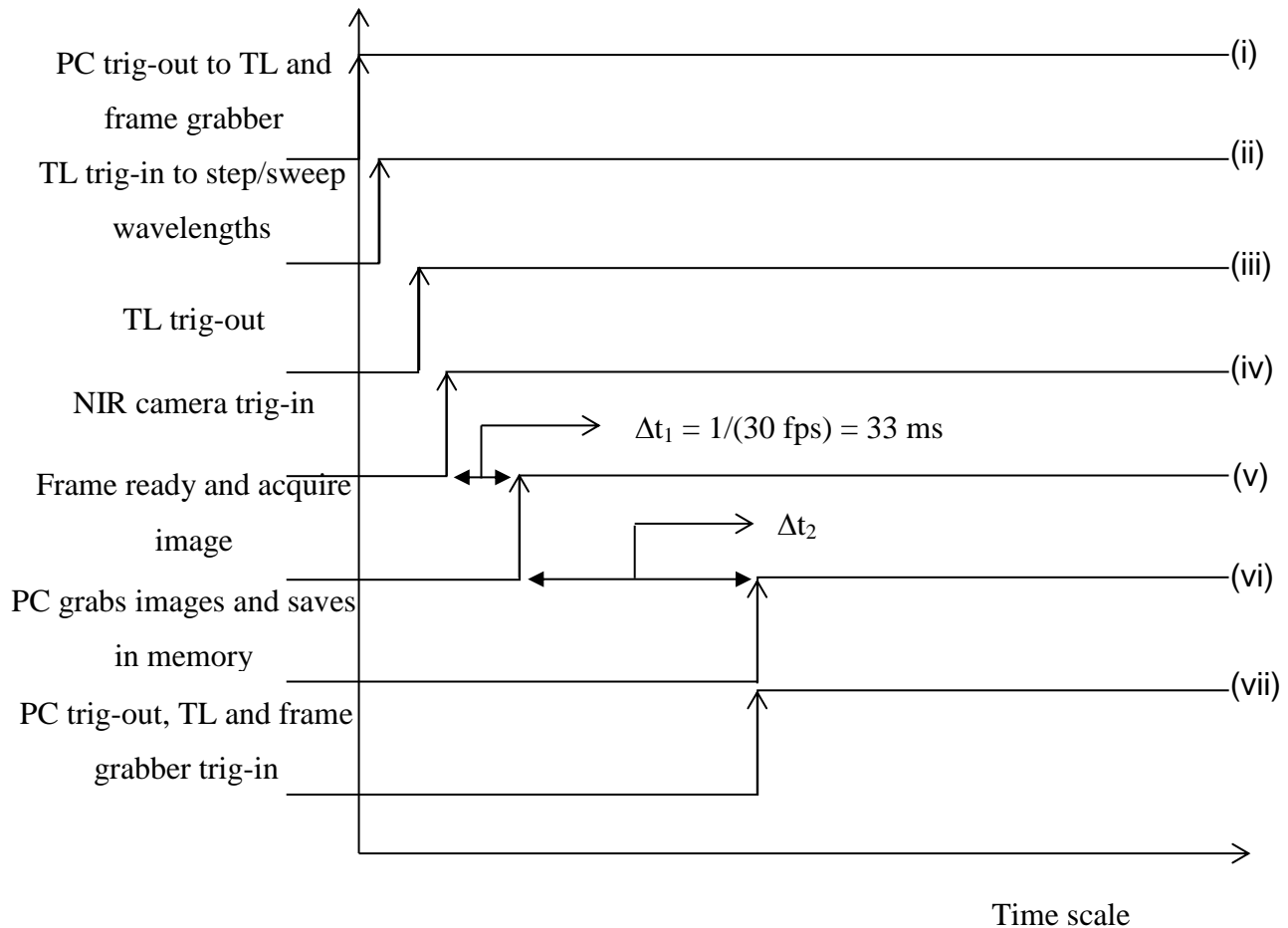
Figure 3. 4 The timing/synchronization diagram

The diagram in Fig. 3.4 shows the synchronisation. The different steps for synchronised operation are given below.

i. Tell tunable laser and the frame grabber to be prepared for lasing and acquisition respectively.

ii. Tell laser to change frequency /wavelength.

iii. The laser was triggered out.

iv. The camera was triggered in.

v. Laser sent an analogue triggering signal to the NIR camera to acquire an imageand the image was acquired (takes the time Δt_1).

vi. When acquisition was over, camera transferred image through camera link cable and it was saved in memory within the time Δt_2

vii. Repeat sequence i-vi.

3.3   WSI – a lens-less setup

A preliminary version of WSI was developed just to check the performance of the tunable laser and high resolution camera. This experiment demonstrated a simple approach of depth resolved imaging of a pair of specularly reflecting transparent surfaces with single illumination. As a result, a sharp peak was obtained with frequency-domain tuning, which proved the linear relationship of phase with the wavenumber.
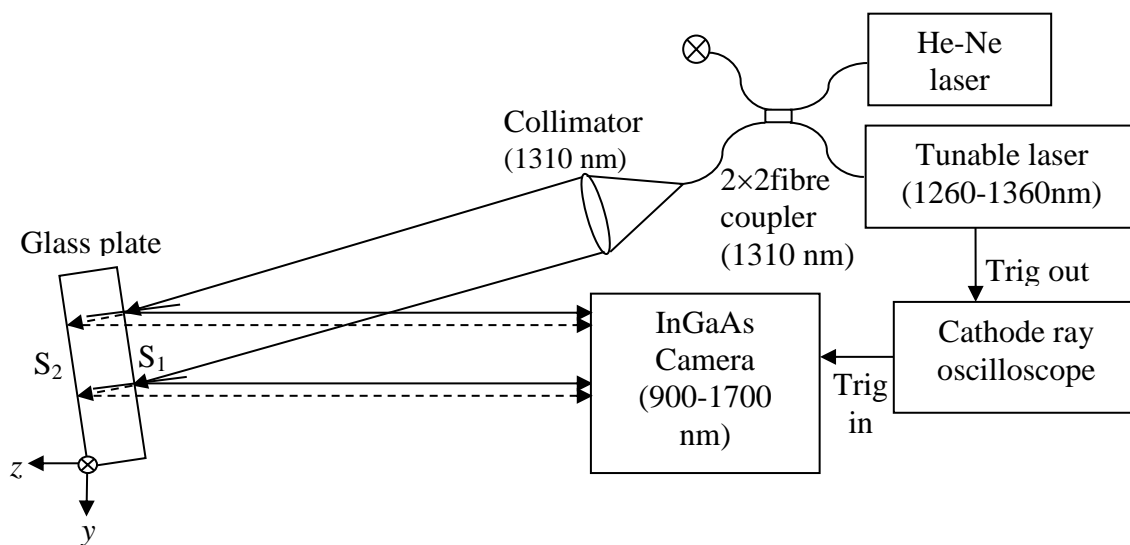
Figure 3.5 Depth resolved imaging by WSI

The WSI had been developed with a sample of depth $z=6$ mm plate made by BK7 glass of refractive index $n_1=1.51$ which provided excellent transmittance through-out the near infrared spectra. S_1 and S_2 was a pair of specularly reflecting transparent surfaces of the glass plate with the optical thickness $n_1 z$. In this experimental setup the sample was illuminated by a single illuminating beam, resulting in a single sensitivity.

The light source consists of an external cavity tunable laser (TSL-510, Santec Ltd. (50mW, central wavelength λ_c = 1310nm and bandwidth $\Delta\lambda$ = 100nm)) whose frequency was varied approximately linearly in time by setting the laser in a sweep mode. The start and final frequencies of the sweep and the step between two consecutive frequencies could be adjusted in the tunable laser. The laser was set at one-way sweeping mode (single ramp) with step operation where the frequency interval was set at 0.002THz, a dwell time of 0.1 sec and a tuning rate of 0.1 nm/sec. The laser output was coupled with He-Ne laser used for alignment purposes (30mW, wavelength = 632.8nm), with a 2×2 fibre optic coupler (Thorlabs, central wavelength= 1310nm, SMF single mode fibres) to get proper alignment. The broadband coupler was polarization independent, passive and designed for the 1240-1380nm range. One of the outputs of the coupler served as a source is the illumination beam of the interferometer which was collimated by 1310nm compatible FC/APC collimator lens. This fibre collimation package was pre-aligned to collimate a laser beam propagating from the tip of an FC/APC connected fibre with diffraction limited performance at the design wavelength. In addition, the doublet lens had an anti-reflection (AR) coating to minimize surface reflections.
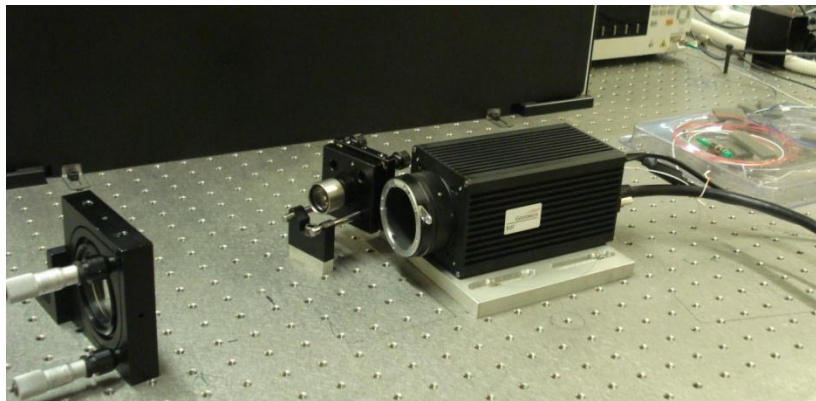
Figure 3.6 Lens-less setup used to validate a WSI single channel system based on a telecom tunable laser and an InGaAs NIR camera.

A pair of smooth wavefronts reflected at the front and back surfaces of the glass plate (S_1 and S_2), interfered with each other and straight line fringes were seen through the NIR camera (which did not have an imaging lens). The camera was triggered by the laser via a BNC-BNC cable. The triggering operation was inspected by means of a cathode ray oscilloscope (CRO) to check whether all frames were recorded sequentially whilst the wavelength of the laser was tuned at a constant rate.

3.4 Evaluation of system performance (linearity of frequency scan)

3.4.1 Full frequency scan

Consider the layout shown schematically in Fig. 3.5. A beam of wavelength λ is partially reflected from both the glass-air interface S_1 (front surface) that acted also as a reference surface and the back surface S_2. The incident angle was kept as small as ~ 22° (geometrically measured), so that the thickness within the material along the incident beam and along the reflected beam normal to the sample surface (in the direction of z axis) were considered to be the same. This was exaggerated in Fig. 3.5 for illustration. $\Lambda(x, y) = 2n_1 z(x, y)$ is the optical path difference between the front and back surfaces of the sample. In the Cartesian coordinate system shown in Fig. 3.5, it corresponds to $(2 \times 1.51 \times 6)$mm=18.12mm. S_1 and S_2 are parallel surfaces, so $\Lambda(x, y)$ remains constant throughout the sample. The reflected wavefronts imaged onto a pixel of the photo-detector array with indices (m, n). The phase difference, depth range and resolution can be evaluated by using equations 3.5, 3.11 and 3.13 respectively.

A great feature of the TSL-510 laser is that it can be tuned linearly in frequency (rather than in wavelength as it is the case of laser diodes). The results presented here correspond to a full frequency scan at constant rate, starting from $v_1 = 237.9305\,\text{THz}$ to $v_2 = 220.4356\,\text{THz}$, that correspond to wavelengths $\lambda_1 = 1260.00$nm and $\lambda_2 = 1360.00$nm, respectively. The frequency sweep was done in 'step mode' and the step between two consecutive frequencies was fixed at 0.002THz, corresponding to the wavelength step 0.011nm. A sequence of 8748 interferograms of 4×4 pixels were recorded with the camera running at 30 frames s^{-1}. Only a small number of pixels were used to increase speed and reduce data storage. The output power of the laser beam was set at 0.02mW.

Figure 3.7(a) shows the intensity with respect to frame number for the full frequency scan, measured for one pixel (2,2) in the field of view, while Fig. 3.7(b) shows the same intensity pattern in a narrow range. Figure 3.8(a) shows the Fourier transformed data against the distance axis and Fig. 3.8(b) represents the peak of interest in detail, on the same axis.

The depth resolution was measured by the width of the peak in the 1-D Fourier domain, which was ~ 50µm from the 3.8(b) and ~ 46µm from Eqn. (3.13). Note the execellent uniformity in the signal modulation throughout the scan.
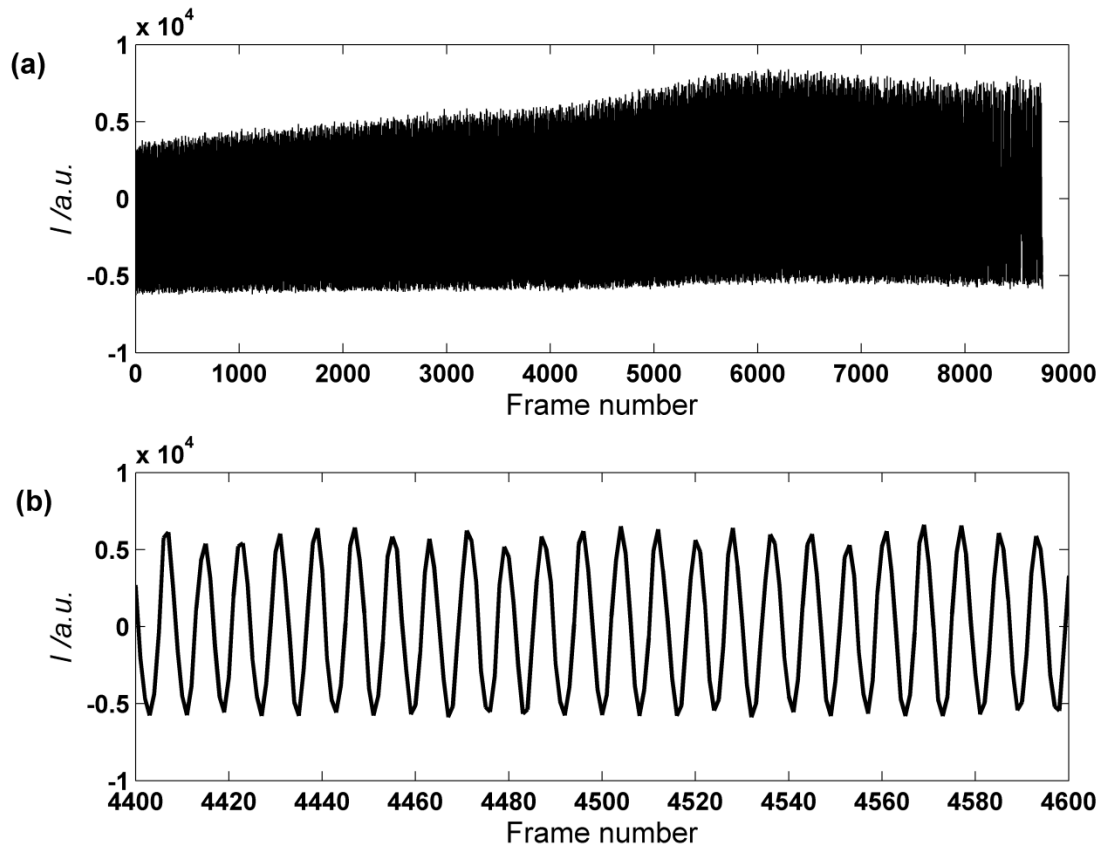
Figure 3. 7 (a) Intensity signal recorded at a pixel of an InGaAs detector array during a full frequency scan of a NIR tunable laser. The intensity corresponds to the interference between light reflected at the front and back surfaces of a BK7 glass plate.(b) Same signal in a smaller range.
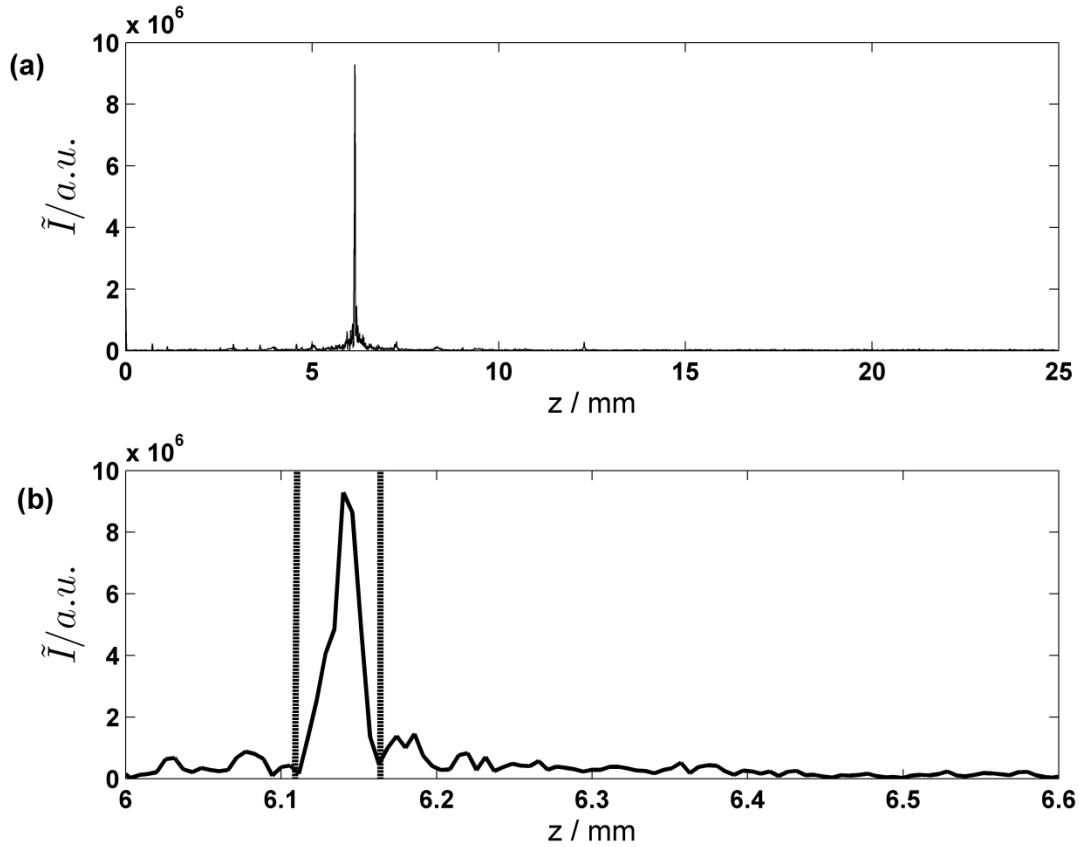
Figure 3. 8 (a) Fourier transform of the signal shows in Fig. 3.8(a) showing the cross correlation peak along distance axis, (b) zoomed-in version of the peak of interest.

3.5 Conclusion

In this chapter a mathematical description of WSI was presented for a single channel system. A prototype WSI system based on a telecom NIR laser and a NIR InGaAs camera was proposed and its performance was validated in terms of scan linearity. A narrow peak was obtained from a full frequency scan of the laser, representing the back surface of the plate. The peak had a width of ~0.05mm (z-axis), which compared well with the expected value of 0.046mm from Eqn. (3.13).

In this preliminary experiment with single illumination having single sensitivity, only the positions of the scatterers on the back surface of the plate could be located or the whole depth could be calculated from the intensity signal recorded at a single pixel during a full

frequency scan. Moreover, if two scans are performed before and after a deformation of the sample, the phase change $\Delta\phi_j$ (m, n, 0) would be evaluated at the peak, which is a direct measure of the change in optical path length $\Delta\Lambda_j(m, n)$ due to the deformation only one component of the 3-D displacement could be measured. In the next chapter a full-field WSI system is discussed where multiple illumination directions are used to get three orthogonal components of displacement fields of a deformed object using the same basic principles of this Chapter. The system described in this Chapter can thus be used as a building block for the full sensitivity system presented in Chapter 4.

Chapter 4

4 Full sensitivity WSI system

4.1 Introduction

A full sensitivity WSI has been designed and constructed with the aim of measuring displacements in the full volume of a scattering material. All the components of the displacement vector can be calculated at each voxel of the data volume by simultaneously measuring the interference signal produced for different illuminations during a full frequency scan. In the proposed design, the sample was illuminated by three collimated coherent beams which were 120° apart around the observation direction, their optical paths adjusted relative to the reference beam so that it was possible to resolve three reconstructions in the frequency domain. This was a form of sensitivity multiplexing which involves assigning non-overlapping frequency ranges to different signals or to each illuminating beam in the set-up. Direct measure of the change in optical path length $\Delta\Lambda_j(m,n)$ due to the deformation, can

measure only one component of the displacement fields. In the next Chapter a full field WSI system is discussed where multiple illumination directions are used to get three orthogonal components of the displacement fields of a deformed object using the same basic principles of this Chapter. The system described in this Chapter can thus be used as a building block of the full sensitivity system.

The following sections describe the optical setup, principle of WSI based on frequency multiplexing and the main mathematical framework. Advantages over the corresponding method based on low-coherence interferometry (LCI) include a non-dependency on spatial scanning devices in the interferometer model and increased signal to noise ratio.

4.2   Optical setup

Fig. 4.1 shows a schematic diagram of the optical setup of WSI, including a reference arm, three illumination beams 120° apart from each other around the observation direction and the imaging arm. The output of the tunable laser (TSL-510) was connected to one of the inputs of 2×4 PLC (planar lightwave circuit) fibre optic splitter (Shenzhen Gigalight). The splitter contains single mode fibres (SMF) designed for a central wavelength of 1310 nm. One of the outputs of the splitter served as a source of the reference arm, OF_R, and the other three served as sources to the three individual illuminating beams, OF_1, OF_2 and OF_3. Reference and sample (scattered back from sample) beams were combined with a 45:55 pellicle beam splitter, PBS, and the interference pattern was detected by a 2-D photo-detector array (SU640SDV-1.7RT/RS170, Goodrich corporation, 640×512 pixels, 14 bit resolution).
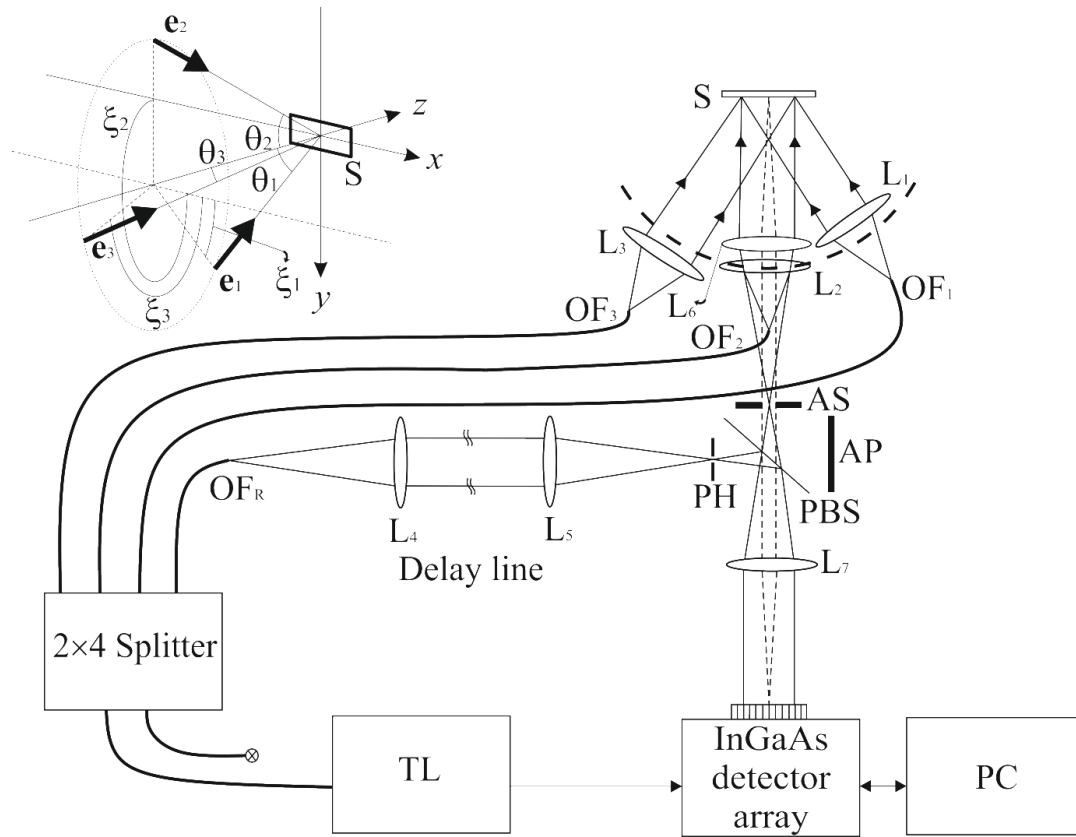
Figure 4.1 WSI set-up showing the tunable laser (TL), 2×4 PLC splitter, InGaAs detector, pellicle beamsplitter (PBS), absorber plate (AP), pinhole (PH), aperture stop (AS), sample (S), lenses (L_1-L_7), optical fibres (OF_1, OF_2, OF_3, OF_R) and personal computer (PC).

The three illuminating beams were collimated by near-infrared double achromats L_1, L_2 and L_3 and their orientation was such that the sample S was illuminated from three non-co-planar directions. The beams subtended zenith angles θ_1, θ_2 and θ_3 with the observation vector along the negative direction of z-axis. The imaging arm was formed by lenses L_6 and L_7. The illumination beams were symmetrically oriented around the observation direction and making azimuth angles ξ_1, ξ_2 and ξ_3 with the positive direction of x-axis as shown in the insert in Fig. 4.1. A $4f'$ double telecentric imaging system was formed by the lenses L_6 and L_7 in the imaging arm. An aperture stop, AS, was placed at the mid-focal plane of both lenses to control telecentricity, speckle size and throughput of the system. In the reference beam, a pinhole, PH was used to control the intensity ratio between reference and object beams.

The optical path difference between the reference beam and each illumination beam was adjusted with respect to a delay line by moving the respective collimating lenses (L_1 or L_2 or L_3) slightly either towards or away from the sample. If a sphere is considered with a centre at

the intersection point of the sample surface and the optical axis of the whole system, then the optical centre of achromat L_1 lied inside the sphere, of L_2 on the sphere surface and of L_3 outside it. The optical fibres OF_1, OF_2 and OF_3 contained the same optical paths and thus the distances from the illuminating lenses to the sphere measured their relative optical path differences, which were used to separate signals corresponding to different sensitivity directions in the frequency domain. The setup described above was effectively a two-splitter Mach-Zehnder interferometer with multiple illumination directions which were frequency multiplexed- see Fig. 4.2.
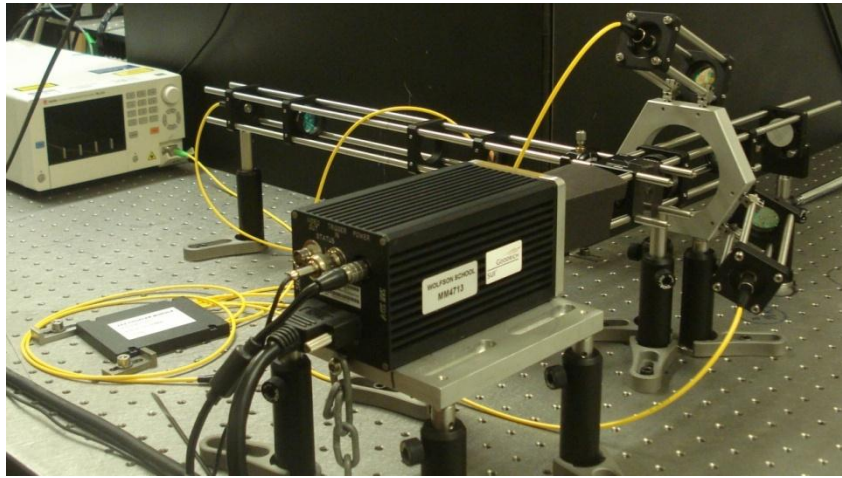
Figure 4.2 The laboratory set-up of WSI

The first step of the WSI design was setting up the illumination system. The sample was illuminated by three collimated coherent beams which were 120° apart. Three images of a sample due to three illumination beams could be resolved easily in the frequency domain by adjusting the optical path difference between each illumination and reference beam. This was done simply by sliding the lens along with the mounting cage slightly for each beam towards or away from the object. Light was launched from the tunable laser through the FC/APC connector and was fed into a single mode optical fibre (SMF-28e) of working wavelength 1310nm, which was one of the inputs of PLC splitter. The power of the input beam was equally divided into four outputs through the splitter and among them three served as sources of three illumination beams of the interferometer.

Each illuminating beam of the interferometer as shown in Fig. 4.3 and Fig. 4.4 consisted of four components:

1. Output fibre of PLC splitter (SMF-28e fibre) as a source,

2. FC/PC fibre adapter,

3. Achromatic doublet lens of 100mm focal length and

4. Four micro bench rods (4 inch each) for holding all other three components together.

4.3 Illumination beams
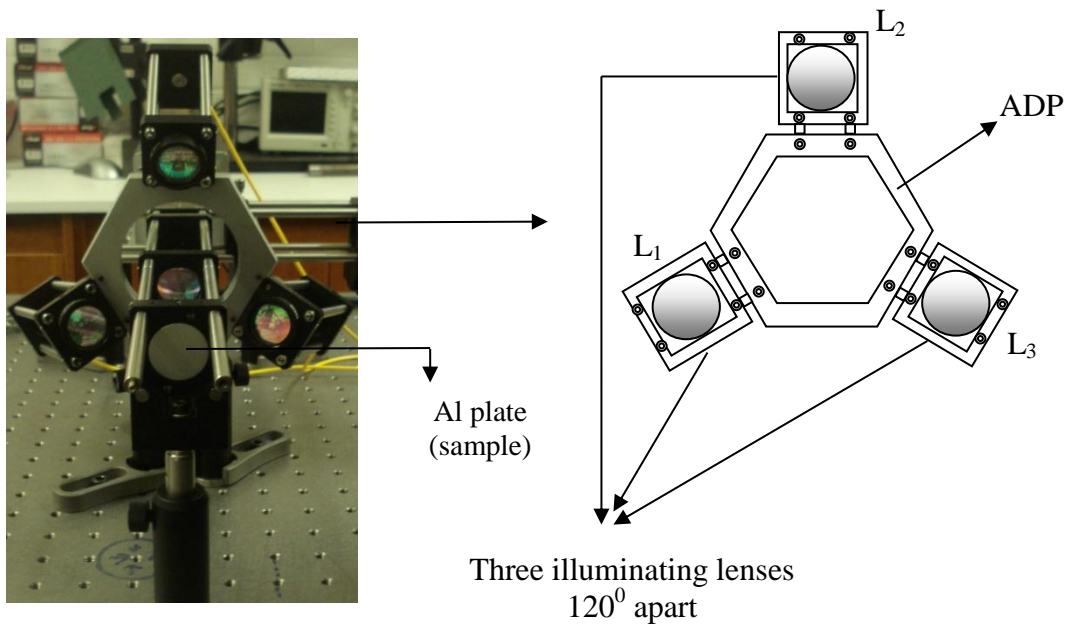
Figure 4.3 Illumination system; Top: viewing towards the camera; ADP- adapter for three illumination beams, Al plate –Aluminium plate.
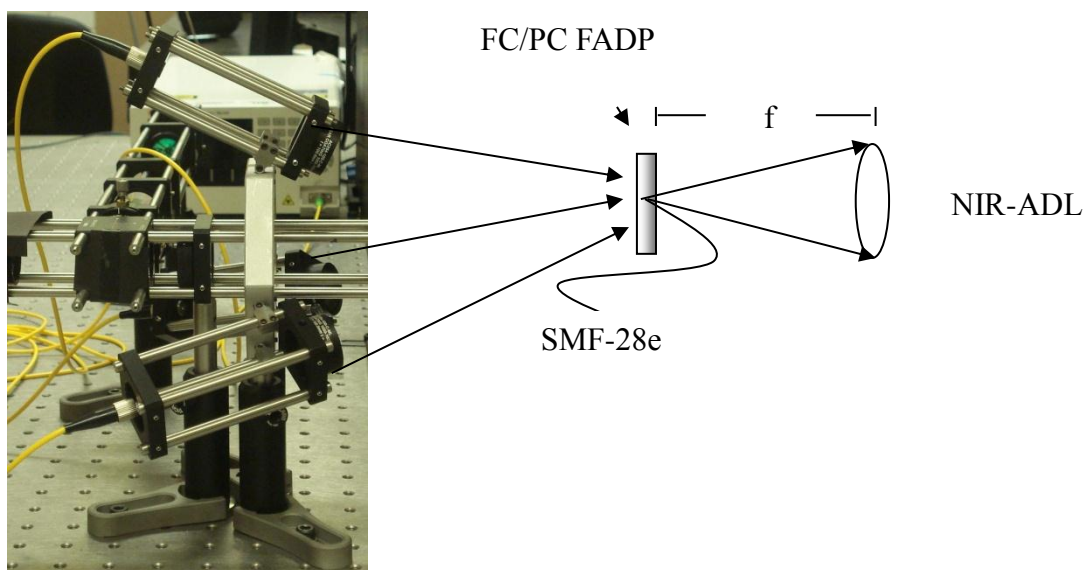
Figure 4. 4 Illumination beams; side view: camera is on the left hand side, object on the right; NIR-ADL- near infrared achromatic doublet lens, f- focal length, FADP- fibre adapter

4.3.1 Collimation of individual illumination beam

The working wavelength (1260-1360nm) of the proposed WSI was in the infrared region, an infrared (IR) viewing card (61.87mm $\times$ 45.5mm, 700-1400nm wavelength range) was used to collimate each invisible illumination beam.
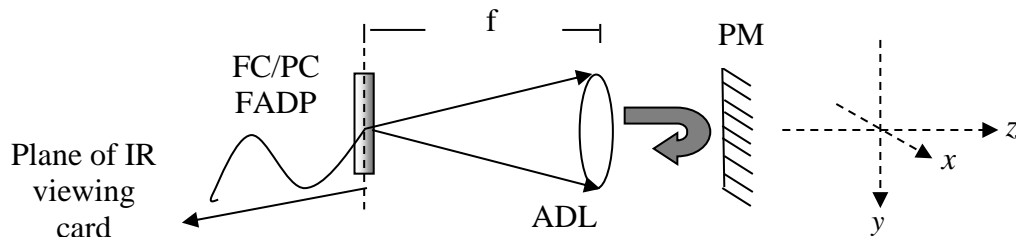
Figure 4.5 Collimation of a beam; ADL- achromatic doublet lens, PM-Plane mirror, f-focal length, FADP- fibre adapter

In each illumination system, the single mode fibre was connected to the adapter through FC/PC connector and placed at the back focal point of the achromatic lens for getting proper collimation on the other side (right hand side of the lens) as shown in Fig. 4.5. During the collimation procedure, a plane mirror was placed at the other side and tilted slightly along the *z*-axis. If the outgoing beam was parallel, it reflected back from the mirror and passed through the lens again, converged on the back focal plane of the lens at a point slightly away from the central point due to the mirror tilt. The IR card should be kept at the same plane of the fibre adapter to visualize that bright focussed spot. This spot would become blurred and bigger for any other position of the lens. Thus the best collimation was achieved by focussing the spot back into the fibre and detecting at the other side of the fibre splitter. After getting the collimated beam, the mirror was removed and subsequently the output beam diameters (at the right hand side of the lens) were observed at several positions along the same line away from the lens using that IR card. If the beam diameter was found to be the same at various distances, then it was safe to assume that output beam was collimated and the fibre tip was at the back focal plane of the lens.

4.3.2 Configuring three non-coplanar collimated beams

The next step was to fix three collimated illumination beams along with their mounting cage, fibre adapter and four rods as shown in Fig. 4.4. They should be non-coplanar and were 120° apart from each other. A special adapter was made for holding three beams as shown in Fig. 4.3. Swivel couplers connected the cage assemblies to the adapter and enabled positioning them at zenith angles θ_1, θ_2 and θ_3 with the observation direction along the negative z-axis as shown in the insert of Fig. 4.1. The adapter was made from aluminium, adhered to close tolerances and provided rigid structure. The sample was then illuminated by three beams simultaneously, as shown in Fig. 4.1 and they were oriented in such a manner that three collimated spots on the sample surface overlapped with each other.

4.3.3 Imaging optics

The imaging optics in the sample arm of the interferometer is shown in Fig. 4.6. The sample was imaged by two achromatic doublets L_6 and L_7 of focal length 100 mm each, in a 4f configuration. A 1 inch (Ø1") diameter, sand blasted, flat aluminium plate was used as a reference surface or sample.

At first, the doublet L_7 was placed at a distance of 100mm away from 2-D photo-detector array. The cemented IR achromatic doublet of 100mm focal length was available in pre-mounted condition which was SM-1 threaded and the mount made itself easy to handle the lens and incorporate it into micro bench setup. All achromatic doublets used here are designed to work in the 1050-1620nm IR spectral region. They are useful for controlling chromatic aberrations at 1330nm and are frequently used to achieve a diffraction-limited spot when using a monochromatic source like a laser.

A ring activated iris diaphragm was placed at a distance of 100mm away from the lens L_7 and a pellicle beamsplitter (45:55 ratio, 1-2μm wavelength range) was inserted in between them as shown in the figure above. This ring activated iris controlled telecentricity, speckle size and throughput. The cube-mounted pellicle beamsplitter virtually eliminates ghosting and minimizes dispersions since the second surface reflection is superimposed on the first one. They are extremely fragile due to their 2μm thick nitrocellulose membrane. Another doublet L_6 was then kept around 100mm away from the diaphragm and finally the sample was held at the back focal plane of L_6. A clear image of the sample with 1:1 magnification was obtained

with this design, so that in the future a human cornea could be imaged in the full detector array.
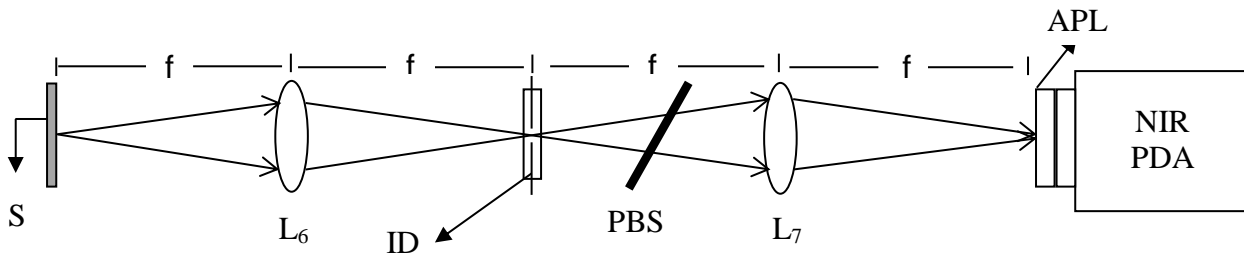
Figure 4.6 Imaging optics; ID- iris diaphragm, APL-adapter plate, PBS- pellicle beam splitter, S-sample

As mentioned before the sample arm was designed like a classical 4-f imaging setup, which is widely used in optical interconnects because of its telecentricity and good imaging capabilities for extended fields.
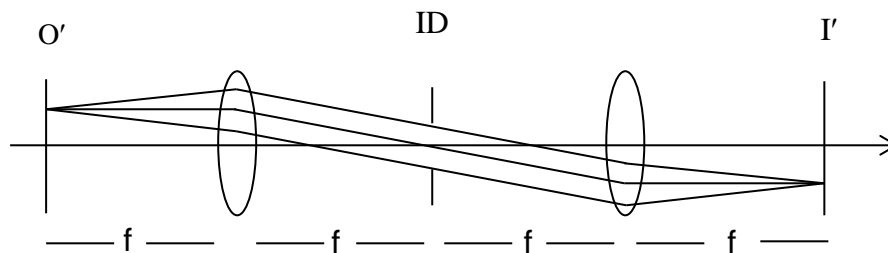
Figure 4.7 Double telecentricity; O'- object, I'- image, f-focal length, ID- iris diaphragm

Telecentricity is an important feature for several optical metrology systems as the apparent size of an inspected object does not change with focus, object position or object thickness. The iris diaphragm is strategically located at the focal point of the front and rear lens elements in the sample arm and it is basically controlling the amount of light that reaches the charge-coupled device (CCD) array. Telecentricity is an important property for designing multi-element lenses where the chief rays are collimated and parallel to the optical axis in the image and/or object space. In a telecentric system the magnification remains constant and that is irrespective of image and/or object location. The telecentricity can be classified in three different categories depending upon the optical space(s) in which the chief rays exhibit their

56

behaviour. The telecentricy achieved in the sample arm of the proposed WSI setup in Fig. 4.1, was the bilateral or double telecentricity. In this proposed system the stop was placed at the common focal plane of lenses L_6 and L_7, resulting in both the entrance and exit pupils being located at infinity.

4.3.4 Alignment of the reference arm

One of the outputs of the PLC fibre splitter was connected to the externally SM1 threaded fibre adapter at one end of the reference arm through an FC/PC connector and served as the source of reference beam. The diverging beam was then collimated by achromatic doublet L_4 of 100 mm focal length. If a fibre tip or the source of diverging light was placed at back focal plane of lens L_4, then collimated light could come from other. The collimation was done according to section 4.3.1.

The second doublet L_5 had (focal length 100mm) was placed on an XY translation stage at a distance of~230mm from L_4. The XY translator provides ±1 mm of travel perpendicular to the optical axis of a cage system. The movable carriage is threaded with SM1 threads and directly accepts Ø1" optics up to 0.3" (8 mm) thick.

A 5μm diameter pinhole was placed on a Z translation stage at a distance 100 mm away from L_5 as shown in the the Fig. 4.9. The SM1 threaded translation stage provides a stable, highly repeatable 1.5 mm translation of optics within a 30 mm cage system with an actuator knob graduated in 1 μm increments. The precision pinhole on the Z translation stage in conjunction with precision alignment (L_5 on XY translation stage), was effectively stripping variations in intensity of a Gaussian beam and a bright reference spot could be seen through the imaging device by adjusting the distance between them.

The diverging reference beam at the other side of the pinhole was recombined with the object beam at the 45:55 pellicle beam splitter, which gave rise to a high modulation speckle interference pattern on the detector array. The intensity ratio between object and reference beam was adjusted by moving the pinhole along the delay line.
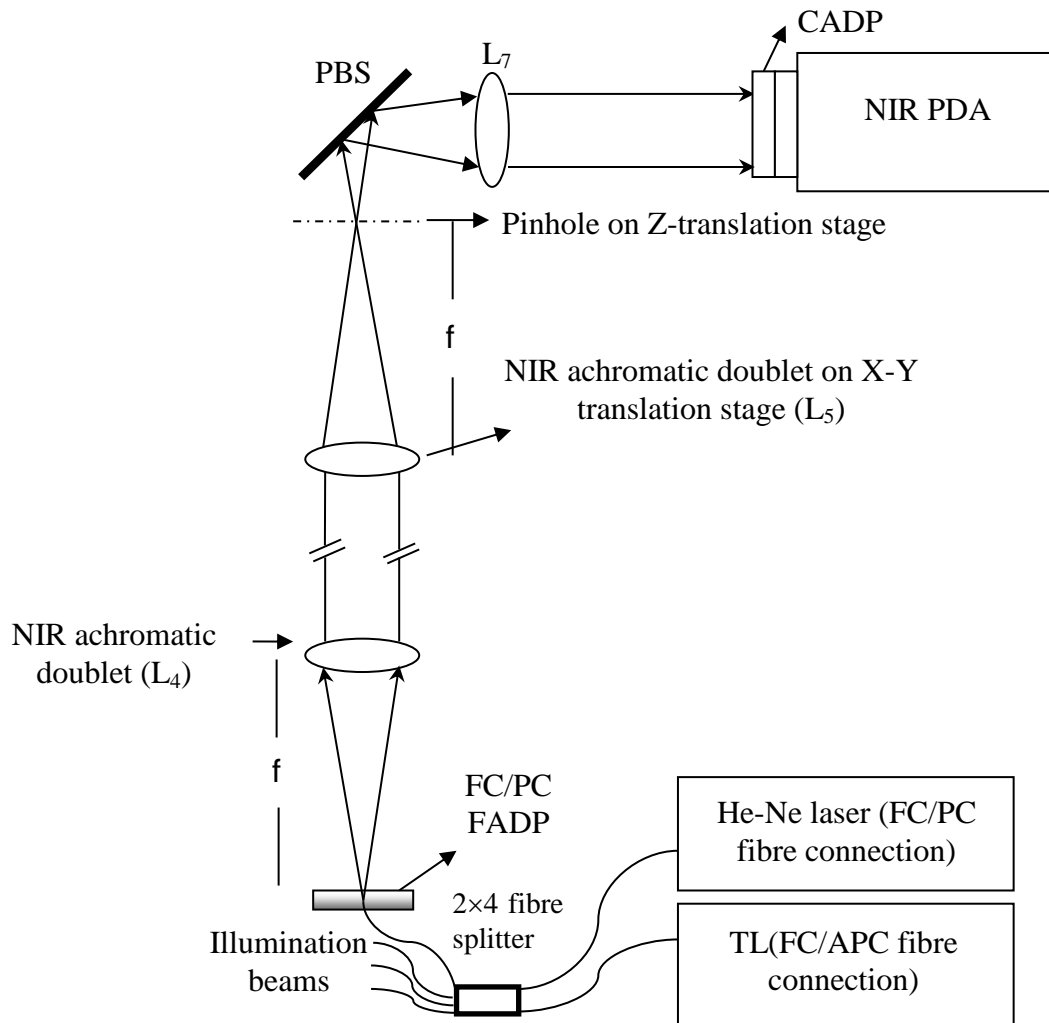
Figure 4.8 Alignment of reference beam; PBS- pellicle beam splitter, CADP- camera adapter plate, TL- tunable laser, FADP- fibre adapter.
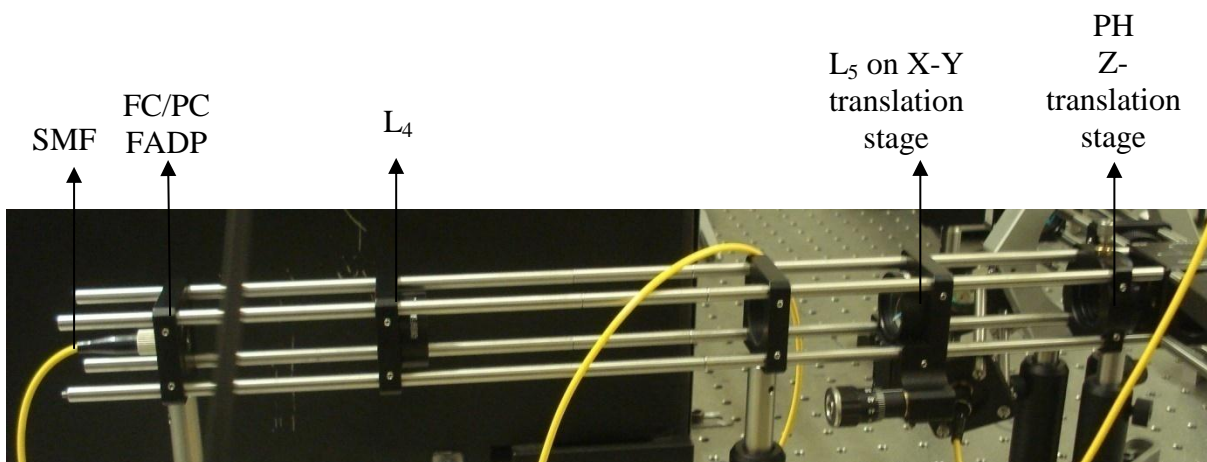
Figure 4.9 Reference beam (Lab setup); SMF- single mode fibre, FADP- fibre adapter, PH-pinhole.

4.4 Working principle of full-sensitivity phase-contrast Wavelength scanning interferometry

Let us consider a plate made of a semitransparent scattering material that was illuminated and observed using the interferometer shown in Fig. 4.1. The observation direction was defined as the negative direction of the z-axis. The scattering surface was imaged onto the photo-detector array with magnification $M=1$ as already discussed in section 4.3.3.
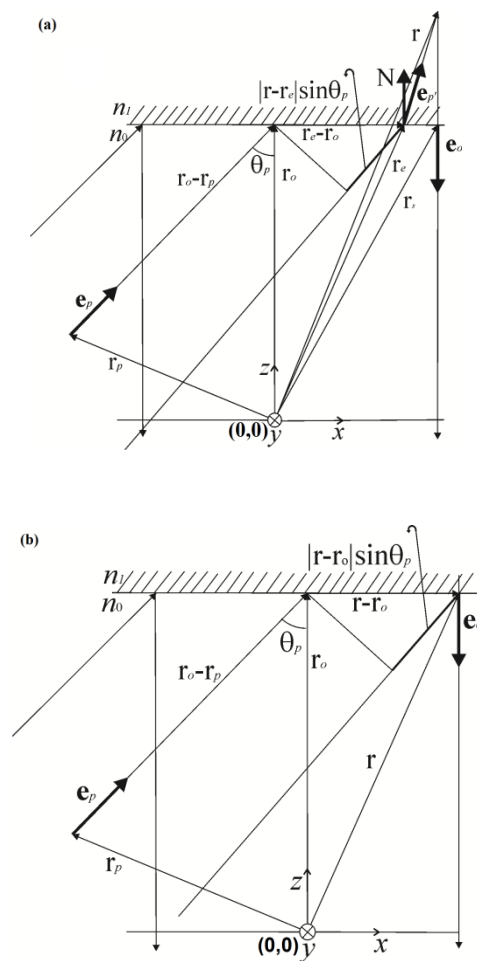
Figure 4.10 Generalized optical path diagram for WSI with multiple illumination directions for a scattering material (a) and an opaque surface (b).

Let us consider Fig. 4.10. A detailed ray and wavefront diagram is shown for one illumination beam on the plane of incidence in Fig. 4.10(a) for a scattering material and in Fig. 4.10(b) for an opaque surface. All the position vectors are drawn from the reference point (0,0) on the plane xy at $z=0$ which is considered the reference plane. $\mathbf{e}_p$, $\mathbf{e}_{p'}$ and

$\mathbf{e}_o=(0,0,-1)$ are unit vectors along the *p*-th illumination beam in the surrounding medium, the illumination beam within the material, and the observation direction, respectively. $\mathbf{r}$ is a position vector of a point with coordinates (*x, y, z*) within the scattering material which is imaged onto a pixel with indices (*m, n*) on the photo-detector array. p_x and p_y are the pitch between pixels along the *n* and *m* axes respectively on the photo-detector array so that $x=np_x$ and $y=mp_y$. $\mathbf{r}_0$ is the position vector of a point on the sample surface having coordinates (x_0, y_0, z_0) at which the illumination beam is incident and the point is imaged at pixel (0, 0) of the detector. Similarly; $\mathbf{r}_e$, $\mathbf{r}_s$ and $\mathbf{r}_p$ are respectively the position vectors of points with coordinates (x_e, y_e, z_e), (x_s, y_s, z_s) and (x_p, y_p, z_p). At (x_e, y_e, z_e), the incident light is refracted at the sample surface for reaching the point $\mathbf{r}$ within it, the point (x_s, y_s, z_s) on the surface of a scattering material is imaged onto pixel (*m, n*) and finally (x_p, y_p, z_p) is a point on the angled illumination wavefront propagating with direction $\mathbf{e}_p$ incident on the object plane at $\mathbf{r}_0$. n_1 and n_0 are the refractive indices of the material and surrounding medium (air in this case) respectively.

The optical path difference between light from the *p*-th illumination beam scattered at point (*x, y, z*) within the material and the reference wave can be written as

$$\Lambda_p(x,y,z) = n_0[\mathbf{e}_p \cdot (\mathbf{r}_0 - \mathbf{r}_p) + \mathbf{e}_p \cdot (\mathbf{r}_e - \mathbf{r}_0)] + n_1[\mathbf{e}_{p'} \cdot (\mathbf{r} - \mathbf{r}_e) + \mathbf{e}_o \cdot (\mathbf{r}_s - \mathbf{r})] + n_0 \mathbf{e}_o \cdot \mathbf{r}_s \quad (4.1)$$

The triangle with r_e-r_0 as the hypotenuse is a right triangle, and all incoming vectors are parallel. The first term on the right-hand side of Eqn. (4.1) represents the optical path from a point on the illumination wavefront, $\mathbf{r}_p$, to point $\mathbf{r}_e$, where light enters the material. The second term represents the optical path due to propagation within the material upon refraction, from point $\mathbf{r}_e$ to $\mathbf{r}$ and back to the surface at $\mathbf{r}_s$. Finally, the last term represents the optical path from the object surface at $\mathbf{r}_s$ to the reference beam's zero delay wavefront at $z= 0$. The relationship between $\mathbf{r}_s$ and $\mathbf{r}_e$ in a general case is governed by refraction at $\mathbf{r}_e$ by

$$|\mathbf{r}_s - \mathbf{r}_e| = |\mathbf{r} - \mathbf{r}_s| \tan(\theta_{p'}) \qquad (4.2)$$

and the Snell's law in vector form:

$$n_0(\mathbf{N} \times \mathbf{e}_p) = n_1(\mathbf{N} \times \mathbf{e}_{p'}) \qquad (4.3)$$

where θ_p and $\theta_{p'}$ are the incidence and refracted angles of the p-th beam, $\mathbf{N}$ is a unit vector normal to the surface, $(0, 0, 1)$ here, and $\mathbf{e}_{p'}$ is a unit vector pointing along the refracted beam. This vector representation is convenient when dealing with non-coplanar illumination and observation directions, especially at the data processing stage. In the following analysis, we will consider the case of a flat sample that lies perpendicular to the observation direction to eliminate extra terms that would appear due to refraction at the surface. The general case is described in section 2.3.1.4 in [79].

Let us consider the object is modelled as a set of N_s discrete thin scattering layers parallel to its surface. The intensity due to the interference of the three object wavefronts and the reference wavefront can be written as

$$I(m,n,t) = |\, A_0(m,n,t) + \sum_{p=1}^{3}\sum_{j=1}^{N_s} A_{pj}(m,n,t)\exp[i\phi_{pj}(m,n,t)]\,|^2 \tag{4.4}$$

This is the modified form of the Eqn. (3.1) in Chapter 3. In Eqn. (4.4), A_0 represents the amplitude of the reference wavefront. A_{pj} ($p=1, 2, 3$; $j=1, 2, \ldots N_s$) is the amplitude of the wavefront scattered at the j-th slice when illuminated by the p-th beam and $i=\sqrt{-1}$. ϕ_{pj} is the phase difference between light scattered back at the j-th slice when illuminated by the p-th beam and the reference beam. The spatial indices m and n take the values $m=0, 1, 2, \ldots, N_m-1$; $n=0, 1, 2, \ldots, N_n-1$ and t is a non-dimensional time defined as the true time divided by the camera interframe time. Expanding Eqn. (4) and dropping the (m, n, t) dependence in all the amplitude and phase variables for clarity gives

$$I(m,n,t) = A_0^2 + \sum_{p=1}^{3}\sum_{j=1}^{N_s} A_{pj}^2 + 2\sum_{p=1}^{2}\sum_{q=p+1}^{3}\sum_{j=1}^{N_s-1}\sum_{l=j+1}^{N_s} A_{pj}A_{ql}\cos(\phi_{pj}-\phi_{ql}) + 2A_0\sum_{p=1}^{3}\sum_{j=1}^{N_s} A_{pj}\cos\phi_{pj} \tag{4.5}$$

The right hand side of Eqn. (4.5) consists of four terms. The first two correspond to dc terms. Term 3 represents interference between light from the j-th and light from the l-th layers corresponding to different illumination beams indicated by indexes p and q, and together with Term 2 are referred to as the autocorrelation terms (AC). Term 4 represents the interference between the scattered light from the j-th slice when illuminated by the p-th beam and the reference beam, and is referred to as the cross correlation term (CC). This latter term contains the information about the microstructure of the sample.

The phase ϕ_{pj} changes with time according to

$$\phi_{pj}(m,n,t) = \phi_{sj}(m,n) + k(t)\Lambda_{pj}(m,n) \, , \tag{4.6}$$

Where $k(t)$ is the wavenumber $2\pi/\lambda(t)$, and ϕ_{sj} is a phase shift that may arise at zero nominal path difference due to, for instance, a phase change on reflection or due to the microscopically random arrangements of scatterers contributing to the amplitude at pixel (m, n) at the j-th slice, i.e. the phase that leads to speckle noise. Λ_{pj} represents the optical path difference given in Eqn. (4.1) due to the p-th beam and for the j-th slice, which lies at a depth $z = z_0 + (j-\frac{1}{2})\delta z$ below the sample's surface, δz being the layer thickness. WSI involves changing k with time over a total range Δk while an image sequence is recorded. In the ideal case of a linear variation of k with t,

$$k(t) = k_c + \delta k t \tag{4.7}$$

where k_c is the central wavenumber, δk is the interframe wavenumber increment and t ranges from $-\Delta k/2\delta k$ to $+\Delta k/2\delta k$, corresponding to the central wavelength λ_c, with a total number of N_t intervals. Substitution of Eqn. (4.7) into Eqn. (4.6) leads to

$$\phi_{pj}(m,n,t) = \phi_{sj}(m,n) + k_c\Lambda_{pj}(m,n) + \delta k\Lambda_{pj}(m,n)t \, , \tag{4.8}$$

The linear variation of ϕ_{pj} with t leads to temporal frequencies (units of "cycles per frame")

$$f_{\Lambda pj}(m,n) = \delta k\Lambda_{pj}(m,n)/2\pi \, , \tag{4.9}$$

that is, frequencies proportional to the optical path difference between light from the p-th beam scattered at the j-th layer and the reference wavefront. It is convenient to define an alternative frequency in units of "cycles per scan duration"

$$\hat{f}_{\Lambda pj}(m,n) = f_{\Lambda pj}N_t = \Delta k\Lambda_{pj}(m,n)/2\pi \, , \tag{4.10}$$

Thus, measuring frequencies $f_{\Lambda pj}$ or $\hat{f}_{\Lambda pj}$ in a pixel wise basis provides a measure of $\Lambda_{pj}(m, n)$, which can be used to locate the coordinates of scatterers on the surface and the bulk of the sample. Moreover, if two scans are performed before and after a deformation of the sample, then provided ϕ_{sj} remains the same between scans, the phase changes $\Delta\phi_{pj}(m, n, 0)$ provide a direct measure of the change in optical path lengths $\Delta\Lambda_{pj}(m, n)$ due to the deformation. Both the position and phase change of surface scatterers can be evaluated by a time-frequency analysis. The Fourier transform of the interference intensity signal $I(m, n, t)$ in Eqn. (4.5) which is the modified version of Eqn. (3.8) of Chapter 3 for three illumination beams, can be written as

$$\tilde{I}(\hat{f}) = \tilde{W}(\hat{f}) * \left\{ \begin{array}{l} \left(I_0 + \sum_{p=1}^{3}\sum_{j=1}^{N_s} I_{pj} \right)\delta(\hat{f}) + \sum_{p=1}^{3}\sum_{j=1}^{N_s}\sqrt{I_0 I_{pj}}\,\exp(\pm i\phi_{0pj})\delta(\hat{f} \mp \hat{f}_{\Lambda pj}) \\ + \sum_{p=1}^{2}\sum_{q=p+1}^{3}\sum_{j=1}^{N_s-1}\sum_{l=j+1}^{N_s}\sqrt{I_{pj}I_{ql}}\,\exp[\pm i(\phi_{0pj}-\phi_{0ql})]\delta[\hat{f} \mp (\hat{f}_{\Lambda pj}-\hat{f}_{\Lambda ql})] \end{array} \right\} \quad (4.11)$$

where * represents convolution, $\tilde{W}(\hat{f})$ is the Fourier transform of W(t), a continuous window function that represents the finite sampling duration and the envelope of the laser power spectrum. The first term between curly brackets in Eqn. (4.11) is part of the autocorrelation term and represents the dc term due to the reference and scattered wavefronts. The second, known as the cross-correlation term, represents the interference between the reference and all three illumination beams scattered at all layers within the sample and is given by the superposition of Dirac deltas δ that fall within bands in the frequency domain between frequencies $\hat{f}_{\Lambda p1}$ and $\hat{f}_{\Lambda pNs}$ which are, according to Eqn. (4.10), proportional to the optical paths Λ_{p1} and Λ_{pNs} corresponding to the first and last layers. The phase at the origin of each of these frequency components is given by $\phi_{0pj} = \phi_{pj}(m, n, 0)$. The third term, known as autocorrelation, represents the interference between pairs of scattering layers corresponding to either the same illumination beam or different ones. It is represented by Dirac deltas at frequencies $\pm(\hat{f}_{\Lambda pj} - \hat{f}_{\Lambda ql})$. In order for all the cross correlation frequency bands to be fully separated in the frequency domain and avoid overlap with the autocorrelation terms, the carrier frequencies $\hat{f}_{\Lambda pj}$ and $(\hat{f}_{\Lambda pj} - \hat{f}_{\Lambda ql})$ must be carefully set. This is done by adjusting the optical paths Λ_{pj} by moving the collimating lenses L_1, L_2 and L_3, which will shift the

wavefront represented in Eqn. (4.1) by position vector $\mathbf{r}_p$. The second term in Eqn. (4.1) thus adjusts a 'piston' term in the optical path difference Λ_{pj} and is characteristic of each illumination beam.

4.5 Range and resolution of the optical path difference measurement

The maximum unambiguous range that the optical path difference may take is given by the Shannon sampling theorem as discussed in section 3.2.3 of Chapter 3. The maximum allowed optical path difference and resolution for a single scattering surface and for a bulk material are already described in Eq. (3.11) to Eq. (3.14) in that section.

4.6 Conclusion

A detailed design of a phase-contrast three dimensionally sensitive WSI setup has been demonstrated. The working principle and basic equations were developed for three illumination beams. The mathematical framework provides the required tools to obtain 3-D reconstructions of the material microstructure and also depth-resolved phase information that can be used to evaluate all the three components of the displacement vector at each voxel of the data volume. This technique can be viewed as frequency multiplexed OCT in which each illumination channel carries information for a specific displacement sensitivity that will be described in detail in next two chapters.

Chapter 5 presents experimental results of the reconstruction of a single scattering surface which is used to calibrate the full-field WSI technique with three illuminations. It also presents the description of the procedure of separation of images in the frequency domain for a single scattering surface, the least square fitting and re-registration of each image plane in the volume, calculation of all zenith and azimuth angles of the illumination beams and finally the construction of the sensitivity matrix that results from all three illumination directions.

Chapter 5

5 Surface reconstruction for system calibration purposes

5.1 Introduction

A multiple sensitivity phase-contrast WSI has been developed with the aim of measuring three orthogonal components of displacements in the full volume of the scattering materials. To generate multiple images in the frequency domain with differing sensitivity vectors that are required to determine three dimensional object displacements, multiple illuminations of the object must be used. The three sensitivity vectors can be generated by two methods, either using a single illumination direction and multiple observation directions or by multiple illumination directions and a single observation direction. The later one is considered here where for each illumination the light scattered back from the surface (in case of an opaque

sample) or from each of the different layers of a bulk material is combined with a reference wave. The optical path difference between the back scattered light and the reference beam varies linearly with the depth of the scattering layers for each illumination beam and as a consequence, the frequency of the interference signal produced also varies linearly with optical path difference or with depth.

The multiple interference signals generated by several illuminations can readily be separated in the frequency space using WSI by adjusting the optical path difference between the reference and each illumination beam. This can be done by moving the respective collimating lenses on three different illumination beams slightly either towards or away from the sample with respect to a delay line. A sphere can be considered with a centre at the intersection point of the sample surface and the optical axis of the whole system and it can be assumed that all optical fibres which are the sources of three illumination beams contain the same optical paths inside them, then the distances from the illuminating lenses to the sphere actually measure their relative optical path differences, which are used to separate signals corresponding to different sensitivity directions in the frequency domain. Thus the technique can be viewed as frequency multiplexed OCT in which the image produced for each illumination can be reconstructed and separated in frequency domain. This is a form of sensitivity multiplexing which involves assigning non-overlapping frequency ranges to different signals or to each illumination beam in the set-up.

This chapter describes the system calibration by imaging a single scattering surface with multiple illuminations, separation of multiple signals in the frequency domain, calculation of zenith and azimuth angles of illumination vectors, evaluation of sensitivity vectors and observation vector and finally the formation of the sensitivity matrix.

5.2 Image acquisition and construction of 3-D magnitude and phase volumes

A flat scattering surface (sandblasted Aluminium plate) was studied first using the interferometer shown in Fig. 4.1 of Chapter 4. The purpose of this was to examine the performance of the tunable laser and the near infrared (NIR) photo-detector in terms of the linearity of the wavenumber scan $k(t)$ and the intensity noise, which ultimately evaluate the width of the peak that represents the position of the sample surface in the Fourier transformed data $\tilde{I}(\hat{f})$, i.e. the optical path resolution $\delta\Lambda$. This will be described in detail in section 5.2.1.

Due to the oblique illumination beams, the reconstructions of scattering surface appear tilted. In the case of scattering surface the optical path difference in Eqn. (4.1), reduces to

$$\Lambda_p(x, y, z) = n_0[\mathbf{e}_p \cdot (\mathbf{r}_0 - \mathbf{r}_p) + \mathbf{e}_p \cdot (\mathbf{r} - \mathbf{r}_0) + \mathbf{e}_o \cdot \mathbf{r}] \qquad (5.1)$$

with $\mathbf{r}$ the position vector of point (x, y, z) now representing a point on the surface - see Fig. 4.10(b) of Chapter 4. As the orientation of these tilted image planes in the frequency domain is directly related to the orientation of the tilted illumination beams, they can be conveniently used to calculate the illumination unit vectors $\mathbf{e}_p$, i.e. the zenith and azimuth angles of all illumination vectors as shown in the insert of Fig. 4.1 of Chapter 4. Therefore the sensitivity vectors that are linked to measure phase changes to determine actual 3-D displacement fields can be evaluated. This is described in sections 5.2.2, 5.2.3 and 5.2.4.

5.2.1 Depth range and depth resolution

A sequence of 8748 frames of 64×64 pixels images was recorded whilst scanning the laser frequency over the full range from $v_1 = 237.9305$THz to $v_2 = 220.4356$THz ($v = c/\lambda = ck/2\pi$, with $c = 2.9979243 \times 10^8$m/sec the speed of light in vacuum) which corresponds to a wavelength range 1260nm$\leq \lambda \leq$1360nm and a wavevector range 4.9867×10^6m$^{-1} \leq k \leq 4.6200 \times 10^6$m^{-1}and the intensity $I(m, n, t)$ was encoded in 14 bits. The frequency sweep was done in 'step mode' and the step in between two consecutive frequencies was fixed at 0.002 THz, corresponding to the wavelength step of 0.011nm and wavevector step of 41.9m^{-1}.

The field of view was ultimately limited by the random access memory available for data processing, but 512×640 pixels (rows, columns) images could be acquired with the NIR camera. After a complete scan, the stack of images of a 3-D intensity volume was stored - see Fig. 5.1.
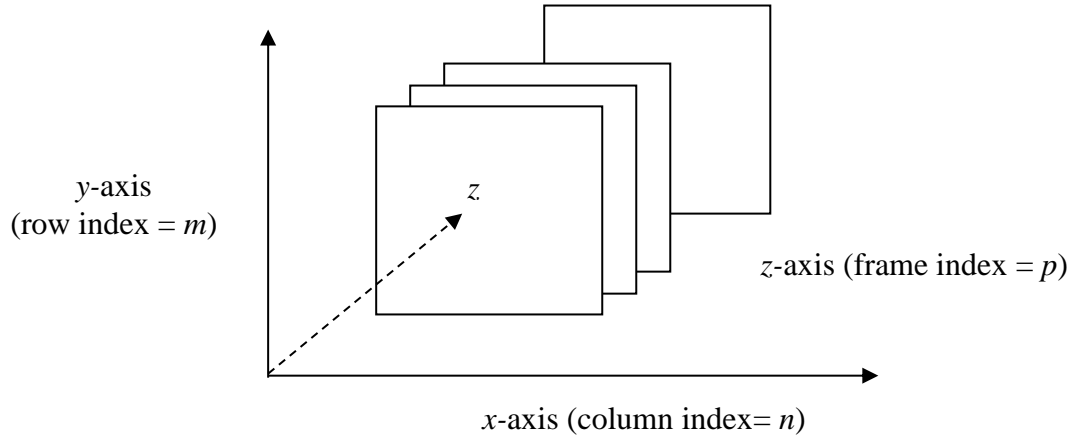
Figure 5. 1 3-D data volume obtained by WSI

Fourier transformation of the recorded 3-D (for a pixel (*m, n*) intensity distribution was performed on a pixel wise basis along the *t*-axis, leading to a spectrum that is directly related to the position of the surface along the observation direction at coordinates $x=np_x$, $y=mp_y$. The tunable laser delivered a nearly constant power during the whole scan, which translated in a good level of signal modulation. Fig. 5.2(a) shows the intensity for a pixel at the centre of the field of view (FOV), plotted against frame number, i.e. $I(32, 32, t)$. The mean value of the intensity signal was subtracted to eliminate the dominant DC peak at $f_{\Lambda p}=0$. Also, the intensity signal was multiplied by a Hanning window $W(t) = 0.5\{1 - \cos[2\pi(t + N_t/2)/N_t]\}$, $-N_t/2 \leq t \leq +N_t/2$, to reduce spectral leakage between the otherwise prominent secondary lobes of a rectangular window $\tilde{W}(\hat{f})$. The Fourier transform of the signal in Fig. 5.2(a) is shown in Fig. 5.2(b) in the positive frequency axis and revealed six peaks. The frequency axis was converted to optical path difference by using Eqn. (4.9). Peaks are labelled according to which pair of beams interfere; for instance, "01" indicates interference between the reference beam and object beam 1 and "23" indicates interference between object beams 2 and 3 (see insert in Fig. 4.1 of Chapter 4). Notice in Fig. 5.2(b) how peaks "01", "02", "03" are fully separated. This separation is adjusted by moving lenses L_1, L_2 and L_3 towards or away from the sample so that the peaks do not overlap with the cross interference ones and no aliasing is introduced. Fig. 5.2(c) shows peak "01" in more detail. It has a width of ~0.06 mm, which compares well with the expected value of 0.068 mm from Eqn.(3.12).
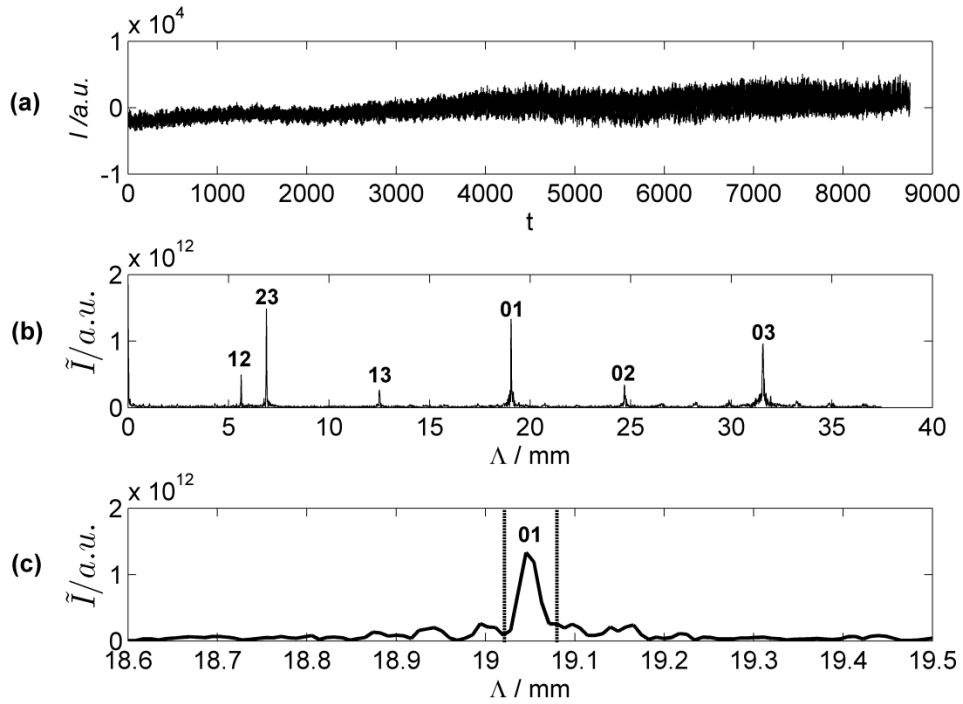
Figure 5. 2 Intensity signal recorded at one pixel during a WSI scan when an opaque flat surface is imaged under 3-beam illumination (a); its corresponding Fourier transform, showing cross correlation terms "01", "02" and "03" and autocorrelation terms "12", "13" and "23" (b); peak 01 in more detail (c).

When this computation was done for every pixel and the cross interference between the object beams were neglected, an instance of the surface emerged for each object beam within the so-called 'reconstruction volume' in the 'direct', i.e. (x, y, Λ), space. As mentioned before, the surface appeared with different tilts for each illumination direction.

Fig. 5.3 shows a slice through the reconstructed volume parallel to the $y\Lambda$ plane for $x=32$. The three lines to the left correspond to the cross interference between the object beams. The three on the right correspond to the interference between the object beams and the reference beam, and thus represent the object as reconstructed for each illumination direction.
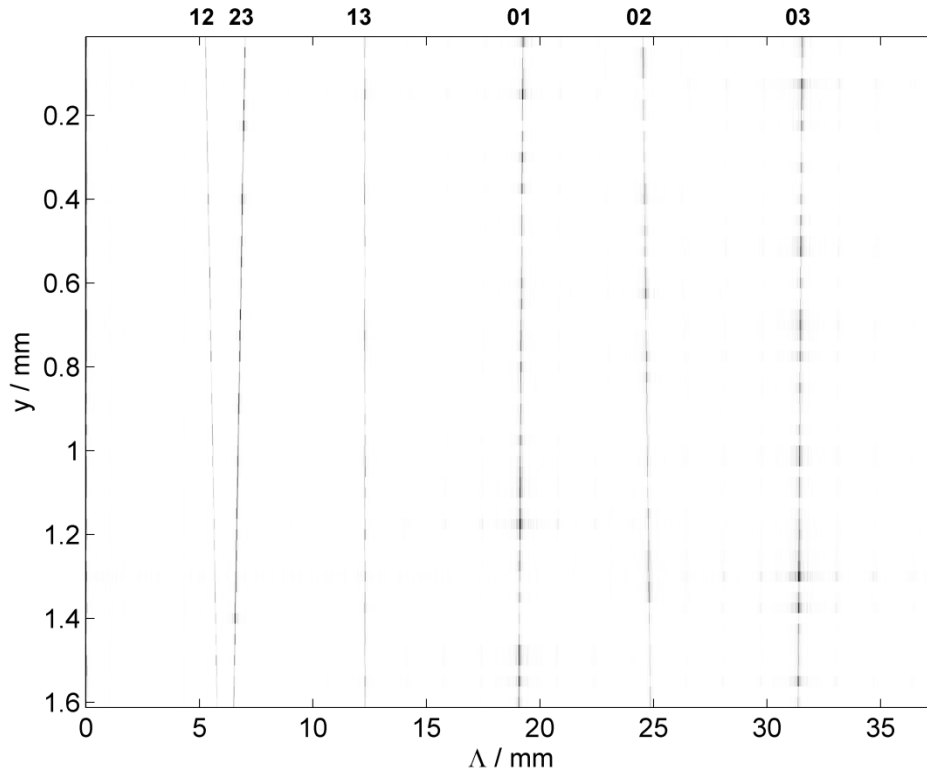
Figure 5. 3 *y*Λcross-section of the magnitude of the Fourier transform volume obtained when a flat opaque surface is reconstructed, shown in reverse contrast for clarity. Lines corresponding to the auto correlation terms "12", "23" and "13" and the cross correlation terms "01", "02" and "03" are clearly visible. Their tilt is a consequence of the oblique illumination.

5.2.2 Reconstruction of a single scattering surface

In order to automatically isolate the reconstructions of planes "01", '02" and "03", some simple image processing functions were used to obtain a 'mask' for each plane. The 'masks' were obtained by : 1) thresholding the magnitude of the Fourier transform in Fig. 5.3: 2) using morphological operations to connect holes in the reconstructed planes and eliminate isolated (disconnected) voxels – see Fig. 5.4; 3) labelling the different regions to identify the 'masks' – see Fig. 5.5.
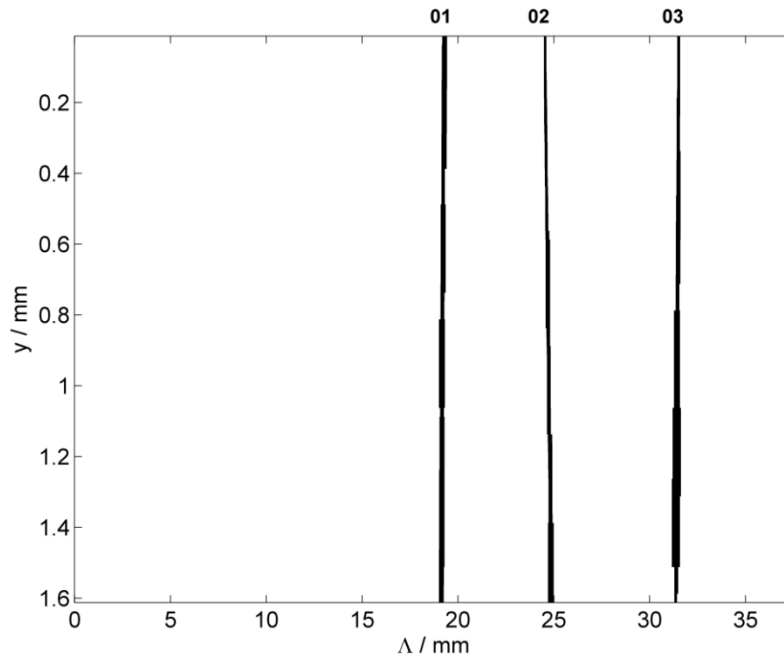
Figure 5. 4 $y\Lambda$ cross-section of the magnitude of the Fourier transform volume obtained after thresholding and morphological operations. The cross correlation terms "01", "02" and "03" are clearly visible.
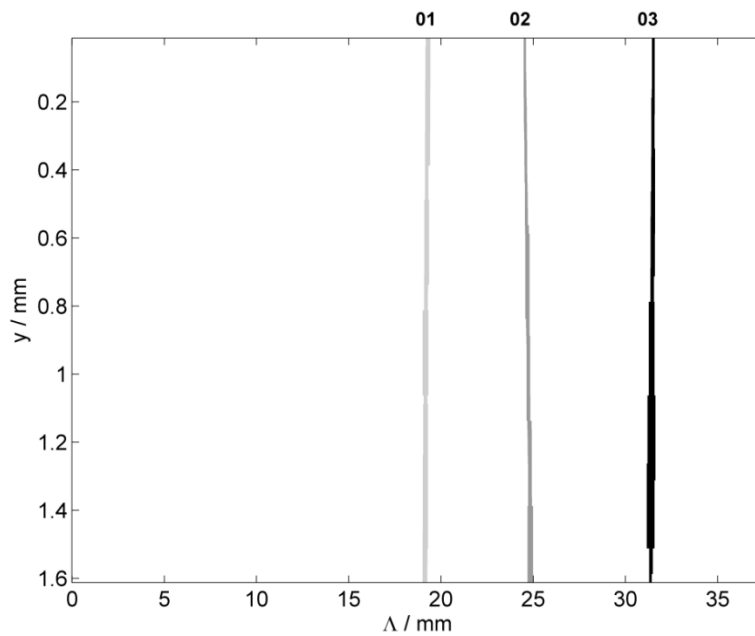
Figure 5. 5 $y\Lambda$ cross-section of the magnitude of the Fourier transform volume obtained after labelling. The cross correlation terms "01", "02" and "03" are clearly visible.

5.2.3 Plane fitting to the reference surface reconstruction

The first labelled object in the Fig. 5.5 was masked from the reconstructed 3-D volume data and then the maximum values of the FFT magnitude along z-axis were found within the mask for each for each (x, y) position. This is done to isolate peak "01" for all pixels in the FOV, and leads to a tilted plane in 3-D space. So we had ended up with a single peak point along the z axis for each (x, y) position and all peak positions were used to reconstruct a 2-D array, which was the first tilted image plane. The same procedure was applied to the second and third labelled objects in Fig. 5.5, thus leading to a total of three tilted reconstructed flat surfaces. Finally, a plane was fitted to each surface. Figure 5.6(a) shows the reconstructed surfaces, Fig. 5.6(b) shows the fitted planes, and Fig. 5.6(c) shows the error between them. The same procedure was again applied to all surface reconstructions "01", "02" and "03".
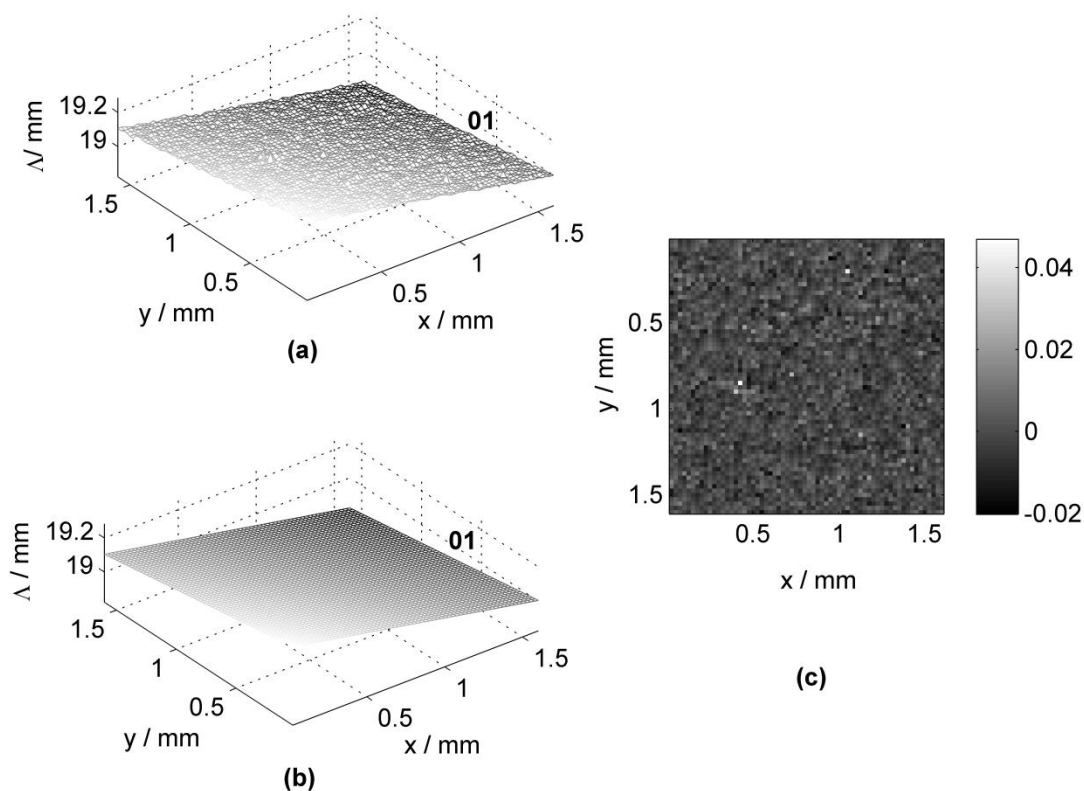
Figure 5. 6 (a) The reconstructed flat reference surface, (b) the plane of best fit for illumination beam "01" and (c) 2-D error between reconstruction and plane of best fit. .

5.2.4 Evaluation of illumination and sensitivity vectors

As the orientation of the reconstructed surfaces is uniquely related to the illumination directions, they can be used to calculate the orientation of the illumination beams $\mathbf{e}_p$. Let us consider three separate points P_1, P_2, P_3 on any one of the least square fitted planes, in xy-Cartesian coordinate system as shown in Fig. 5.7.
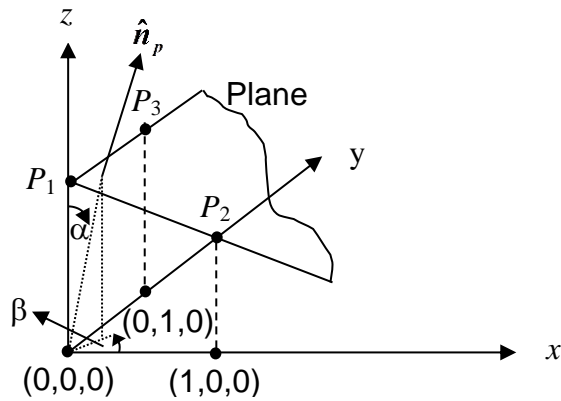
Figure 5. 7 Three separate points on any one fitted image plane

The equation of a best fit plane can be written as,

$$z(x, y) = ax + by + c \qquad (5.2)$$

where, a, b, c are the coefficients obtained from least square fitting.

$z(0,0) = c$, defining the point P_1 : $(0, 0, c)$;

$z(1, 0) = a + c$, defining the point P_2 : $(1, 0, a + c)$;

$z(0, 1) = b + c$, difining the point P_3 : $(0, 1, b + c)$;

The normal of each plane can be found by taking the cross product of two vectors parallel to each plane:

$$\hat{n} = (P_1 - P_2) \times (P_1 - P_3) \qquad (5.3)$$

where $\hat{n} = (n_x, n_y, n_z)$ and n_x, n_y, n_z are the components of normal vector along x, y and z directions. It is convenient to denote the normal vector to the p-th reconstructed surface by $\mathbf{n}_p$, and express it in terms of α_p and β_p, the zenith and azimuth angles that $\mathbf{n}_p$ subtends from the observation axis and the x-axis, respectively. It can be shown that:

$$\mathbf{n}_p = (\sin\alpha_p \cos\beta_p, \sin\alpha_p \sin\beta_p, \cos\alpha_p) \quad , \tag{5.4}$$

or equivalently:

$$\alpha_p = \cos^{-1}(\hat{\mathbf{k}} \cdot \mathbf{n}_p) \tag{5.5}$$

$$\beta_p = \tan^{-1}\left(\frac{\hat{\mathbf{j}} \cdot \mathbf{n}_p}{\hat{\mathbf{i}} \cdot \mathbf{n}_p}\right) \tag{5.6}$$

$\hat{\mathbf{i}}, \hat{\mathbf{j}}$ and $\hat{\mathbf{k}}$ are unit vectors along the x, y and z axes, respectively.

From Fig. 4.10(b) in Chapter 4, it follows that the optical path difference between points $\mathbf{r}_0$ and $\mathbf{r}$ is $\Lambda(\mathbf{r}) - \Lambda(\mathbf{r}_0) = n_0 \mathbf{e}_p \cdot (\mathbf{r} - \mathbf{r}_0) = n_0 |\mathbf{r} - \mathbf{r}_0| \sin\theta_p$, with θ_p the zenith angle of $\mathbf{e}_p$ to the observation direction. This is illustrated in the diagram in Fig. 5.8, which in the vertical axis shows relative distance along the observation direction and in the horizontal axis shows points $\mathbf{r}_0$ and $\mathbf{r}$ on the surface.
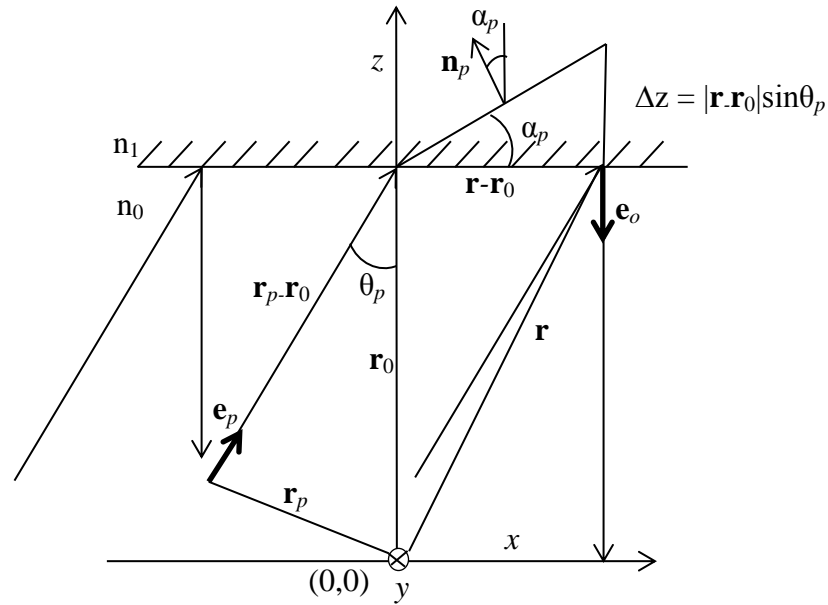
Figure 5. 8 Geometric relationship between the illumination vector e_p and the normal to the reference surface reconstruction, n_p. The plane of the figure corresponds to the plane of the azimuth of n_p and e_p.

If $n_0=1$ then the optical path difference represents geometrical distance, i.e. $\Delta z=k.(\mathbf{r}\text{-}\mathbf{r}_0) = |\mathbf{r}\text{–}\mathbf{r}_0|\sin\theta_p$. As the surface normal vector $\mathbf{n}_p$ subtends an angle α_p to the z-axis (Eqn. (5.4)), then it can be seen from the Fig. 5.8 that,

$$\tan\alpha_p = \frac{|\mathbf{r}-\mathbf{r}_0|\sin\theta_p}{|\mathbf{r}-\mathbf{r}_0|} = \sin\theta_p \tag{5.7}$$

Similarly, it can be shown that the azimuth of the normal vector, β_p, is simply related to the azimuth of corresponding illumination vector, ξ_p, by

$$\xi_p = \beta_p + \pi \tag{5.8}$$

Therefore, once the normal vectors $\mathbf{n}_p$ have been obtained for all surface reconstructions via plane fitting, the angles α_p and β_p are obtained from Eqns. (5.5) and (5.6) and finally the illumination direction $\mathbf{e}_p$ is determined using Eqns. (5.7) and (5.8) as

$$\mathbf{e}_p = (\sin\theta_p\cos\xi_p, \sin\theta_p\sin\xi_p, \cos\theta_p) \tag{5.9}$$

The sensitivity vectors of the system can now be evaluated directly using Eqn. (5.9) and the observation vector (Fig. 4.10 in Chapter 4) is

$$\mathbf{e}_o= (0, 0, -1) \tag{5.10}$$

The illumination vectors are given by,

$$\mathbf{k}_1 = \frac{2\pi}{\lambda}(\sin\theta_1\cos\xi_1, \sin\theta_1\sin\xi_1, \cos\theta_1) \tag{5.11}$$

$$\mathbf{k}_2 = \frac{2\pi}{\lambda}(\sin\theta_2\cos\xi_2, \sin\theta_2\sin\xi_2, \cos\theta_2) \tag{5.12}$$

$$\mathbf{k}_3 = \frac{2\pi}{\lambda}(\sin\theta_3\cos\xi_3, \sin\theta_3\sin\xi_3, \cos\theta_3) \tag{5.13}$$

In general form the sensitivity vector can be written as,

75

$$\mathbf{S}_p = \frac{2\pi}{\lambda_c}(\mathbf{e}_p - \mathbf{e}_o) = \frac{2\pi}{\lambda_c}(\sin\theta_p \cos\xi_p, \sin\theta_p \sin\xi_p, 1+\cos\theta_p) \, , \qquad (5.14)$$

or, in matrix form:

$$\mathbf{S} = \frac{2\pi}{\lambda_c}\begin{pmatrix} \sin\theta_1 \cos\xi_1 & \sin\theta_1 \sin\xi_1 & 1+\cos\theta_1 \\ \sin\theta_2 \cos\xi_2 & \sin\theta_2 \sin\xi_2 & 1+\cos\theta_2 \\ \sin\theta_3 \cos\xi_3 & \sin\theta_3 \sin\xi_3 & 1+\cos\theta_3 \end{pmatrix} . \qquad (5.15)$$

The elements of the sensitivity matrix are the sensitivity vectors $\mathbf{S}_1 \equiv \mathbf{k}_1 - \mathbf{k}_0, \mathbf{S}_2 = \mathbf{k}_2 - \mathbf{k}_0, \mathbf{S}_3 = \mathbf{k}_3 - \mathbf{k}_0$, respectively. All fitted planes are shown in the data volume of Fig 5.9(a) and the normal vector to reconstruct the surface "01" is shown in Fig. 5.9(b). The sensitivity and observation vectors, as evaluated from the reference surface reconstructions using Eqns. (5.2)-(5.14) are shown in the Fig. 5.9(c}.
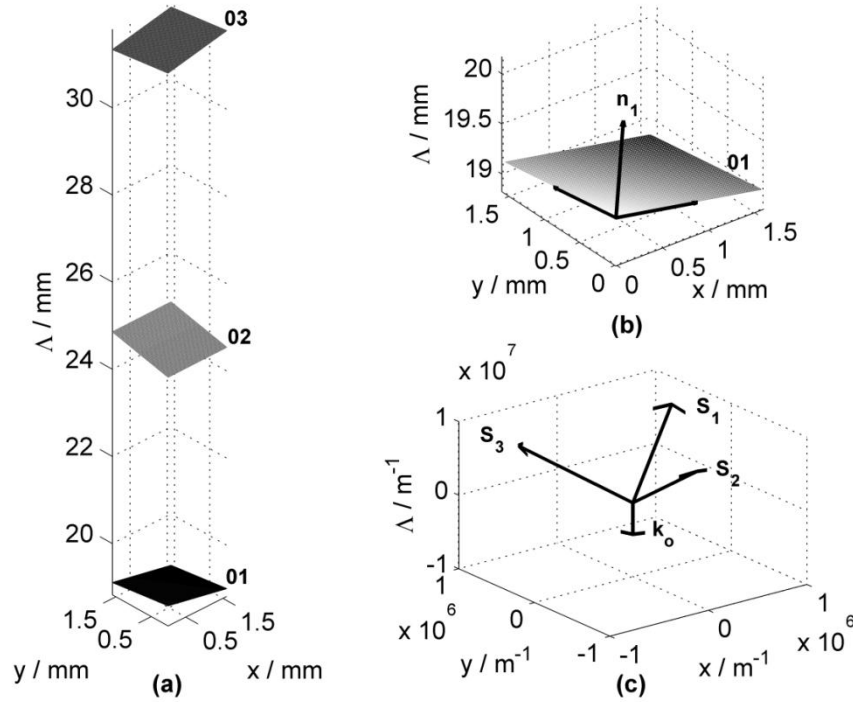
Figure 5. 9 Planes of best fit obtained for reconstructions "01", "02" and "03" for a reference flat surface. (a) Plane of best fit for reconstruction "01" showing its normal vector (b) and sensitivity and observation vectors, as evaluated from the reference surface reconstructions using Eqns. (5.2)-(5.14) (c).

5.3 Conclusion

In this Chapter, a flat opaque and optically rough surface was used to evaluate the illumination and sensitivity vectors of the full sensitivity WSI system. The flat surface can thus be used as a reference (or datum) for subsequent reconstructions. Multiple signals were separated in frequency space by adjusting the optical path difference between each illumination and the reference beam.

The next chapter presents the measurements of 3-D displacement fields at each voxel within the material by measuring changes in the 3-D phase distributions between two separate scans before and after deformation. Using three directions of illuminations and one direction of observation, it is possible to simultaneously record three phase distribution volumes, each associated to an independent sensitivity vector. The sensitivity matrix basically links the three different measured phase values at a particular voxel from all phase difference volume elements with the displacement vectors (u, v, w) of that corresponding point in the object. This is described in detail in Chapter 6 and validated using three controlled rigid body translations of a semitransparent scattering sample:

     1. in-plane rotation,

     2. out-of-plane tilt and

     3. both in-plane rotation and out-of-plane tilt.

Chapter 6

6 Volume reconstruction of internal structure and 3-D displacement fields

6.1 Introduction

The technique presented in this thesis was designed to measure all orthogonal components of displacement in the full volume of scattering materials with interferometric sensitivity. This can be achieved by measuring changes in the 3-D phase distributions between two successive scans before and after deforming or moving the sample. By using three non-coplanar illumination directions it is possible to simultaneously evaluate the phase change at every voxel within the reconstructed volume. Once the sensitivity matrix has been established as described in Chapter 5.

The phase data evaluated for each illumination direction has to be re-mapped into a common coordinate system so that corresponding points in the 3-D data volumes represent the same position within the object. This process is known as re-registration and is described in section 6.2 of this Chapter.

The relationship between the measured phase change and the displacement field can be expressed in matrix form as

$$\mathbf{\Phi} = \mathbf{S}\Delta\mathbf{r} \qquad (6.1)$$

$\mathbf{S}$ is the sensitivity matrix defined in Eqns (5.15) and (5.16), $\Delta\mathbf{r}= (u, v, w)^{\mathrm{T}}$ and $\mathbf{\Phi}= (\Delta\phi_1, \Delta\phi_2, \Delta\phi_3)^{\mathrm{T}}$ ($^{\mathrm{T}}$ indicates transposed), where u, v, and w represent the displacements along the x, y and z axes, respectively and $\Delta\phi_1$, $\Delta\phi_2$, $\Delta\phi_3$ are three phase difference volumes obtained from the reconstructions corresponding to the three illumination beams :

$$\begin{pmatrix} \Delta\phi_1 \\ \Delta\phi_2 \\ \Delta\phi_3 \end{pmatrix} = \frac{2\pi}{\lambda_c} \begin{pmatrix} \sin\theta_1\cos\xi_1 & \sin\theta_1\sin\xi_1 & 1+\cos\theta_1 \\ \sin\theta_2\cos\xi_2 & \sin\theta_2\sin\xi_2 & 1+\cos\theta_2 \\ \sin\theta_3\cos\xi_3 & \sin\theta_3\sin\xi_3 & 1+\cos\theta_3 \end{pmatrix} \begin{pmatrix} u \\ v \\ w \end{pmatrix}. \qquad (6.2)$$

Finally, the 3-D distribution of the displacement vector within the sample is obtained by using the inverse of the sensitivity matrix as

$$\Delta\mathbf{r} = \mathbf{S}^{-1}\mathbf{\Phi} \qquad (6.3)$$

This operation has to be performed in a voxel by voxel basis in the reconstructed volume.

6.2 Data acquisition and volume reconstruction

A sequence of 8748 frames of 64×64 pixels images of an epoxy resin block (seeded with scattering particles) was recorded whilst scanning the laser frequency over the full range from v_1= 237.9305THz to v_2= 220.4356THz.The intensity $I(m, n, t)$ was encoded in 14 bits and subsequent data analysis took place on a pixel-wise basis. Figure 6.1 shows the semi-transparent scattering sample.

The sample used in the present experiment is the epoxy resin block seeded with scattering particles (titanium oxide, 1µm average diameter) much smaller than the size of the volume point spread function (PSF) of the WSI system (25µm laterally and 68µm axially). The particles/resin volume fraction is $\sim 3 \times 10^{-3}$, which results in ~ 100 particles per PSF.
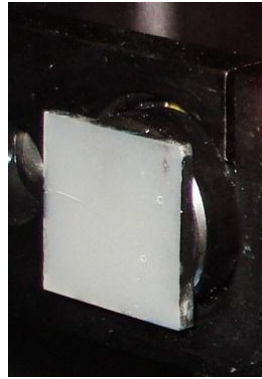
Figure 6.1 An epoxy resin block seeded with scattering particles

The cross correlation image volumes were separated from the autocorrelation terms. The autocorrelation terms were made due to the cross interference between the object beams and they were neglected. As mentioned before, the volume appeared with different tilts for each illumination direction. Figure 6.2 shows a slice through the reconstructed volume parallel to the $y\Lambda$ plane. Fourier transformation of the resulting 3-D intensity distribution along the time axis through each slice reconstructs the scattering potential within the volume. In the positive frequency axis the spectrum reveals several amplitude peaks. Prior to the Fourier transform, the mean value of the intensity signal was subtracted and the signal was multiplied by a Hanning window for each slice along time axis. Each $y\Lambda$ slice reveals three thick 'bands' due to the power reflected from the all different layers of a sample block, for all three illuminations. The three microstructural reconstructions of the sample block can then be obtained in the spatial domain by simply exchanging the frequency axis to the position axis or optical path axis. The volumes overlapped with each other to the left (hardly visible in Fig. 6.2) correspond to the cross interference between the object beams. The three on the right correspond to the interference between the object beams and the reference beam, and thus represent the object volume as reconstructed for each illumination direction.

Figure 6.3 shows a block diagram of the main data processing steps for both the reference surface and the volume sample. The sections that follow address these stages in detail.
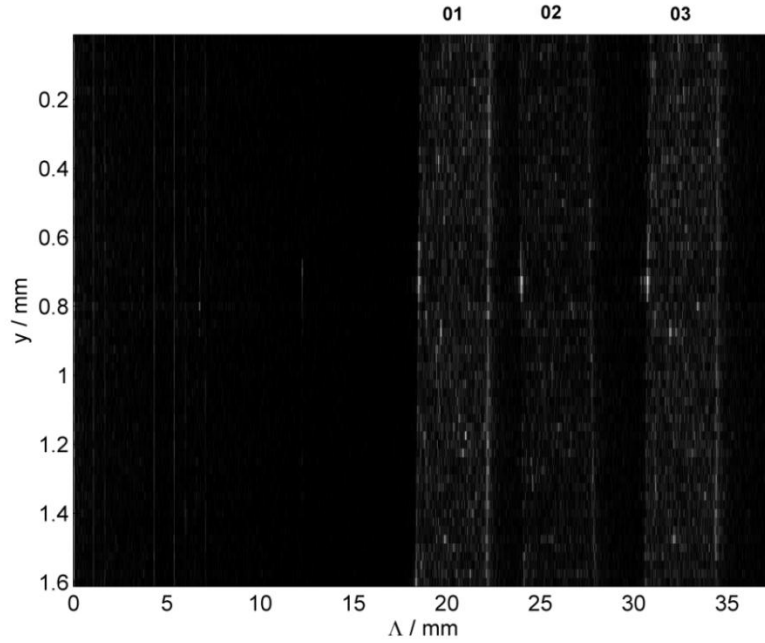
Figure 6.2 A $y\Lambda$ slice through the reconstructed volume
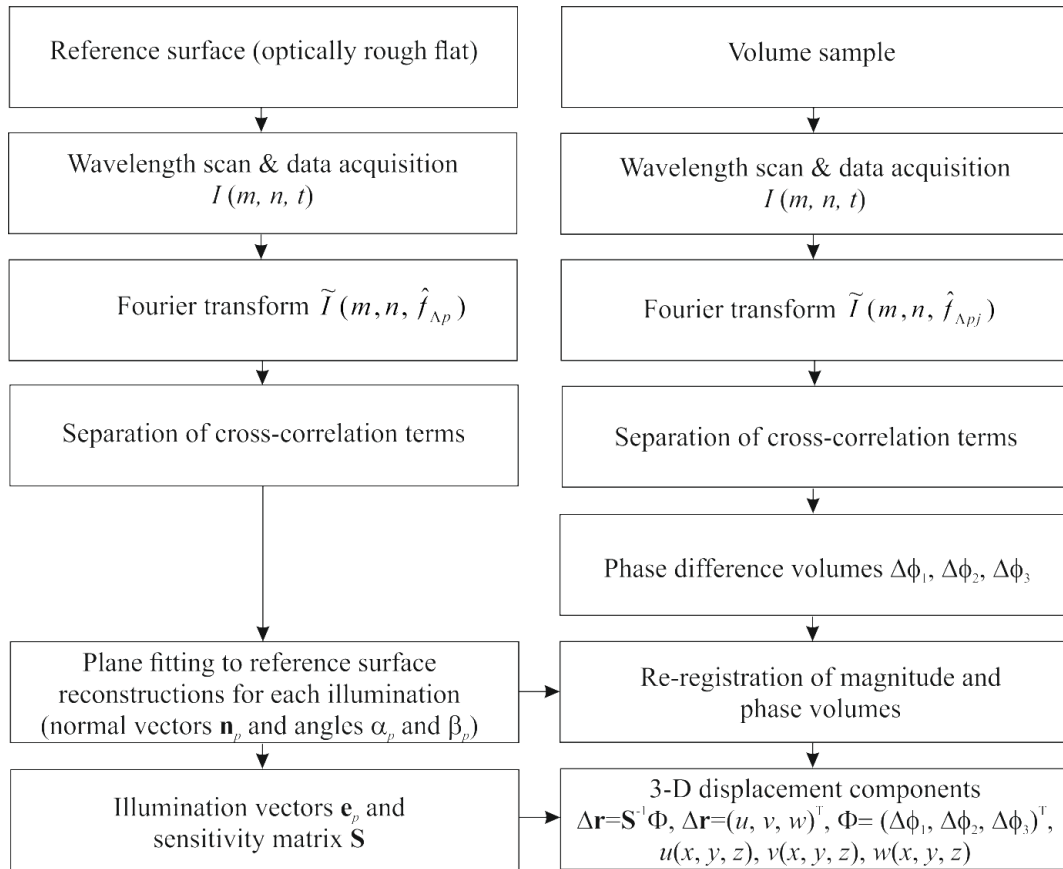
Figure 6.3 Schematic diagram of the data processing for the reference surface and a volume sample.

6.3 Volume registration

Registration is thus the process by which corresponding voxels in each reconstructed volume are brought to the same position in a common coordinate system. This is usually done by a mathematical transformation that may include a combination of translation, rotation and shear in most cases. The registration requires the subtraction of the carrier frequency for each illumination direction described by the first term between squares brackets in Eqn. (5.1). Moreover, subtraction of the position dependent optical path difference described in the second term between square brackets in Eqn. (5.1), $\mathbf{e}_p \cdot (\mathbf{r} - \mathbf{r}_0)$, was also required. Fortunately, this was a simple task once the normal vectors $\mathbf{n}_p$ had been estimated, and could be done efficiently through a simple geometric transformation.

6.4 3-D full-sensitivity displacement evaluation

In this section, we present experimental results on the measurement of 3-D displacement fields within the bulk of an epoxy resin block seeded with scattering particles (titanium oxide, 1 μm average diameter) much smaller than the size of the volume point spread function (PSF) of the WSI system (25μm laterally and 68μm axially). The particles/resin volume fraction was $\sim 3 \times 10^{-3}$, which resulted in ~100 particles per PSF. If particles were sparse as required by particle image velocimetry, there would be regions in the volume that would not contribute any signal and thus no displacement information could be retrieved. On the other hand, a high volume fraction would result in multiple scattering, which increases the noise floor and reduces the depth resolution of the system (the point spread function broadens in the axial direction). This is because of the extended optical path due to multiple scattering events, which effectively de-localises the scattering centres.

6.4.1 System validation: Evaluation of phase difference volumes due to rigid body motion

In order to validate the WSI system and to measure the displacement fields within the volume of the material, the epoxy resin block seeded with scattering particles was fixed on the tilting

stage and as well as on a rotation stage as shown in Fig. 6.4 below. The displacement could be introduced in two ways: either in-plane rotation on the xy-plane (see Fig. 4.1in Chapter 4) or out-of-plane tilt about the x-axis. The controlled displacements were easy to implement through these stages and provided a benchmark to validate the full field measurements obtained with the WSI system.
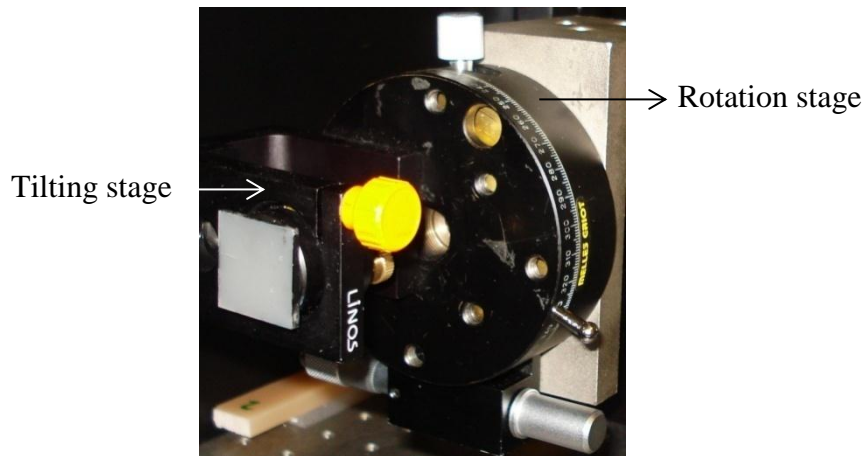
Figure 6.4 Epoxy resin block fixed on tilting stage and a rotating stage

.

Three different cases were considered: 1) In-plane rotation, 2) Out-of-plane tilt, and 3) Both in-plane rotation and out-of-plane tilt simultaneously. The sample was first fixed on the rotation and tilting stages as shown in Fig. 6.4. Then, two full frequency scans were performed before and after moving the sample (with either rotation, tilt or both). Finally, the procedure shown schematically in Fig. 6.3 was followed.

6.4.2 In-plane rotation
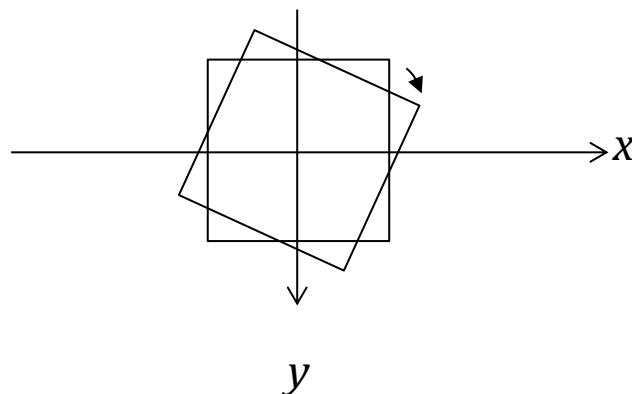
Figure 6.5 In-plane rotation

In case of an in-plane rotation, the epoxy resin block sample was rotated on the *xy*-plane as shown in Fig. 6.5.

Figure 6.6 shows '*y*Λ' cross sections of the registered reconstructed volumes of the sample, "01", "02" and "03", corresponding to each of the illumination beams. The top row shows the magnitude of the Fourier transform, whilst the bottom row shows the wrapped phase difference volumes $\Delta\phi_1$, $\Delta\phi_2$ and $\Delta\phi_3$ obtained after rotating the sample by 0.11° (phase values between $-\pi$ and π). A cubic kernel of $7\times7\times7$ voxels was used on the terms $\sin(\Phi)$ and $\cos(\Phi)$ before the `atan` function evaluation, to reduce speckle noise. The fringes in Fig. 6.6 represent a phase change proportional to the displacement of the sample along the sensitivity vectors for each illumination beam. Larger in-plane rotations and tilts lead to an increase in the number of fringes. The phase gradient is related to the direction of the displacements.
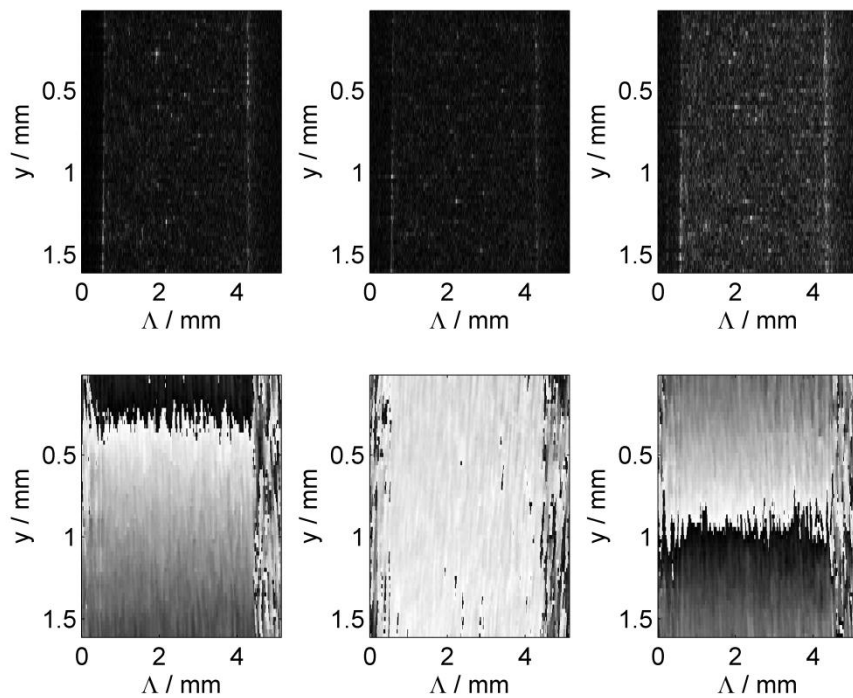
Figure 6.6 Reconstructed cross-sections of the magnitude and wrapped phase volumes of a semitransparent scattering sample that has undergone in-plane rotation (phase values between -π and π).

6.4.3 Out-of-plane tilt
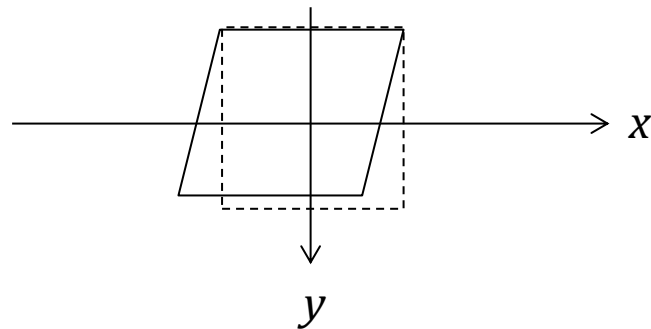
Figure 6.7 Out-of-plane tilt

In order to introduce known out-of-plane displacements, the epoxy resin block sample was tilted about the *x*-axis as shown in Fig. 6.7.

Figure 6.8 shows '*y*Λ' cross sections of the registered reconstructed volumes of the sample, "01", "02" and "03", corresponding to each of the illumination beams. The top row shows the magnitude of the Fourier transform, whilst the bottom two rows show the wrapped phase difference volumes $\Delta\phi_1$, $\Delta\phi_2$ and $\Delta\phi_3$ obtained after tilting the sample by 0.027° and 0.054° respectively. The phase values of the wrapped phase volume lie between $-\pi$ and π. A cubic kernel of 7×7×7 voxels was again used on the terms $\sin(\Phi)$ and $\cos(\Phi)$ before the `atan` function evaluation, for reducing speckle noise.
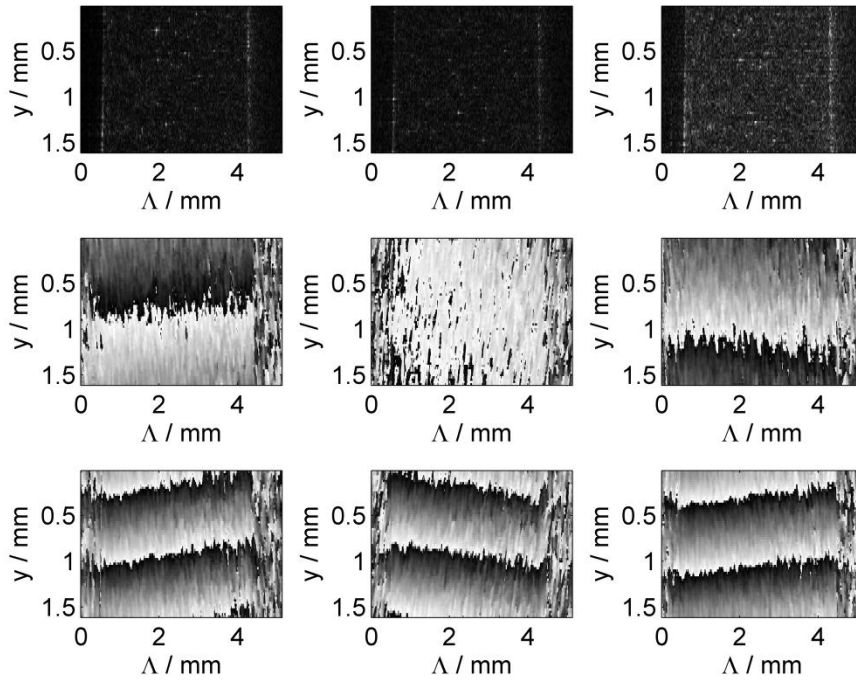
Figure 6.8 Cross-sections of magnitude (1st row) and the wrapped phase volumes (2nd row for 0.027$^{°}$ and 3rd row for 0.054$^{°}$ tilt) of a scattering sample that has undergone out-of-plane tilt (phase values between -π and π).

6.4.4   In-plane rotation and out-of-plane tilt

Figure 6.9 shows '$y\Lambda$' cross sections of the registered reconstructed volumes of the sample, "01", "02" and "03", corresponding to each of the illumination beams when in-plane rotation and out-of-plane tilt are introduced simultaneously. The top row shows the magnitude of the Fourier transform, whilst the bottom row shows the wrapped phase difference volumes $\Delta\phi_1$, $\Delta\phi_2$ and $\Delta\phi_3$ obtained after rotating by 0.11$^{°}$ and tilting the sample by 0.027$^{°}$ respectively (phase values between $-\pi$ and π). A cubic kernel of 7×7×7 voxels was used on the terms $\sin(\Phi)$ and $\cos(\Phi)$ before the `atan` function evaluation, to reduce speckle noise.
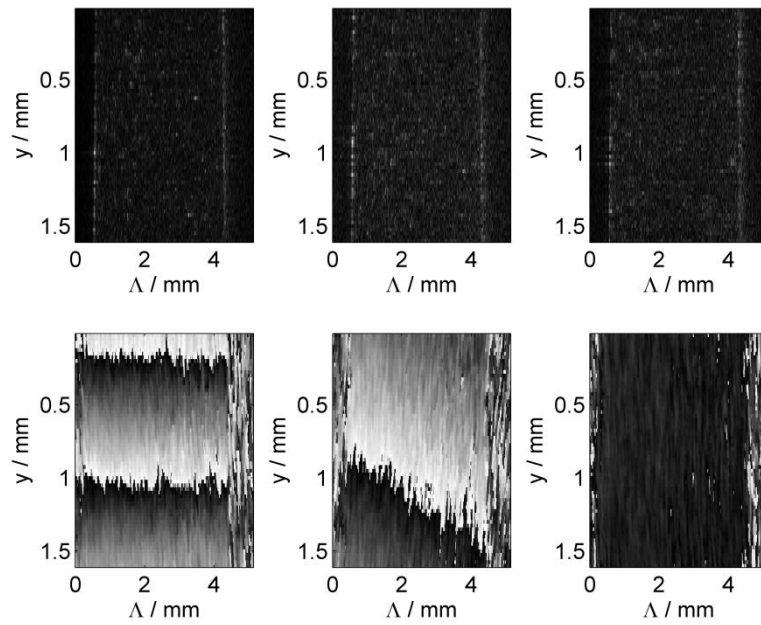
Figure 6.9 Cross-sections of magnitude and the wrapped phase volumes of a scattering sample that has undergone simultaneous in-plane rotation and out-of-plane tilt (phase values between $-\pi$ and π).

6.5 3-D phase unwrapping

The wrapped phase volumes were unwrapped with a 3-D path following algorithm designed to prevent the unwrapping path to go through phase singularity loops. Phase unwrapping is the process of recovering unambiguous phase values from phase data that are measured in modulo 2π rad (wrapped data) [128-131]. Phase discontinuities occur in areas that are locally under-sampled or where true discontinuities occur, due to layover in a topographic interferogram or a surface-breaking fault in a deformation interferogram. From the 3-D unwrapped phase volumes, 3-D displacements were been calculated for each voxel using the sensitivity matrix, the measured phase difference volumes and Eqns. (3.9) - (3.10).

6.6 3-D displacement results

The 3-D displacement field components *u*, *v* and *w* were finally calculated for each voxel in the measurement volume using Eqn. (6.3) for the case of 1) in-plane rotation, 2) out-of-plane

tilt, and for 3) both.

6.6.1 In-plane rotation

The presence of noise in the $\Delta\phi_1$, $\Delta\phi_2$ and $\Delta\phi_3$ phase volumes meant that an effective volume of only $31\times16\times301$ (m, n, p) voxels was obtained without any unwrapping errors. Figure 6.10 shows cross sections of the measured 3-D displacement field corresponding to the epoxy sample under in-plane rotation (corresponding to phase volumes shown in Fig. 6.6). The first row indicates the displacement component u and the second row v. From left to right, the columns show sections of the data volume on planes $y\Lambda$, $x\Lambda$ and xy. Notice the gradient in the u and v displacement fields, as expected for an in-plane rotation around the observation direction.
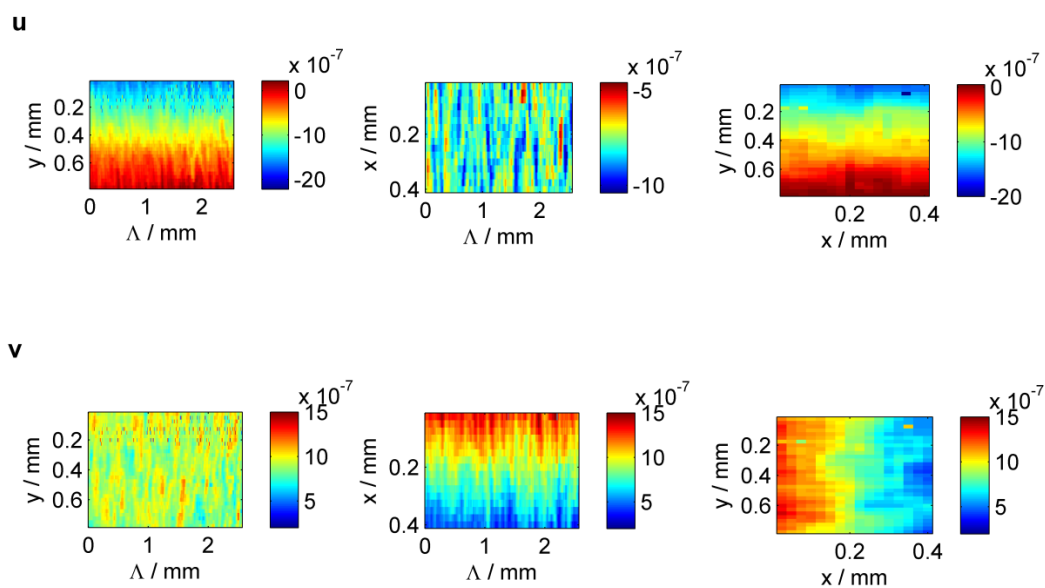
Figure 6.10 Cross sections of the measured 3-D displacement field corresponding to a sample after in-plane rotation. The rows indicate the displacement components u and v along the x, y and Λ axes. The columns show sections of the data volume on planes $y\Lambda$, $x\Lambda$ and xy. Displacements units: mm.

A comparison was made between the measured displacements with the known ones introduced with the rotation stage. The $u(x, y)$ and $v(x, y)$ displacements shown in Fig. 6.11 were averaged along the x and y axes, respectively, to reduce noise. Fig. 6.11 also shows the

'reference' displacements introduced with the rotation and tilting stages. The error-bars represent the root mean squared deviation of the displacement along respective rows and columns in Fig. 6.10. The root mean squared deviation between the theoretical and measured displacements $u(x, y, z)$ and $v(x, y, z)$ were 0.12 μm and 0.47 μm, respectively.
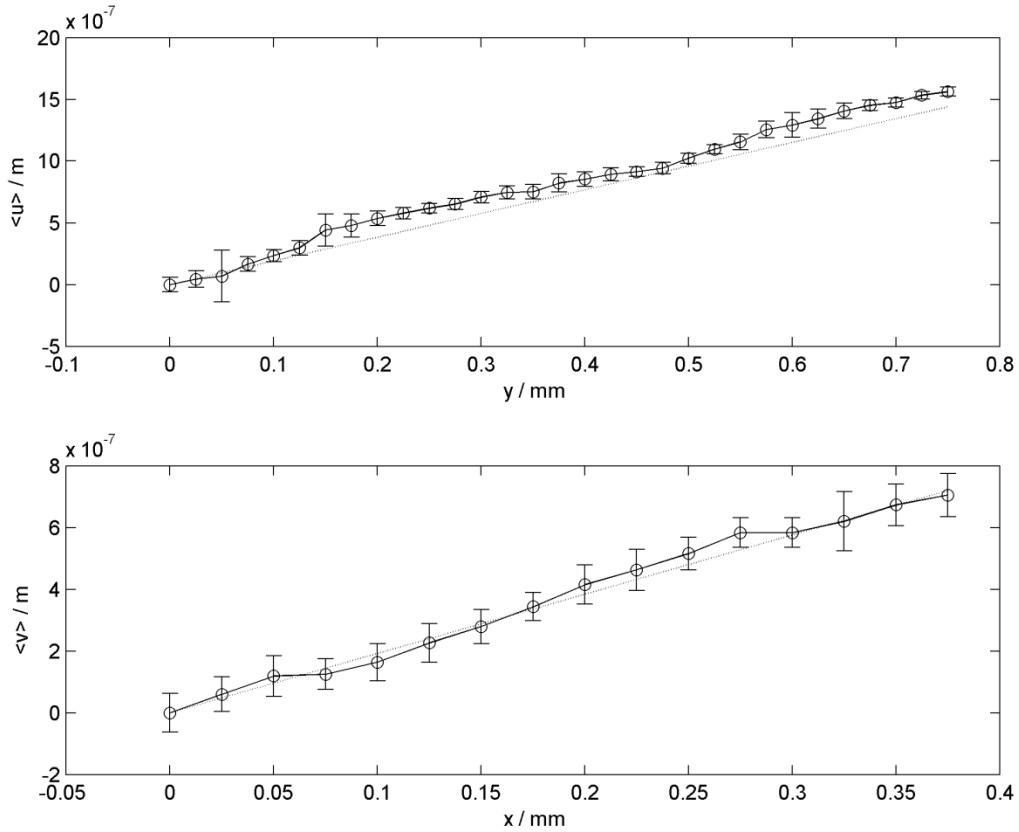
Figure 6.11 'Measured' (black line) and 'reference' (gray line) average displacement profiles obtained for in-plane rotation of the sample.

6.6.2 Out-of-plane tilt

In the $\Delta\phi_1$, $\Delta\phi_2$ and $\Delta\phi_3$ phase volumes, only $21\times64\times301$ (m, n, p) voxels for 0.027 ° tilt and $13\times36\times71$ voxels for 0.054 ° tilt were obtained without unwrapping errors. Figure 6.12 and 6.13 show cross sections of the measured 3-D displacement fields corresponding to the epoxy sample under out of plane tilt of 0.027 ° and 0.054 °, respectively. These correspond to phase difference volumes shown in 2nd and 3rd row of Fig. 6.8. The rows indicate the displacement components w along the x, y and Λ axes, respectively. From left to right, the columns show sections of the data volume on planes $y\Lambda$, $x\Lambda$ and xy, respectively.
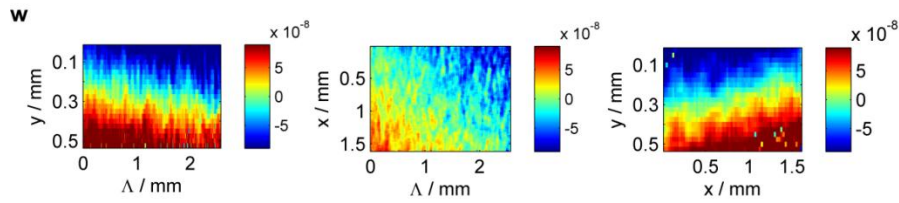
Figure 6.12 Cross sections of the measured 3-D displacement field corresponding to a sample under out-of-plane tilt (0.027°). The row indicates the displacement components *w* along the *x*, *y* and Λ axes, respectively. The columns show sections of the data volume on planes *y*Λ, *x*Λ and *xy*. Displacements units: mm.

Figure 6.13 Cross sections of the measured 3-D displacement field corresponding to a sample under out-of-plane tilt (0.054°). The row indicates the displacement components *w* along the *x*, *y* and Λ axes, respectively. The columns show sections of the data volume on planes *y*Λ, *x*Λ and *xy*. Displacements units: mm.

The gradient of the *w* displacement field corresponds to out-of-plane tilt. In order to compare the measured displacements with the known ones introduced with the tilt stages, the *w*(*x*, *y*) displacement shown in Figs. 6.12 and 6.13 were averaged along the *x*-axis and error bars representing the root mean squared deviation were also included. These results are shown in Fig. 6.14.
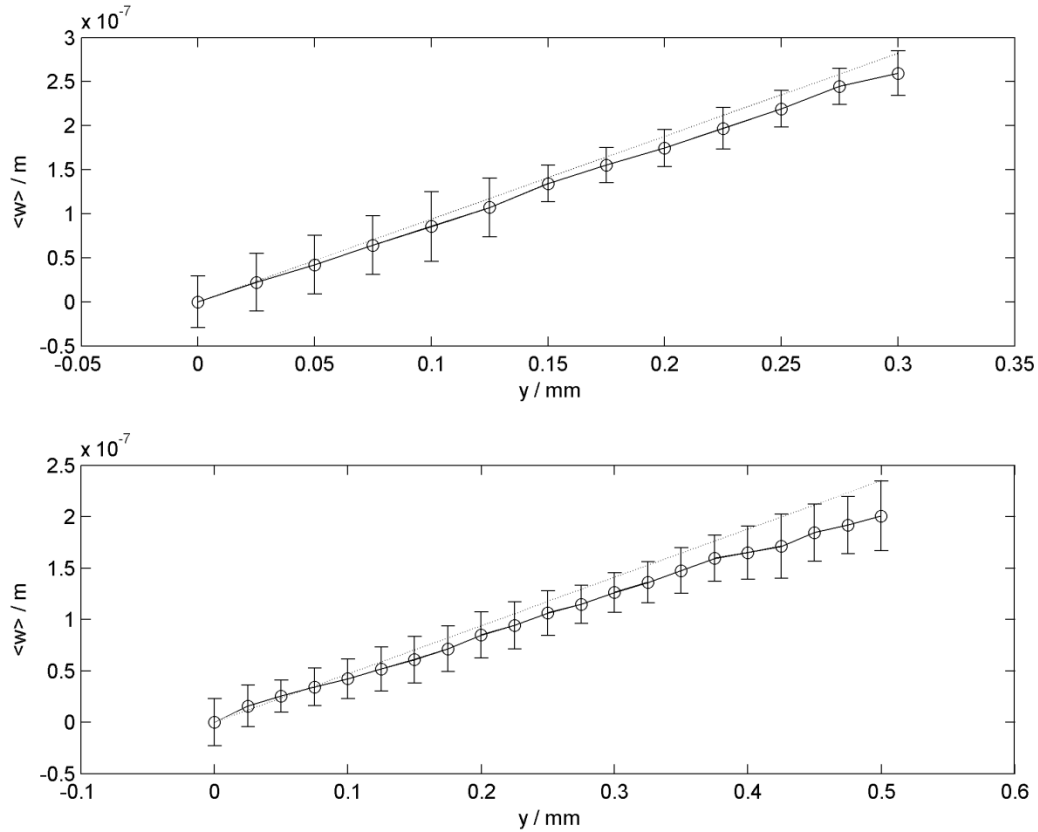
Figure 6.14 'Measured' (black line) and 'reference' (gray line) average displacement profiles obtained for out-of-plane tilt (for 0.027° and 0.054° respectively) of the sample.

The root mean squared deviation between the theoretical and measured displacements *w*(*x*, *y*, *z*), for out-of-plane tilt (for 0.027° and 0.054° respectively) were 30.12nm and 30.98nm, respectively.

6.6.3 Simultaneous in-plane and out-of-plane

For simultaneous in-plane rotation and out-of-plane tilt, 16×35×71 (*m*, *n*, *p*) voxels were obtained from the phase-difference volume data without any unwrapping errors. Figure 6.15

shows cross sections of the measured average 3-D displacement field corresponding to the epoxy sample under in-plane rotation and out of plane tilt. From top to bottom, the rows indicate the displacement components *u*, *v* and *w* along the *x*, *y* and *z* axes, respectively. From left to right, the columns show sections of the data volume on planes *y*Λ, *x*Λ and *xy*. Notice the gradient in the *u* and *v* displacement fields, as expected for an in-plane rotation around the observation direction, and the gradient of displacement *w* at the bottom right, which corresponds to out-of-plane tilt.
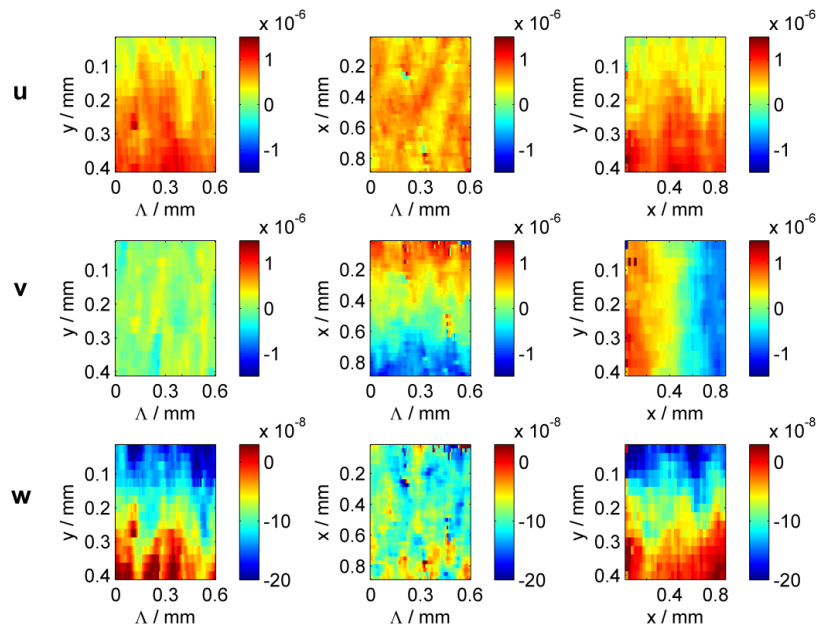
Figure 6.15 Cross sections of the measured 3-D displacement field corresponding to a sample under in-plane rotation and out of plane tilt. The rows indicate the displacement components *u*, *v* and *w* along the *x*, *y* and Λaxes, respectively. The columns show sections of the data volume on planes *y*Λ, *x*Λ and *xy*. Displacements units: mm.

In order to compare the measured displacements with the known ones introduced with the rotation and tilt stages, the $u(x, y)$, $v(x, y)$ and $w(x, y)$ displacements shown in Fig. 6.15 were averaged along the *x*, *y* and *x*-axes, respectively, and error bars representing the root mean squared deviation were also included. These results are shown in Fig. 6.16. The root mean squared deviation between the theoretical and measured displacements $u(x, y, z)$, $v(x, y, z)$ and $w(x, y, z)$ were 0.14μm, 0.20μm and 32.5nm, respectively.
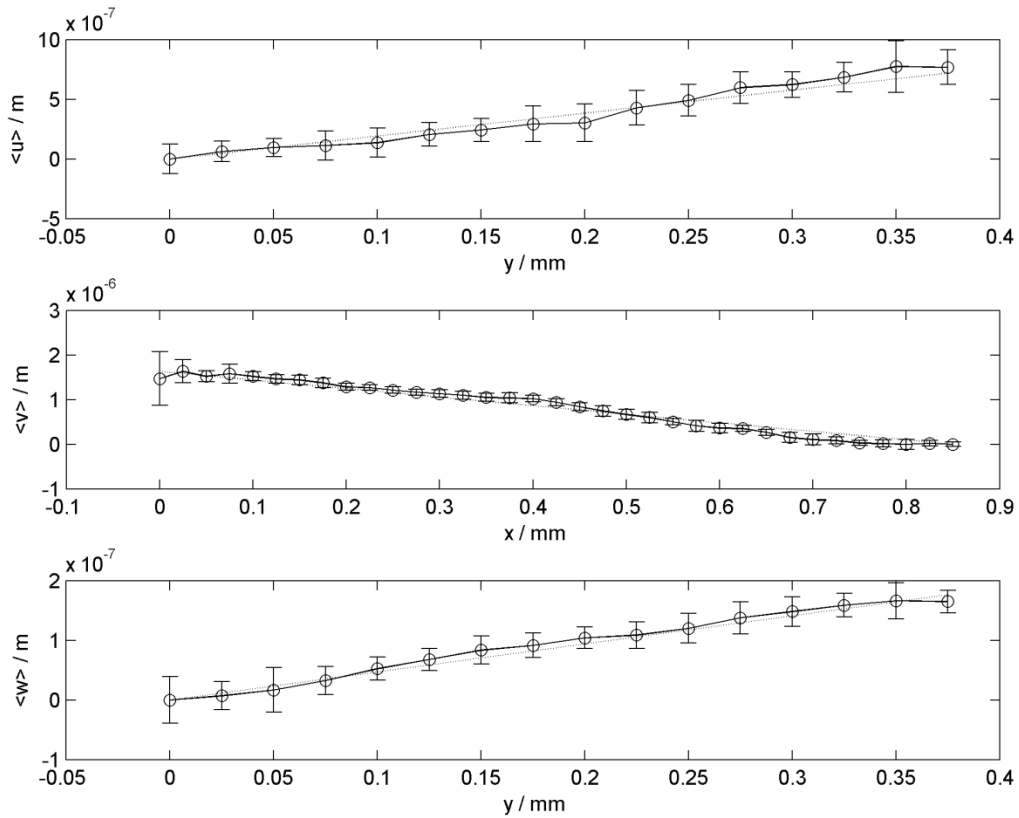
Figure 6.16 'Measured' (black line) and 'reference' (gray line) average displacement profiles obtained for simultaneous in-plane rotation and out-of-plane tilt of the sample.

6.7 Conclusion

In this chapter we described a method based on WSI to measure 3-D displacement fields within scattering materials with interferometric sensitivity. It provides 3-D reconstructions of the material microstructure and also depth-resolved phase information that was used to evaluate all the components of the displacement vector at each voxel of the data volume. This can be viewed effectively as an extension of full-sensitivity Digital speckle pattern interferometry (DSPI) into three dimensions. Alternatively the technique can be viewed as frequency multiplexed OCT in which each channel carries information for specific displacement sensitivity. Even though a robust 3-D phase unwrapping algorithm was used, where phase unwrapping errors due to large singularity loops remained. The measured 3-D displacements showed excellent agreement with the expected values obtained from known rotation as tilt angles introduced with mechanical stages.

The next Chapter summarizes the overall results and also discusses different problems encountered during the experiment, advantages and disadvantages of the technique and future plans.

Chapter 7

7 Discussion and further work

A novel method based on wavelength scanning interferometry has been proposed and demonstrated to measure 3-D displacement fields within semi-transparent scattering materials. This effectively extends full-sensitivity DSPI into three dimensions. The reconstructed microstructure of the material volume has been obtained and the depth-resolved phase difference volumes due to known displacement fields have been used to evaluate all three orthogonal components of the displacement vector at each voxel within the data volume. The technique can be viewed as frequency multiplexed OCT where multiple illumination channels carry signals for specific displacement sensitivities. The ability to measure the complete set of displacement components within the volume of the sample opens exciting opportunities in experimental mechanics, for instance the identification of constitutive parameters in anisotropic or multi-material samples. This is usually done by finite element

model updating (FEMU) or alternatively using the virtual fields method (VFM); these are two powerful inversion techniques that benefit from full field displacement or strain fields.

With no memory constraints, the current WSI interferometer could generate a raw data volume of approximately $512\times640\times N_t$ (rows, columns, frames). The maximum number of frames N_t is given by the ratio of the laser frequency tuning range to the minimum frequency step: $N_t = \Delta\nu/\delta\nu = 17.495\text{THz}/0.0002\text{THz} \sim 87,000$ frames. After re-registration, the size of the 'displacement' volumes u, v and w would be reduced to $\sim512\times640\times N_t/24$ due to the data processing required in the Fourier domain. The factor $1/24$ arises from the fact that ½ of the frequency axis (negative frequencies) is neglected, another ½ is lost due to the autocorrelation terms, then ⅓ of the remaining bandwidth is used for each sensitivity vector and finally $\sim$½ of that range is effectively used to accommodate the object thickness due to the tilt in the frequency space. Thus, the reconstructed displacement volumes would contain $\sim512\times640\times3600$ voxels. If a $7\times7\times7$ convolution kernel is used to reduce spatial noise then the displacement volumes would provide $\sim70\times90\times520$ independent measurements. The maximum 'effective' depth range can be estimated from Eqn. (3.11) by considering $\delta k = 4.19\text{m}^{-1}$ and an extra factor of $1/12$ (½ already taken into account by discarding negative frequencies) as $\Lambda_{M\_eff} = \Lambda_M/12 \sim 62\text{mm}$. The depth range in the current setup is 6.2mm, where only 8748 frames were recorded, as explained in section 5.2.1. This is assuming that multiple scattering and absorption do not set a lower limit. The sample used to evaluate the performance of the WSI system proposed in this Thesis consisted of an epoxy resin block seeded with scattering particles much smaller than the size of the volume PSF. A particles/resin volume fraction of $\sim3\times10^{-3}$ resulted in ~100 particles per PSF. If particles were sparse as required by particle image velocimetry, there would be regions in the volume that would not contribute any signal and thus no displacement information could be retrieved. On the other hand, a high volume fraction would result in multiple scattering, increasing the noise floor and reducing the depth resolution (as the point spread function broadens in the axial direction) and the maximum imaging depth of the system, as light cannot penetrate deeper into the sample.

Some issues that need to be investigated include the effects of material dispersion, birefringence, intensity noise through the optical fibre, penetration depth, surface refraction, effects of mechanical scanning within the system , other sources of mechanical vibration etc., [64] all of which may have effects in the measured displacement and strain fields. Moreover,

phase singularities can be so abundant and complex in a 3-D volume that robust 3-D phase unwrapping algorithms are required.

For a dispersive sample, the most common effect in the OCT signal reconstruction is the degradation of the axial resolution. In WSI, wavelengths of the tunable laser are incident on the sample sequentially and for each incidence, the effective wavelength within the sample reduces due to its finite refractive index (R.I.) where the R.I. is a function of wavelength in case of a dispersive material. The change amounts to the free space wavelength divided by R.I. at each wavelength. As a result, the sample dispersion introduces additional frequency dependent phase components to the Fourier transformed data, which may change the positions of the cross correlation peaks and may not locate the coordinates of the scatterers on the surface or the bulk of the material properly.

The WSI system described in this Thesis illuminates the object with polarized light. This is partially depolarized in the scattering sample and the backscattered light recombines with a polarized reference beam. As sample birefringence can alter the polarization of the backscattered light, it may lead to a reduced interference modulation and thus reduced signal to noise ratio.

Intensity modulation due to fibre polarization effects can be observed in all interferometric setups using optical fibres, and care must be taken to minimize these, e.g. by using polarization preserving fibres and maintaining the fibres in a stable environment during image acquisition.

The penetration depth inside the sample depends on factors like: 1) wavelength of the light incident upon it, 2) sample spectral absorption, and 3) sample scattering. Different experiments proved that near-infrared light penetrates more inside tissues and common polymers than visible light. Strong spectral absorption in the range of the tunable laser emission will lead to reduced backscattered light, and thus to low signal to noise ratio. The effect of scattering has been discussed above.

In all depth resolved tomographic imaging techniques, refraction distortion at all interfaces between different regions having different refractive indices must be determined and

corrected for accurate dimensional characterization [132]. Even though these methods were limited to 2-D processing of cross-sectional images, 3-D curved structures such as the convex surface of the cornea, the concave surface of a hollow organ or a tract can also be corrected for refraction distortion by applying 3-D algorithms. The 2-D refraction correction is only possible in case of 3-D curved surfaces if the sample is rotationally symmetric about an axis passing through the apex of the sample. If left uncorrected, refraction distortion will lead to phase errors and thus spurious displacements and strain. The WSI system proposed in this Thesis is free from any mechanical scanning devices, which in OCT systems are responsible for certain geometric distortions.

Phase unwrapping is the last and usually challenging step for extracting phase information in fringe analysis. In this Thesis, a phase unwrapping algorithm based on setting surface patches onto phase singularity loops has been used [129-131, 133, 134]. Jenkinson *et al* [135] in 2002 presented another approach of 3-D phase unwrapping algorithm based on the minimization of a cost function that leads to an integer programming problem: a mathematical optimization algorithm in which all variables are integers. This approach is very fast but does not guarantee the best optimal solution. This method was applied in 3-D MRI data for venogram studies in fMRI. Improvements in 3-D phase unwrapping will enable the full utilization of the measured data-volume, thus increasing the field of view.

The proposed WSI system is able to measure 3-D displacement components in the order of a few microns with uncertainties around some tens of nanometres, in all voxels in the data volume. The high sensitivity of the technique implies that it is suitable for measuring small deformations produced, for instance, in rigid materials subjected to mechanical or thermal loads. Large displacements will eventually produce too many fringes and decorrelate the speckle, in which case speckle tracking methods would become more appropriate (up to strain levels of ~1%).

Regarding the performance of the proposed WSI system with existing single channel OCE systems, perhaps the fundamental advantage of the former is that due to the multiple illumination directions, all the components of the displacement field can be measured. OCT elastography has so far been limited to the measurement of the axial component of the displacement field. This is certainly a big limitation when all the components of the strain tensor are required, e.g. to characterize a non-isotropic materials.

Fibre glass composite materials, polymers and adhesives all seem good target materials to study their mechanical behaviour with the technique proposed in this Thesis. Epoxy resins have found diverse applications due to their excellent properties [136,137] as electrical insulators, microelectronics encapsulants, matrix for fibre reinforced materials and structural adhesives, to name a few. Measurement of localized hygroscopic expansion, thermal behaviour, internal damage evolution and structural integrity of these materials seem all plausible fields for further research.

Appendices

A1 Setting up the camera from Goodrich Corporation

Camera :

8000-0324, Rev 1

SU640SDV-1.7RT/RS170-GO22A11V0

S/N *0809S9992 *

Pixel freq ~ 43,956 MHz

Strobe freq~ 11,000 MHz

The camera was first set in an operating platform including lens, power supply, and video cables which was attached to a video monitor (PAL standard). The Video Out port of the camera was set normally active and displayed what the camera sends out via Camera Link. The digital frame grabber card from National Instruments was able to coordinate the digital

shipping between camera and the frame grabber card and the ICD file contained all of the relevant camera parameter information.

Frame grabber:

The NI-1428 card is used for standard desktop computers with a PCI bus. The 1427 card can be used for desktop computers with an available PCI-Express bus. The ICD file is associated with the National Instruments (NI) environment known as IMAQ, which are their software drivers for the frame grabber. MAX, a NI software, gives access through the ICD file and NI Camera Link card to the camera. SUI-IA is an example of application software built in MAX.The SUI-IA is an application software developed in IMAQ / MAX (part of the NI Camera Link software suite) which works only with the NI Camera Link card, using the DLLs of the provided / installed NI software. Anything done in SUI-IA can be done in the base NI software without the Sensors Unlimited elements. Thus the basic NI Camera Link interface software (MAX, IMAQ) plus the SUI-IA software plus the supplied ICD file is all that is necessary to interface to the camera and get live data. The version of SUI IA 4.0.1 incorporates a terminal window, permitting the entry of camera commands and display of their results. This is under the Camera Setup tab.The Camera Link Terminal is another program that provides a screen where users can enter camera commands and see the camera response, even while MAX program is connected to the board. This gives a great diagnostic power as one can see what the camera setting is to understand whether a software command has been received or not.

While using NI-1428 card, the operation becomes straight-forward, even if somewhat specific to the frame grabber card and its software (as the digital signal is sent according to standards, the software becomes a function of the frame grabber card, except for the optional serial camera setting commands as per SUI manual).There are a number of Camera Link vendors in the open market, but SUI has chosen National Instruments to offer integration support. Other vendors, such as Matrox has Camera Link interfaces (Matrox Intelicam 8.0 Build 1230 and MIL 8.0 (2005)) which had been already proven to work with this camera. SUI builds cameras with a Camera Link interface, and Matrox builds Camera Link frame grabber interfaces to the computer which has the ultimate responsibility to display the data in the proper environment.

Most Camera Link vendor-sourced software has a 'wizard' of sorts that allow a user to make his/her own interface file. The SU640SDV is a 640 ×512 pixel array with 14 bits resolution, single-output, base level Camera Link with Baud Rate 57600 and a clock frequency of 40 MHz. In the Horizontal it is expected to have 32 "pre" and 2 "post" blank pixels and in the Vertical it is expected to have 0 "Pre" and 2 "Post" pixels.

Different Camera Link interface softwares that allow to adjust the pre- and post- pixels interactively, using the following method:

If a distorted but live image has been shown on starting and relative black and white levels change appear when an user put his/her hand in front of the lens, the horizontal 'pre' value (one) should be incremented by one until the image becomes square and looks good, except for black bands right or left, and probably black bands or a roll in the image top to bottom. Once the image looks good as above, the horizontal black band should be removed by moving one pixel at a time from Pre to Post, i.e. if one starts with a good image at 42 pre and 0 post, the next step is 41 pre and 1 post, so that 41 + 1 = the originally found 42. The image will shift with this effort. Shifting should be carried out until getting the proper image. Next step can be performed in the same way for the vertical. If only a quarter of the image has been got (i.e. half of the horizontal line, half of the vertical extent = first quarter of the array), a Camera Link value described as DVAL (or possibly Data Valid and similar) should be toggled to its opposite: If it is Off, it needs to be turned On. If it at 1, it should be made 0, assuming these are valid commands specific to the board and if this does not fix the image, the parameters should be reset. The timing diagram should also be checked according to the manual. A stretched image can be seen when the Data Valid (DVAL is what it normally is called) signal is not properly set. The Camera Link card runs at maximum frequency and the camera is running at a slower rate, so the data points are duplicated a number of times (often times it is a factor of 4). In other words, it could be said that the stretching of the image is because the frame grabber is sampling the data incorrectly. This is sometimes because the frame grabber is trying to acquire data at the camera strobe frequency of 44 MHz. The pixel frequency is 11MHz, so the frame grabber sampling range should be cut by a factor of 4, or if sampling 11MHz at 44MHz the frame grabber should only consider 1 in 4 pixels as valid.

The Camera Link cable (Base mode i.e. 187676-02) is a standard item. The SD (SDV) camera series uses an MDR connector, and the NI card uses an MDR connector as well (the terminations are identical on an MDR-MDR camera link cable).

Triggering:

With the triggering to the Camera Link card, basically the camera is running at video rates, and the trigger tells the NI software to perform an operation, normally to save a certain amount of data and the camera knows nothing about any triggers sent. Triggering the camera allows users to make the camera respond to the signal or to synchronize any other instrument with the camera. There are 3 modes of external triggering. Trigger mode 1 allows users to control when the camera starts the exposure, and the end of the exposure is set by the stored EXP value, either from the OPR setting or specifically entered by users. Trigger mode 2 allows to control the start and the end of the recording by the length of the 'trigger active' pulse. This takes care of setting the exposure time. Trigger mode 3 controls when the camera will send data down the Camera Link interface. Essentially, the Camera Link card will be waiting for signal, and on the trigger held high (/low, user-configurable), data will be shipped until it is stopped by the trigger transition. Setting the exposure time is performed with the EXP command and the Frame Period commands. The CORRECTION commands should not be used as the corrections are only valid for the given parameters of an OPR setting, and changing the exposure time will make the corrections invalid. Users can write their own acquisition routine to acquire a set of number of frames for each trigger. In this case, the camera should be kept in free run condition and the trigger signal can be used to trigger the software to store the next *N* frames after the event trigger appears. There would be no need to freeze the camera between events.

To avoid missing any frames, the video recorder must be set to acquire all of its frames into RAM (In Applications Preferences menu under Setup the option "Stream to Disk" is not checked).

Important commands:

There is a general time out and a time out for each command. The default is for 5 seconds for the acquisition: Frame Timeout (5000). In the NI-IMAQ environment, the ICD file contains a default and current setting for all of the parameters. When the GRAB or SNAP buttons are

used, these settings are sent to the camera. Therefore, they will override any camera settings. NI-IMAM loads the parameters from the file on disk at the start of the session, or when there is a timeout, therefore, when some changes are made in the MAX, those should be saved in the ICD file. By pressing 'reset to default values' the user allows the software to load the default settings stored in the ICD file on disk, over-writing any changes he/she may have tried to make. The frame period of the camera, in the default case, is locked to the RS-170 video rate of 30 frames per second. The FRAME:PERIOD is for setting the camera timing in free run mode (TRIG:MODE 0); it does not know or have any way of reporting the trigger rate in those modes. Similarly, it is the same for the EXP command, in case of TRIG:MODE 2.

OPR is a camera command that is sent directly to the camera via the serial interface inside Camera Link. The OPR command can be sent via a program, or one can type it in manually via a serial access tool (SUI-IA has such an example on the second tab in the Camera Attributes dialog box). Each OPR has a known exposure time, frame time, dark correction, and white correction associated with it. Via the OPR settings, it is easy to move through the cameras dynamic range capability with corrected results. Sample OPR commands are 'OPR 1', 'OPR 7', OPR 15'. Users can also define their own OPR setting based on their unique needs.

Most of the user interface software is set up for continuous or multi-frame acquisition and the images may normally take a couple of cycles to be displayed. The camera does not have any memory. The acquired image is integrated onto the Focal plane array (FPA) and then digitized and readout over the camera link interface pixel by pixel. It is up to the frame grabber and the controlling software to store the image and display it. SUI Image Analysis software has the capability to save images in several formats. The simplest and smallest format for transferring to MATLAB is with the extension .IMG - this creates a file where the first bytes give the column and row size using ASCII characters, followed by a carriage return character. Then the pixel data is given in sequence, with 16-bit binary values. In MATLAB, the whole file is generally read in bytes, where the first 7 bytes representing the ASCII characters are stripped off and then the rest is stored in the 2-D image memory array. The .IMC version has 9 lines of ASCII text and then the raw data follows with the image. The .PNG image format is 16 bit uncompressed format which is more universal. It is an open source type of format that doesn't need a license. The .TIF file has many options and seems not so universal. It is also a 16-bit and lossless format.

To increase the exposure time beyond the standard for this 30 fps camera, there are two ways. The first does not need an new OPR: In Trigger mode 2, the external trigger signal controls both the start but also the end of integration by the width of the trigger signal. By default for the SDV camera the SCAN:VIDSYNC has to be ON, but that limits the frame period to $1/30^{th}$ of a second. By turning it off, the frame period can be set to longer times, thus permitting the exposure time to be increased. A convenient command to use would be EXP:MAXRATE, which will automatically increase the frame period appropriately. Once the value has been settled a new OPR has to be invoked and the OPR:SAVE command should be issued. For a new setting, at the time of startup, the OPR:START command can be issued with the new OPR # and then the CONFIG:SAVE can be used to make the current settings the power on condition. Everything should be done in TRIG:MODE 0 before saving. In either case, the factory non-uniformity corrections will not be appropriate with this longer exposure time and the image dynamic range may be squeezed by dark current filling the full well, causing non-linear effects. Unlocking the acquisition from the analog video to go slower will result in the video showing the same frame of data several times until the new frame is available. In the double buffer video display mode the analog video will show complete frames of data from the same acquisition but there will be more delay.

The dark current of the camera increases with long exposure times. If the pulse is short the net number of photons is low, and increment of the dark level plus the dark noise from that larger level followed by the longer exposure time will hurt the goal of capturing a weak signal. Increasing the exposure time is more appropriate when the flow of photons is continuous and the signal to build up to be bigger than the read noise of a single acquisition.

For MATLAB usage, the TXT option or the most compact format IMG type store a header with just seven ASCII characters: "512,640" followed by a carriage return line feed pair, then the image data as a stream of 16 bit words. MATLAB can be set to read the file, strip off the text before the first carriage return, or read it in as row and pixel counters for nested loops that put the words into a 16-bit integer array of the same dimensions.

Steps to change the exposure time:

1) VIDSYNC is a global command. It has to be set once per session / change the power up state with the CONFIG:SAVE command.

2) The purpose of EXP:MAXRATE is to automatically set FRAME:PERIOD at the appropriate value that allows for the overhead needed in addition to the the exposure time. This is a fixed amount. If VIDSYNC is enabled, the value for FRAME:PERIOD will not change.

3) For OPR:DEL ALL, any user created OPRs are deleted

4) For OPR:SAVE, a new OPR is created, at the next available number. If the current number is 7, then the next is 8.

5) Once an OPR has been created, such as 8, and it is the current operating OPR, then for changing the EXP, the OPR:UPDATE needs to be used to alter the stored settings for OPR 8.

6) If EXP big# is issued and it exceeds the current (frame period − overhead) value, it will show an error. Thus FRAME:PERIOD has to be increased first and then EXP in that case to avoid an error.

7) First use SCAN:STATE OFF and then making of some changes can generate an error, whereas SCAN:STATE ON and making of changes can minimize the prospect of the error message. However for increasing the exposure time, just turning off VIDSYNC and then using EXP:MAXRATE should be sufficient.

8) The inquiry commands can be used to ensure that the commands have done what an user asked for, e.g. the FRAME:PERIOD? command.

9) Before starting the acquisition and to see that the frame rate has not changed, a FRAME:PERIOD? commandor OPR? command can be issued.

10) As the pixel clock period is 91 ns, 123 µs represents 1352 clock cycles. This is the difference between the value to set the exposure clock cycles in the EXP:MAXRATE command, such as the first example is below of 1098830 and the resulting frame period value of 1100182. This overhead time between the exposure time and the frame period must be allowed.

11) If the output is viewed from the VIDEO OUT BNC while OUTPUT:SYNC is enabled, it would be confirmed that the commands were indeed changing the camera timing to provide the exposure period and frame period as selected.

If the frame rate is to be set exactly at 10 Hz and the frame period to be at 100 ms (as near as the integer number of clock cycles will allow), the FRAME:PERIOD should be programmed as 1098909. For this frame period, the longest exposure clock time can be programmed as the number less 1352, or 1097557. The actual exposure time will be (1097557 + 28)*91 ns

or 0.099880235 seconds. If, on the other hand, the exposure time has to be set exactly at 100 ms, then an exposure time is used in clock cycles of 0.1/91 ns = 1098901, then 28 has to be subtracted to get the value in exposure cycles to program into the EXP command: 1098873. (Again, the integer value limits the accuracy, but the crystal controlled clock is a nominal value and has a stability of +/-25 ppm)

The InGaAs is not as uniform as Silicon. For this camera, a good pixel is one that stays within +/-35% of the mean. This means, that when the mean intensity across the array is 12300 counts, that some good pixels could be reaching full scale of 16383. When pixels exceed the limits of the ADC, data is lost.

Example : For 50 ms frame period, simply divide 91 ns into that time to get the number of clock cycles to program, which is 549451 (rounding up).

A2 Table 1 Measurement of displacement fields in the volume of materials

Technique	Materials	Volume size / voxel size (mm^3)	Time per voxel (s)	Displacement resolution or uncertainty / strain resolution	Spatial resolution	Comments	Reference
ND & synchrotron XRD	Polycrystalline engineering materials, metals	Volume-20mm^3 for ND and 0.11mm^3 for synchrotron XRD	Tens of minutes for ND and seconds to minutes for for synchrotron XRD (for moderate sample of depth & resolution 1mm^3)	10^{-4} strain resolution	Can be improved to 0.5mm	Both can provide line scan, area scan and **3D** maps of residual strain non-destructively during complex environment such as. fatigue loading and temperature.	[19]
XRD	Crystalline nano-materials, quantum dots, tissues	100nm or less grain size	100-nm crystal in 100 ps (seconds to minutes)	Phase shift +1.4 rad corresponds to displacement 0.08 nm.	40 nm	It is an in-situ measurement technique within nano-materials under different extreme working environment.	[24,25]

XmCT&DVC	Soft and hard epoxy (breast mimicking tissues)	Volume-59×60×45 mm^3 / voxel size-100×100×100 µm^3.	Computation time depends on optimal sib-image size of the correlation process of the elastography.	Displacement uncertainties at 4 different regions-4.0±5.2, _4.0±8.4, and 0.0±8.2 µm Average strain -0.36+0.33 % at hard inclusion	100µm	Method is elastography with 3D X-ay imaging, used to measure the strain of malignant tissues, basically the stiffness, can calculate the displacement and strain only within region of high intensity pattern.	[41]
	Fatigue crack in cast iron	Sample volume-1.6×1.6mm^2 area and 4mm thick. Reconstructed image-340×340×512 voxels, voxel size of 5.06µm ~ 1.72×1.72×2.59 _ mm^3. Volume of ROI : 288×288×288 voxels (1.46×1.46 ×1.46 mm^3)	Total 42min (3sec for each image)	Stress intensity factors 130 µm to 1590 µm	~3µm (depends on detector)	Method comprises in-situ XmCT, filtered back-projection algorithm with C8-DVC and X-FEM simulation has been used to get actual crack shape. Young's modulus of the sample=175 Gpa, yield stress=315 Mpa, Poisson's ratio = 0.3.	[42]
	Cubic silicon sample	Volume-2000 ×2000 × 1150 voxels, resolution 10µm	Averaging 20 images, at 900 steps took 110 min at 10 µm resolution.	u= −0.084 ± 0.221, v = −0.572 ± 0.220,and w = −1.157 ± 0.175.(3-D displacement standard dev. Error)	10µm	New DVC method is developed, can solve 20-degree-of-freedom-problem, can compute very large size.	[43]
	Cancellous bone	Volume-520×520×580 voxels (each voxel-35µm^3)		Standard deviation in the displacement and strain components are 0.005 voxel spaces and 69µstrain.	43.75µm (FEM model)	Displacement results obtained from both DVC and FEM methods for higher density femoral bone were almost similar.	[44]
	Duocel open-cell Al foam with trabecular bone like structure(2 cubic samples)	ROI: 17×17×17voxels .	40 s (using 800MHz personal computer)	Standard deviation in displacement and strain components are 2.0µm and 0.01 respectively.	36µm	The Green Lagrange strain components are determined here.	[45]

	Bovine distal femur, bovine proximal tibia, rabbit distal femur, rabbit proximal tibia, rabbit vertebra, and human vertebra	4 sub-volumes are selected: 20×20×20, 30×30×30, 40×40×40, and 50×50×50 voxels[3], each voxel~36μm	300 ms integration time	Displacement and strain errors-1.86–3.39 mm (0.052–0.094 voxels) and 345–794 μstrain respectively for all bone types for 40voxels[3] sub region.	36μm	Analyses were performed on images of undeformed samples; thus, strain could not be calculated and the phantom structures were not consisted with the specific bone structure , which include large errors.	[46]
	Wood specimen made out of Scots pine (Pinussylvestris).	Volume-1.57×3.42×0.75 mm[3] Reconstructed volume-3.58 ×3.58× _ 1.22 mm[3] and the isotropic voxel dimension 1.75× 1.75×1.75μm[3].	The exposure time was 300 ms and total scan time was approximately 12 min /10 min	Displacements u,v,w along x, y, z directions and strain values were plotted. (w=6.2μm, v=2.6mm)	2.15μm	Different displacements and strain data from two selected regions of different shape, spatial scale and geometrical location have been plotted- both in 2D, 3D.	[47]
	Micro-cracks in murine cortical bone	Volume of interest(VOI) containing micro crack of 400 × 400 × 400 voxels	Not specified	Displacement and strain error 130 nm and 0.013 Displacement accuracy = 0.0006 voxels (0.4 nm) and the precision was 0.176 voxels (130 nm) and strain precision was 0.011 and 0.013.	10μm	Strain resolution of 13.5 voxels (10 μm) and displacement resolution of 13.7 voxels (10.1 μm)	[48]
	Cylindrical bed of sugar	Reconstructed dimensions 7.98 × 7.98 × 8.87 mm[3], during correlation sub volume is 0.753 mm[3](323 voxels).	545 projections distributed at equal angles over 360◦ exposure time/projection 2.56 sec	Border region have a displacement ~20 μm (less than at centre). Towards top of of cylinder, difference increases to ~ 40 μm.	Detector's spatial resolution is 4.5 line pairs/mm (line pairs per mm)	In the result, expected features of granular compaction were observed	[49]

	Polypropylene solid foam	2048 ×2048 × 2200 voxels, per voxel 4.91 µm	For ROI size of 10voxels and element size of 8 voxels, computation time is 10min and for ROI size 176 and element size 16 voxels, time required 1 hour.	For element size 16, displacements are -2.28, -0.77, -2.99 voxels along x, y, z directions, displacement uncertainty o.o1 voxel or 0.197 micron		It is a new approach for finding 3-D displacement by comparing two CT scans.	[50]
	Rock	Reconstructed slice is 14 ×14 ×14 micron^3. 925×925×1325 voxels	15 min	Strain is 20 voxels or 280 µm	14×14×14µm^3	Images represent only the local changes due to deformation only.	[51]
Optical scanning tomography (OST)& DVC	Liquid resins like silicone (transparent)	300×850×140 voxels^3,voxel size 60 µm.	Not specified	Displacement uncertainty 0.037 voxels	0.06mm/voxel	OST presents better structural studies on transparent models with polymer particles.	[52]
DVC by optical slicing	Epoxy resin (high Young's modulus) and Polyurethane (lower modulus) blended with silica powder, silver hollow glass sphere, polyamide powder, polymer micro balloons	Volume of 300×850×140 voxels and correlation subset (31×31 ×31 voxels^3)	Time consuming method (not specified)	Displacement uncertainty x,y and z are 0.015voxel (0.9 micron) and 0.058 Voxel (3.5 micron). Strain uncertainty 0.00075 and 0.0029 respectively.	60 µm /voxel	Standard deviation in displacement 0.0009mm in x any directions and 0.0035mm in z.	[53,54]
3-D US with DVC	Breast mimicking tissue by soft and hard gels	3-D image has the size of 431×231×500 voxels and tracking points are chosen within 36 × 18 × 47 voxels	Not specified	Calculated elastic modulus in 3D for (1% strain)E $_{inclusion}$/E $_{outer}$ is 2.12 and inclusion diameter is 10.9 mm.	Space resolution of 82.5 µm/pixel	2-D and 3-D displacement and strain fields are measured and strain fields are improved using smoothing algorithm.	[57]
USI and 3-D estimator	Polyvinyl alcohol cryogel pressure ulcer mimicking	Phantom volume (30 mm × 60 mm × 110 mm)	For 1 section of the elastograms, standard PC with 2.6	3-D estimator is based on mean value of normalized	Lateral and azimuthal resolutions are much coarser than axial	Optimized adaptive and iterative process estimates the axial	[55,56]

	phantom		GHz CPU and 1 Gb RAM took 1 hour (Matlab coding).	correlation coefficient of 0.93. For 2% deformation 0.6mm displacement can be measured.	(not specified)	strain distribution during lateral and azimuthal motion.	
Laser scanning confocal microscopy with DVC	Transparent agarose gel sample embedded with fluorescent markers	512×512×512 voxels, i.e. 230×230×230 µm^3, DVC sub volume 64×64×64 voxels (2 voxels~1µm)	Tens of minutes	Under uniaxial compression and without stretch correlation, lateral strains are 0.8×10^{-2}, 1.1×10^{-2},and axial strain is -9.25×10^{-2}, without stretch correlation lateral strains are-3.6×10^{-2},-7.8×10^{-2}, and axial strain is-9.34×10^{-2}.	Lateral resolution is 3-10 times better than axial resolution, which can be determined by 3-D point spread function.	Under large deformation, the stretch correlation and deconvolution algorithm improves strain measurement accuracy.	[59]
	Same	DVC sub volume 30×30×30 and searching volume 70×70× 70	Tens of minutes	Mean error for 5% compression, lateral strain 1.3×10^{-3} and axial strain3.4×10^{-3} and mean displacement error 0.0767 voxels (3-D gradient based algorithm) and 0.0216 voxels (3-D Newton-Raphson iterative method)		It provides a set of DVC algorithm for 3-D deformation measurement. Homogeneous vertical displacement fields are measured in sub volume 30×30×30 and searching volume 70×70× 70 regions by DVC.	[60]
	Migrating fibroblast on the surface of FN modified polycrylamide gel	The cell is imaged within a field of view 150×150×150 µm^3	35 min to 140 min depending on the thickness of the sample	Displacement resolution >0.12 µm (decreases from 67% to 23% with increasing thickness.	¬2 micron	Traction forces during malignant transformation, force profile and effects of soluble factors can be evaluated.	[61]

OST with DVC	Plane bearing model in epoxy resin, embedded with polyamide particles of 150μm	DVC performed on 31×31×31 voxels, step volume of 20 voxels between two subset volumes	Not specified	Displacement uncertainty is 0.1 voxel ~ 0.006 mm, strain value ~ 0.005.	Spatial resolution of volume image ~ 0.06 mm/voxel	Mechanical response of aeronautical plane bearing has been studied.	[73]
OCT+2D speckle de-correlation	Gelatin model, pork meat, human skin	5×5×7 μm^3 gelatin volume with 0.2 -6.0 μm dia polystyrene latex sphere distribution, 3×3×2 mm^3 gelatin model with cynoacrylic glue, 1×1×0.3 cm^3 pork meat, 2mm thick surface of bone of backside of male index finger.	70 sec for 0.8 mm lateral scan.	20 μm displacement for gelatin model, 10-16 μm axial displacements with 0.2-0.6 μm rms deviation for pork meat, axial and lateral displacements 13.7 μm(with a standard deviation of 0.45 μm) and 2.2 μm (with a standard deviation of 0.44 μm) respectively for finger skin.	¬ few micron (not specified)	This technique could make the distinction between different stages of strain distribution over time, associated with cell profileration and matrix deposition in engineered and natural tissues.	[66]
3-D OCE	Hydrated and normal finger skin	Image size ¬ 2 mm × 1 mm × 1 mm	Acquisition time ¬ 5 min	Contrast ratio (ratio of strain rate magnitude) between stratum corneum and epidermis is ~ 0-1.8 for 0-2.5 N applied preload.	¬ 15 micron	3-D OCE system, processed in 2-D and displayed in 3-D for in vivo hydrated human skin.	[74]
3-D micro MRI with FE based 3-D correlation	Cancellous boan from bovine femoral head	Volume size: 40mm20mm× 20mm Voxel size:96×192×96 voxels (or7.5mm×15mm×7.5mm).	Scan time 9 hour	For correlation element of 12 voxels, the displacement value along x is – 4.68 voxels, along y-9.82 voxels, along z -6.62 voxels and strain valu-0.6.	Isotropic resolution of 78micron per voxel	3-D displacement fields of sub-voxel uncertainty <0.1voxel (8 mm) fore element sizes >12 voxels.	[26]
MRI with 3-D texture analysis	Composite intervertebral disc tissue	256× 256× 64 voxels 78μm voxel size	12 msec	Axial strain -9.55% ± 2.59% and -9.07% ± 2.71% for two different slices and	In-plane resolution 98micron for meniscal sample and 234 micron for	1st order texture correlation can accurately measure strain distribution of	[27]

				radial strain 0.17% ± 0.83% and -0.14% ± 0.52% for those two slices.	intervertebral disc.	MRI images under large deformation.	
DENSE MRI with Virtual fields method	Phantom made by Semicosil 921 silicone gel	Sample volume: 80×64×154 mm^3 50×50×42 mm^3 ROI is unwrapped	¬6 hours	Average value of modulus in surrounding material is 0.69 and in inclusion is 2.98. Thus the ratio between both modulus values is 4.3.	Not specified	This is the first extension of VFM to the 3-D bulk full field measurement, So assumptions are the limitations, such as, stable Poisson's ratio, loading, quasistatically, linear elastic behaviour.	[29]
Tomographic PIV with DVC	Motion of the particles around a ring vortex	35 × 35 × 7 mm^3 reconstructed volume ~ 700 ×700 × 140 voxels	Not specified	For 3-D cross correlation, interrogation volume ~41^3 voxels absolute error < 0.10 voxels in u and v and < 0.16 voxels in w.	Not specified	This is a lens less tomographic HPIV.	[38]
DHM with PTV correlation	RBC in a circular micro-tube flow	600 μm×350 μm ×350 μm measurement volume with 185 RBCs	Interval between consecutive frames ¬ 2ms, exposure time 10μsec/ frame., computation times are different for 5 different focus functions.	Maximum velocity ~ 5.96mm/s and mean velocity ~ 2:98mm/s,	0.6 micron	RMS velocity in x direction has fluctuation o.305mm/s with o.63micron error, in y direction 0.253mm/s with 0.52micron error and in z direction 0.996mm/s with 2.05micron error.	[39]
Tomographic polarimeter	Epoxy resin cubic sample	Volume ¬ 25mm x 25mm x 25mm	4.5 hours	The characteristic retardation is plotted against no of pixels through a particular line of 36 images (10º intervals of the polarizer) and for 72 images (5º intervals of the	Rotational stage provides the resolution of 0.001 degree.	A Fourier polarimeter is developed, characterising photoelastic parameters of the sample.	[78]

				polarizer) and then compared the noise level.			
PSOCT	Polymer sample	B-scans with 1000 x 512 pixels	Not specified	Retardation values are plotted	1st PS-OCT working at 1550nm range gives depth resolution ¬15micron and 2nd system provides ¬2micron at 800nm for a polymer sample.	It is a reflection mode PS-OCT, measures birefringence in the perpendicular plane of the depth axis	[76]
Tissue Doppler OCT with 2-D correlation	Tissue phantom made by polyvinyl alcohol	B scan with 1.2×2.5 mm^2 with 500 A scans	Time consuming method, camera integration time 34.1µsec, read-out time of OCT 5 sec.	The strain from bottom to top layers ~ 1.65±0.10, minimum resolvable displacement of tissue ~ 0.15 nm and the velocity of the tissue 9.5mm/sec	Axial and lateral resolutions of 8 and 20 µm respectively	Two different types of speckle tracking methods are presented here, one for small and the other for fast and large speckle motion.	[68]

References

1. Ambu, R., et al., Assessment of NDT interferometric techniques for impact damage detection in composite laminates. Composites Science and Technology, 2006, 66(2): p. 199-205.

2. Amaro, A. M., Reis, P. N. B., de Moura, M. F. S. F., Santos, J. B., Damage detection on laminated composite materials using several NDT techniques. Insight-Non-Destructive Testing and Condition Monitoring, 2012, 54(1): p. 14-20(7), (Publisher:The British Institute of Non-Destructive Testing)

3. Rippert, L., Wevers, M., and Huffel, S. V., Optical and acoustic damage detection in laminated CFRP composite materials. Composites Science and Technology, 2000, 60: p. 2713-2724.

4. Awaja, F., et al., The investigation of inner structural damage of UV and heat degraded polymer composites using X-ray micro CT. Composites Part A: Applied Science and Manufacturing, 2011, 42(4): p. 408-418.

5. Zhou, Y., Wildman, R. D., and Huntley, J. M., Measurement of the mechanical properties of granular packs by wavelength-scanning interferometry. Proceedings of the Royal Society A: Mathematical, Physical and Engineering Sciences, 2009, 466(2115): p. 789-808.

6. Avril, S., et al., Overview of Identification Methods of Mechanical Parameters Based on Full-field Measurements. Experimental Mechanics, 2008, 48(4): p. 381-402.

7. Avril, S. and Pierron, F., General framework for the identification of constitutive parameters from full-field measurements in linear elasticity. International Journal of Solids and Structures, 2007, 44(14-15): p. 4978-5002.

8. Grediac, M., et al., The Virtual Fields Method for Extracting Constitutive Parameters From Full-Field Measurements : a Review. Strain, 2006, 42: p. 233-253.

9. Ruiz, P. D., et al., Depth-resolved whole field displacement measurement using wavelength scanning interferometry. J. Opt. A: Pure Applied Optics, 2004, 6: p. 679-683.

10. Ruiz, P. D., Huntley, J. M., and Maranon, A., Tilt scanning interferometry: a novel technique for mapping structure and three-dimensional displacement fields within

optically scattering media. Proceedings of the Royal Society A: Mathematical, Physical and Engineering Sciences, 2006, 462(2072): p. 2481-2502.

11. De la Torre-Ibarra, M. H., Ruiz, P. D., Huntley. J. M., Double-shot depth-resolved displacement field measurement using phase-contrast spectral optical coherence tomography. Optics Express, 2006, 14(21): p. 9643-56.

12. Vaz, M. A. P., Optical methods in experimental mechanics. Paper Ref: P0004_A0584 (Invited Plenary Paper) 3rd International Conference on Integrity, Reliability and Failure, Porto/Portugal, 20-24 July, 2009: p. 1-2.

13. Optical Methods for Solid Mechanics. Rastogi, P. K., Hack. E., Editor. 2012, Wiley-VCH Verlag GmbH & Co.KG.

14. Pagnacco, E., et al., Inverse strategy from displacement field measurement and distributed forces using FEA Mechanical formulation Governing equations. Material Science and Engineering: A, 2007, 452: P. 737-45.

15. Ienny, P., Caro-bretelle, A., and Pagnacco, E., Identification from measurements of mechanical fields by finite element model updating strategies, A review. European Journal of Computational Mechanics, 2009, 18(3-4):p. 37-41.

16. Pierron, F., and Grediac, M., The Virtual Fields Mathod: Extracting Constitutive Machanical Parameters from Full-field Deformation Measurements. 2012(Publisher: Springer.)

17. Pierron, F, Avril, S., Experimental mechanics - Inverse problems in experimental solid mechanics.UNESCO-EOLSS (Encyclopedia of life support systems) sample chapters, 2008.

18. Barrett, C. S., Structure of metals, Crystallographic methods, principles, and data. Metallurgy and Metallurgical Engineering series. 1952 (Publisher: McGraw-Hill book company).

19. Withers, J. and Webster, J., Neutron and Synchrotron X-ray Strain Scanning. Strain, 2001. 37(1): p. 19-33.

20. Zerbst, U., et al., Introduction to the damage tolerance behaviour of railway rails - a review. Engineering Fracture Mechanics, 2009, 76(17): p. 2563-2601.

21. Hutching M. T., Krawitz A. D., Measurement of residual stress and applied stress using Neutron diffraction. 1993 (Publisher: Kluwer Academic).

22. Kalkar J. J., Cannon D. F., Orringer O., Rail Quality and Maintenance for Modern Railway Operation. 1993 (Publisher: Kluwer Academic).

23.   Jun, T. S., et al., Triaxial residual strains in a railway rail measured by neutron diffraction. The Journal of Strain Analysis for Engineering Design, 2009, 44(7): p. 563-568.

24.   Pfeifer, M. A., et al., Three-dimensional mapping of a deformation field inside a nanocrystal. Nature Materials, 2006, 442(7098): p. 63-66.

25.   Robinson, I. and Harder, R., Coherent X-ray diffraction imaging of strain at the nanoscale. Nature Materials, 2009, 8(4): p. 291-8.

26.   Benoit, A., et al., 3D analysis from micro-MRI during in situ compression on cancellous bone. Journal of Biomechanics, 2009, 42(14): p. 2381-6.

27.   Gilchrist, C. L., et al., High-resolution determination of Soft tissue deformations using MRI and first order texture correlation. IEEE transunctions on Medical Imaging, 2004, 23(5): p. 546-553.

28.   Gilson, W. D., et al., Measurement of myocardial mechanics in mice before and after infarction using multislice displacement-encoded MRI with 3D motion encoding. American journal of physiology. Heart and Circulatory Physiology, 2005, 288(3): p. H1491-7.

29.   Avril, S., et al., 3D Heterogeneous Stiffness Reconstruction Using MRI and the Virtual Fields Method. Experimental Mechanics, 2008, 48(4): p. 479-494.

30.   Sutton, M. A. , Orteu, J.J., Schreier, H., Image Correlation for Shape, Motion and Deformation Measurements- Basic Concepts, Theory and Applications. 2009 (Publisher: Springer Science).

31.   Bay, B. K., Methods and applications of digital volume correlation. The Journal of Strain Analysis for Engineering Design, 2008, 43(8): p. 745-760.

32   Smith, T. S., B. K. Bay, and Rashid, M. M., Digital Volume Correlation Including Rotational Degrees of Freedom during Minimization. Experimental Mechanics, 2002, 42(3): p. 272-278.

33.   Pan, B., Wu, D., and Wang, Z., Internal displacement and strain measurement using digital volume correlation: a least-squares framework. Measurement Science and Technology, 2012, 23(4): p. 1-13.

34.   Mass, H. G. , Gruen, .A., Papantoniou D., Particle tracking velocimetry in three-dimensional flows. Experiments in Fluids, 1993, 146: p. 133-146.

35.   Brucker, C., Digital-Particle-Image-Velocimetry (DPIV) in a scanning light-sheet : 30 starting flow around a short cylinder. Experiments in Fluids, 1995, 19: p. 255-263.

36. Hinsch, K. D., Three-dimensional particle velocimetry. Measurement Science and Technology, 1995, 6(6): p. 742.

37. Wu, Y., et al., Measurement of microchannel flow with digital holographic microscopy by integrated nearest neighbor and cross-correlation particle pairing. Applied Optics, 2011, 50(34): p. H297-305.

38. Soria, J. and Atkinson, C., Towards 3C-3D digital holographic fluid velocity vector field measurement-tomographic digital holographic PIV (Tomo-HPIV). Measurement Science and Technology, 2008, 19(7): p. 1-12.

39. Choi, Y. S. and Lee, S. J., Three-dimensional volumetric measurement of red blood cell motion using digital holographic microscopy. Applied Optics, 2009, 48(16): p. 2983-90.

40. Elsinga, G. E., et al., Tomographic particle image velocimetry. Experiments in Fluids, 2006, 41(6): p. 933-947.

41. Lee, S. Y., et al., Strain measurement from 3D micro-CT images of a breast-mimicking phantom. Computers in Biology and Medicine, 2011, 41(3): p. 123-130.

42. Rannou, J., et al., Three dimensional experimental and numerical multiscale analysis of a fatigue crack. Computer Methods in Applied Mechanics and Engineering, 2010, 199: p. 1307-1325.

43. Gates, M., Lambros, J., and Heath, M. T.,Towards High Performance Digital Volume Correlation. Experimental Mechanics, 2011, 51(4): p. 491-507.

44. Zauel, R., et al., Comparison of the Linear Finite Element Prediction of Deformation and Strain of Human Cancellous Bone to 3D Digital Volume Correlation Measurements. Journal of Biomechanical Engineering, 2006, 128(1): p. 1-6.

45. Verhulp, E., van Rietbergen, B., and Huiskes, R., A three-dimensional digital image correlation technique for strain measurements in microstructures. Journal of Biomechanics, 2004, 37(9): p. 1313-20.

46. Liu, L. and Morgan, E. F., Accuracy and precision of digital volume correlation in quantifying displacements and strains in trabecular bone. Journal of Biomechanics, 2007, 40(15): p. 3516-20.

47. Forsberg, F., et al., 3D micro-scale deformations of wood in bending: synchrotron radiation μCT data analyzed with digital volume correlation. Journal of Structural Biology, 2008, 164(3): p. 255-62.

48.	Christen, D., et al., Deformable image registration and 3D strain mapping for the quantitative assessment of cortical bone microdamage. Journal of the Mechanical Behaviour of Biomedical Materials, 2012, 8: p. 184-93.

49.	Forsberg, F. and Siviour, C. R., 3D deformation and strain analysis in compacted sugar using x-ray microtomography and digital volume correlation. Measurement Science and Technology, 2009, 20(9): p. 1-8.

50.	Roux, S. P., et al., Three-dimensional image correlation from X-ray computed tomography of solid foam. Composites Part A: Applied Science and Manufacturing, 2008, 39(8): p. 1253-1265.

51.	Lenoir, N., et al., Volumetric Digital Image Correlation Applied to X-ray Microtomography Images from Triaxial Compression Tests on Argillaceous Rock. Strain, 2007, 43(3): p. 193-205.

52.	Germaneau, A., Doumalin, P., and Dupre, J. C., Comparison between X-ray micro-computed tomography and optical scanning tomography for full 3D strain measurement by digital volume correlation. NDT & E International, 2008, 41(6): p. 407-415.

53.	Germaneau, A., Doumalin, P., and Dupre, J. C., Full 3D Measurement of Strain Field by Scattered Light for Analysis of Structures. Experimental Mechanics, 2007, 47(4): p. 523-532.

54.	Germaneau, A., P. Doumalin, and J.C. Dupre, 3D Strain Field Measurement by Correlation of Volume Images Using Scattered Light : Recording of Images and Choice of Marks. Strain, 2007, 43(3): p. 207-218.

55.	Deprez, J. F., et al., 3D estimation of soft biological tissue deformation from radio-frequency ultrasound volume acquisitions. Medical Image Analysis, 2009, 13(1): p. 116-27.

56.	Deprez, J. f., et al., 3D Ultrasound Elastography for Early Detection of Lesions: Evaluation on a Pressure Ulcer Mimicking Phantom. Conf Proc IEEE Eng Med Biol Soc. 2007, 1: p. 79–82.

57.	Han, Y., Kim, D. W., Jhou, B, and Kwon, H. J., Diagonsis of Breast Tumor using 2D and 3D Ultrasound Imaging. Proceedings of the ASME 2011, International Mechanical Engineering Congress & Exposition IMECE, 2011: p. 1-6.

58.	Varray, F., et al., Simulation of ultrasound nonlinear propagation on GPU using a generalized angular spectrum method. EURASIP Journal on Image and Video Processing. 2011, p. 17-17.

59. Franck, C., et al., Three-dimensional Full-field Measurements of Large Deformations in Soft Materials Using Confocal Microscopy and Digital Volume Correlation. Experimental Mechanics, 2007, 47(3): p. 427-438.

60. Huang, J., et al., a Digital Volume Correlation Technique for 3-D Deformation Measurements of Soft Gels. International Journal of Applied Mechanics, 2011, 3(2): p. 335-354.

61. Maskarinec, S. A., et al., Quantifying cellular traction forces in three dimensions. Proceedings of the National Academy of Sciences of the United States of America, 2009, 106(52): p. 22108-13.

62. Sun, C., Standish, B., and Yang, V. X. D., Optical coherence elastography: current status and future applications. Journal of Biomedical Optics, 2011, 16(4): p. 043001-043001.

63. Liang, X., Crecea, V., and Boppart, S. A., Dynamic Optical Coherence Elastography: a Review. Journal of Innovative Optical Health Sciences, 2010, 3(4): p. 221-233.

64. Drexler, W., Fujimoto, J. G., Optical Coherence Tomography; Technology and applications. 2008 (Publisher: Springer).

65. Schmitt, J., OCT elastography: imaging microscopic deformation and strain of tissue. Optics Express, 1998, 3(6): p. 199-211.

66. Ko, H. J., Tan, W., Stack, R., and Boppart, S. A., Optical Coherence Elastography of Engineered and Developing Tissue. Journal of Tissue Engineering, 2006, 12(1): p. 63-73.

67. Rogowska, J., et al., Quantitative optical coherence tomographic elastography: method for assessing arterial mechanical properties. The British Journal of Radiology, 2006, 79(945): p. 707-11.

68. Kirkpatrick, S. J., Wang, R. K. and Duncan, D. D. OCT-based elastography for large and small deformations. Optics Express, 2006, 14(24): p. 373-379.

69. Liang, X., et al., Optical micro-scale mapping of dynamic biomechanical tissue properties. Optics Express, 2008, 16(15): p. 11052-65.

70. Kennedy, B. F., et al., In vivo dynamic optical coherence elastography using a ring actuator. Optics Express, 2009, 17(24): p. 21762-72.

71. Huang, Y. P., et al., An optical coherence tomography (OCT)-based air jet indentation system for measuring the mechanical properties of soft tissues. Measurement Science & Technology, 2009, 20(1): p. 1-11.

72.   Liang, X. and Boppart, S. A., Biomechanical properties of in vivo human skin from dynamic optical coherence elastography. IEEE transactions on Bio-medical Engineering, 2010, 57(4): p. 953-9.

73.   Germaneau, A., et al., 3D mechanical analysis of aeronautical plain bearings: Validation of a finite element model from measurement of displacement fields by digital volume correlation and optical scanning tomography. Optics and Lasers in Engineering, 2010, 48(6): p. 676-683.

74.   Kennedy, B. F., et al., In vivo three-dimensional optical coherence elastography. Optics Express, 2011, 19(7): p. 6623-6634.

75.   Wiesauer, K., et al., Non-destructive quantification of internal stress in polymer materials by polarisation sensitive optical coherence tomography. Acta Materialia, 2005, 53(9): p. 2785-2791.

76.   Heise, B., et al., Spatially Resolved Stress Measurements in Materials With Polarisation-Sensitive Optical Coherence Tomography: Image Acquisition and Processing Aspects. Strain, 2010, 46(1): p. 61-68.

77.   Szotten D., Lionheart, W. R. B., Tomlinson R. A., Tomographic reconstruction of stress from photoelastic measurements using elastic regularization. Submitted to Inverse Problems, 2006.

78.   Tomlinson, R. A., et al., The Design and Commissioning of a Novel Tomographic Polariscope. Proceedings of the Society of Experimental Mechanics (SEM) Annual Conference and Exposition on Experimental and Applied Mechanics, , 2006.

79.   Huntley, J. M. and Ruiz, P. D., Depth-Resolved Displacement Field Measurement. Advances in Speckle Metrology and Related Techniques. G.H. Kaufmann, Editor. 2011, Wiley-VCH Verlag GmbH & Co.KG. p. 37-104.

80.   Wang, R. K., Ma, Z., and Kirkpatrick, S. J., Tissue Doppler optical coherence elastography for real time strain rate and strain mapping of soft tissue. Applied Physics Letters, 2006, 89(14): p. 144103-144103.

81.   Walther, J., et al., Analysis of in vitro and in vivo bidirectional flow velocities by phase-resolved Doppler Fourier-domain OCT. Sensors and Actuators A: Physical, 2009, 156(1): p. 14-21.

82.   Wang, R. K., Kirkpatrick, S., and Hinds, M., Phase-sensitive optical coherence elastography for mapping tissue microstrains in real time. Applied Physics Letters, 2007, 90(16): p. 164105-164105.

83. Li, P., et al., Assessment of strain and strain rate in embryonic chick heart in vivo using tissue Doppler optical coherence tomography. Physics in Medicine and Biology, 2011, 56(22): p. 7081-92.

84. De la Torre Ibarra, M. H., Ruiz, P. D., and Huntley, J. M., Simultaneous measurement of in-plane and out-of-plane displacement fields in scattering media using phase-contrast spectral optical coherence tomography. Optics Letters, 2009, 34(6): p. 806-8.

85. Huang, D., et al., Optical coherence tomography. Science, New series, 1991, 254(5035): p. 1178-81.

86. Fujimoto, J. G., and Farkas, D., Biomedical optical imaging. 2009 (Publisher: Oxford, University Press).

87. Fercher, F., Hitzenberger, K., and Kamp, G., Measurement of intraocular distances by backscattering spectral interferometry. Optics Communications, 1995, (117): p. 43-48.

88. Hymans, A. J., et al., Analysis of a frequency-modulated continuous-wave ranging system. Proceedings of IEE-Part-B: Electronics and Communication Engineering, 1960, 117(34): p. 365-372.

89. Eickhoff, W., Optical frequency domain reflectometry in single-mode fiber. Applied Physics Letters, 1981, 39(9): p. 693-693.

90. Sekine, A., Minegishi, I., and Koizumi, H., Axial eye-length measurement by wavelength-shift interferometry. Journal of Optical Society of America A, 1993, 10(7): p. 1651-1655.

91. Chinn, S. R., Swanson, E. A., and Fujimoto, J. G., Optical coherence tomography using a frequency-tunable optical source. Optics Letters, 1997, 22(5): p. 340-342.

92. Lexer, F., et al., Wavelength tuning interferometry of intraocular distances. Applied Optics, 1997, 36(25): p. 6548-6553.

93. Mehta, D. S., et al., Scientific and Engineering Applications of Full-field Swept-source Optical Coherence Tomography. Journal of the Optical Society of Korea, 2009, 13(3):p. 341-348.

94. Srivastava, V., Mehta, D. S., et al., Tomographic and volumetric reconstruction of composite materials using full-field swept-source optical coherence tomography. 2012, Measurement Science and Technology, 23:p.1-10.

95. Dhalla, A. H., Izatt, A., et al., Dual-depth SSOCT for simultaneous complex resolved anterior segment and conventional retinal imaging. Proceedings of SPIE , 2012,8213:p.82131G-1-82131G-4

96. Dhalla, A. H., Izatt, A., et al., Simultaneous swept source optical coherence

tomography of the anterior segment and retina using coherence revival. Optics Letters, 2012, 37(11):p.1883-85.

97. Kuwamura, S., and Yamaguchi, I., Wavelength scanning profilometry for real-time surface shape measurement. Applied Optics, 1997, 36(19): p. 4473-4482.

98. Groot, P. D., Measurement of transparent plates with wavelength-tuned phase-shifting interferometry. Applied Optics, 2000, 39(16): p.2658-2663.

99. Akihiro, Y. and Y. Ichirou, Profilometry of sloped plane surfaces by wavelength scanning interferometry. Optical Review, 2002, 9(3): p. 112-121.

100. Hibino, K., et al., Simultaneous measurement of surface shape and variation in optical thickness of a transparent parallel plate in wavelength-scanning Fizeau interferometer. Applied Optics, 2004, 43(6): p. 1241-1249.

101. Hwang, Y. M., et al., Thin-film thickness profile measurement using wavelet transform in wavelength-scanning interferometry. Optics and Lasers in Engineering, 2008, 46: p. 179-184.

102. Gao, F., et al., Wavelength scanning interferometry for measuring transparent films of the fusion targets. 13th International Conference on Metrology and Properties of Engineering Surfaces, 2011, Twickenham, UK.

103. Davila, A., et al., Simultaneous wavenumber measurement and coherence detection using temporal phase unwrapping. Applied Optics, 2012, 51(5): p. 558-67.

104. Ghim, Y. S., Suratkar, A., and Davies, A., Reflectometry-based wavelength scanning interferometry for thickness measurements of very thin wafers. Optics Express, 2010, 18(7): p. 6522-6529.

105. Thiel, J., Pfeifer, T., and Hartmann, M., Interferometric measurement of absolute distances of up to 40 m. Journal of Measurement, 1995, 16(1): p. 1-6.

106. Kikuta, H., Iwata, K., and Nagata, R., Distance measurement by the wavelength shift of laser diode light. Applied Optics, 1986, 25(17): p. 2976-2976.

107. Barwood, G. P. et al., Laser diodes for length determination using swept-frequency interferometry. Measurement Science and Technology, 1993, 9(4): P. 988.

108. Xiaoli, D., and Katuo, S., High-accuracy absolute distance measurement by means of wavelength scanning heterodyne interferometry. Measurement Science and Technology, 1998, 9(7): p. 1031-35.

109. Bechstein, K. H., et al., Absolute interferometric distance measurements applying a variable synthetic wavelength. Journal of Optics, 1998, 29(3), p: 179-82(4).

110. Cabral, A., Abreu, M., and Rebordao, J., Absolute distance metrologyfor long distances with dual frequency sweeping interferometry. Fundamental and Applied Metrology, 2009, p. 1942-1947.

111. Coe, P. A., Howell, D. F., and Nickerson, R. B., Frequency scanning interferometry in ATLAS: remote, multiple, simultaneous and precise distance measurements in a hostile environment. Measurement Science and Technology, 2004, 15(11): p. 2175-2187.

112. Fox-Murphy, A. F., et al., Frequency Scanned Interferometry (FSI): The basis of a survey system of ATLAS using fast automated remote interferometry, Nuclear Instruments and Methods in Physics Research Section A: Accelerators, Spectrometers, Detectors and Associated Equipments, 1996, 383(1),p: 229-37.

113. Gibson, S. M., A study of geodetic grids for the continuous, quasi real time alignment of the ATLAS semiconductor tracker. Proceedings of the 7th International Workshop on Accelerator Alignment,SPring-8, 2002.

114. Gibson, S. M., et al., The Multi-channel High Precision ATLAS SCT Alignment Monitoring System : A Progress Report. Proceedings of the 7th International Workshop on Accelerator Alignment, 2006, p. 1-11.

115. Gibson, S. M., et al., Monitoring the heart of ATLAS using Frequency scanning interferometry. IWAA2004, CERN, Geneva, 2004.

116. Gibson, S.M., et al., Coordinate measurement in 2-D and 3-D geometries using frequency scanning interferometry. Optics and Lasers in Engineering, 2005, 43(7): p. 815-831.

117. Yang, H. J., Nyberg, S., and Riles, K., High-precision absolute distance measurement using dual-laser frequency scanned interferometry under realistic conditions. Nuclear Instruments and Methods in Physics Research Section A, 2007, 575(3): p. 395-401.

118. Yang, H. J., Chen, T., and Riles, K., Frequency Scanned Interferometry for ILC Tracker Alignment. Proceedings for the DPF-2011 Conference, Providence, RI, 2011.

119. Yang, H. J., et al., High-precision absolute distance and vibration measurement with frequency scanned interferometry. Applied Optics, 2005, 44(19): p. 3937-44.

120. Swinkels, B. L., Absolute distance metrology for space interferometers. Proceedings of SPIE, 2004,: p. 314-318.

121. Ruiz, P. D., Huntley, J. M., and Wildman, R. D., Depth-resolved whole-field displacement measurement by wavelength-scanning electronic speckle pattern interferometry. Applied Optics, 2005, 44(19): p. 3945-3953.

122.   Ruiz, P. D., Huntley, J. M., and Coupland, J. M., Depth-resolved Imaging and Displacement Measurement Techniques Viewed as Linear Filtering Operations. Experimental Mechanics, 2011, 51(4): p. 453-465.

123.   Davila, a., et al., Wavelength scanning interferometry using a Ti:Sapphire laser with wide tuning range. Optics and Lasers in Engineering, 2012, 50(8): p. 1089-1096.

124.   Coupland, J. M. and Lobera, J., Holography, tomography and 3D microscopy as linear filtering operations. Measurement Science and Technology, 2008, 19(7): p. 074012-074012.

125.   Chakraborty, S. and Ruiz, P. D., Measurement of all orthogonal components of displacement in the volume of scattering materials using wavelength scanning interferometry. Journal of Optical Society of America A., 2012, 29(9): p. 1776-1785.

126.   Manual of TSL-510 Tunable laser, Santec Ltd..

127.   Manual of NIR InGaAs detector, Goodrich Corporation.

128.   Huntley, J. M., Three-dimensional noise-immune phase unwrapping algorithm. Applied Optics, 2001, 40(23): p. 3901-8.

129.   Salfity, M. F., et al., Branch cut surface placement for unwrapping of undersampled three-dimensional phase data: application to magnetic resonance imaging arterial flow mapping. Applied Optics, 2006, **45**(12): p. 2711-2722.

130.   Salfity, M. F., et al., Extending the dynamic range of phase contrast magnetic resonance velocity imaging using advanced higher-dimensional phase unwrapping algorithms. Journal of the Royal Society Interface, 2006, **3**(8): p. 415-427.

131.   Huntley, J. M., et al. Robust three-dimensional phase unwrapping algorithm for phase contrast magnetic resonance velocity imaging. Fifth International Workshop on Automatic Processing of Fringe Patterns. 2005.

132. Zhao, M., Kuo, A. N., and Izatt, J. A., 3D refraction correction and extraction of clinical parameters from spectral domain optical coherence tomography of the cornea. Optics Express, 2010, 18(9): p. 8923-36.

133.   Abdul-Rahman, H. S., et al., Fast and robust three-dimensional best path phase unwrapping algorithm. Applied Optics, 2007. 46(26): p. 6623-35.

134.   Abdul-Rahman, H. S., et al., Robust three-dimensional best-path phase-unwrapping algorithm that avoids singularity loops. Applied Optics, 2009, 48(23): p. 4582-96.

135. Jenkinson, M., Fast, automated, n-dimensional phase-unwrapping algorithm. Magnetic Resonance in Medicine, 2002, 49(1):p. 193-197.

136. Stifter, D., Beyond biomedicine: a review of alternative applications and developments for optical coherence tomography. Applied Physics B, 2007, 88:p. 337-

137. Grediac, M., The use of full-field measurement methods in composite material characterization: interest and limitations. Composites: Part A, 2004, 35,:p. 751-761.